UNIVERSITÀ DEGLI STUDI DI PADOVA

Technical University of Denmark

UNIVERSITA' DEGLI STUDI DI PADOVA

Dipartimento di Ingegneria Industriale DII

Corso di Laurea Magistrale in Ingegneria Aerospaziale

Configuration Optimisation of Kite-based Wind Turbines

Relatori:

Ernesto Benini

Mac Gaunaa

Michael McWilliam

Mathias Stolpe

Studente:

Filippo Trevisi 1153496

Anno Accademico 2018/2019

Prefazione

Lo scopo di questa tesi è quello di analizzare, in modo sistematico, i sistemi di estrazione di potenza eolica chiamati *crosswind airborne wind energy systems*. Questi sistemi estraggono potenza dal vento grazie a velivoli connessi a terra tramite un cavo: si distinguono in *Ground-Generation* e *Fly-Generation airborne wind energy systems*.

I sistemi *Ground-Generation* producono potenza sfruttando le forze aerodinamiche del velivolo per esercitare una forza di trazione sul cavo e srotolarlo. L'energia elettrica è prodotta con un generatore piazzato al suolo. La produzione di potenza, in questo caso, è composta da due fasi: una fase di produzione, in cui l'energia è prodotta e il velivolo si allontana dalla stazione a terra, e una fase di recupero, in cui il velivolo ritorna al punto di partenza.

I sistemi *Fly-Generation* producono potenza con delle piccole turbine eoliche montate a bordo del velivolo. In questo caso, la potenza elettrica può essere prodotta in maniera continuativa.

Nel mondo della ricerca e imprenditoriale questi due metodi sono studiati separatamente. Un confronto è spesso fornito da considerazioni qualitative o in base alle prestazioni finali. Un metodo di confronto sistematico è proposto in questa tesi. In questo modo, uno studio dei design di massima dei due sistemi può essere ottenuto.

Nella prima parte della tesi le equazioni di potenza dei due sistemi sono unificate in un'unica equazione, con l'assunzione di volo stazionario. In questo modo, le due tipologie possono essere studiate con un'unica trattazione. Questa formulazione analitica tiene in conto della massa del sistema: consente infatti la stima delle perdite di potenza dovute alla massa. Un design di massima della struttura, dell'elettronica di bordo e del cavo fornisce una stima della massa in volo, necessaria per il calcolo della potenza estraibile. Il modello proposto in questa tesi comprende gli aspetti salienti dei vari sotto-sistemi.

Una volta presentato il modello, i metodi usati per studiarlo sono mostrati. Due metodi sono usati in maniera sequenziale. Il primo consiste in un'ottimizzazione mediante un algoritmo *gradient-based*. L'algoritmo modifica delle variabili per massimizare una funzione obbiettivo. Facendo ciò, realizza un design del sistema. L'ottimizzazione può essere considerato un processo totalmente deterministico che, per dei valori di alcuni parametri, fornisce un design di configurazione del sistema. Il secondo metodo stima quindi come questi parametri influenzano il design. Questo studio è svolto con una analisi di sensitività globale, in particolare con una tecnica chiamata *variance-based decomposition*. Questa tecnica stima la sensitività della varianza degli output, che descrivono gli ottimi design, con rispetto alla varianza degli input. La varianza degli input è assegnata e rappresenta le incertezze dei parametri. Queste incertezze rappresentano fonti di incertezza dovute a parametri aleatori, diversi design, sviluppi tecnologici di componenti, prestazioni di componenti non sviluppati e così via. In questo modo, è possibile studiare le configurazioni robuste e gli aspetti critici dei design nel futuro.

I risultati, per il caso in cui i sistemi sono ottimizzati per massimizzare la produzione annua, sono mostrati, evidenziando i trend chiave nei design.

Sucessivamente, un modello economico è proposto per valutare il costo di questi sistemi. Gli stessi metodi sono utilizzati per studiare i design ottimizzati per massimizare il profitto. I risultati, per questo caso, sono mostrati per sistemi *Ground-Generation* e *Fly-Generation*, evidenziando le interessanti possibilità che queste tecnologie, una volta mature, possono avere da un punto di vista commerciale.

Abstract

The aim of this thesis is to analyse in a systematic way the design of crosswind airborne wind energy systems. Ground generation and Fly generation airborne wind energy systems should be seen from one perspective, to identify the common critical design drivers. The strong configurations and the sub-systems that need to be developed should be determined. Thus, this work is looking into optimal crosswind AWES into the future.

A generalization of the Loyd power equations is derived, to model a system with ground and onboard generation. The main sub-systems and physics are considered: reel-in phase, additional drag due to tether and lifting line theory, tether sag, structural design of the aircraft, take-off strategy and dimension of onboard turbines. Once the flying mass is found, the relative power losses are evaluated. To evaluate the power losses due to mass an analytic model is proposed. This model can be useful to AWES designers to estimate the influence of the flying mass on the power production with analytic equations.

The physical model of a generic crosswind AWES is implemented into an optimisation algorithm, which performs the kite design to maximise the annual energy production. Many aleatory and epistemic uncertainties are present in the problem. Thus, a global sensitivity analysis outlines how these uncertainties propagate throughout the design.

To maximise the AEP, the kite wing area and the aerodynamic coefficients are found to be the design drivers. The main sub-systems are analysed, outlining the critical issues and main characteristics.

In the second part of the thesis, a cost model is included. The cost model takes into account kite structure, tether, generators, electronics, take-off and landing structure, tower, fix cost and operation costs. A life for tether and kite is considered. The cost model is implemented in the optimisation algorithm, to find designs that maximise the profits.

A global sensitivity analysis shows the key trends in the optimal designs, outlining the characteristics that commercial AWES will have in the future and their strength.

Acknowledgements

I would like to acknowledge my supervisors for the support and advices during this period. Thanks to Professor Mac Gaunaa for the enthusiasm and for the long engaging discussions. I acknowledge Professor Michael McWilliam for the enlightening comments and meetings. Before December, I didn't know about AWES. It is because of him that I discovered this fascinating world. Thanks to Professor Mathias Stolpe for the encouragement and the broad comments. I acknowledge Professor Ernesto Benini for the comments and for the suggestions concerning future works.

Thanks to my girlfriend, Victoria, for the reviews. Thank Jules, Fabio and Simone for listening to my thoughts during lunches and dinners. Thanks to my family for giving meaning to the word home. I acknowledge the University of Padova, which formed my way of thinking, and the Technical University of Denmark, which completed my education. Thanks to the company *KiteX* for the industrial insight.

To Vanessa and Tommaso, just married

Contents

List of Figures

List of Tables

Acronyms

AEP Annual Energy Production

AWE Airborne Wind Energy

AWES Airborne Wind Energy Systems

CF Capacity factor

DV Design Variables

FG-AWES Fly Generation Airborne Wind Energy System

GG-AWES Ground Generation Airborne Wind Energy System

ICC Initial Capital Cost

LCOE Leverized Cost of Energy

VBD Variance Based Decomposition

Nomenclature

A Weibull scale parameter. In Chapter 3 it stands for wing area for readability.

a On-board wind turbines induction factor

a_{el} Coefficient for the generator cost

A_g Ground area needed for taking-off and landing

A_{kite} Wing area.

α_{TO} Climbing angle during take-off

A_{prop} Propellers rotor area

AR Wing aspect ratio

A_{turb} Rotor area of on-board turbines

B Support position

β Elevation angle

C_d Drag coefficient

C_{d0} Drag coefficient at zero lift

C_{fix} Fixed costs

C_L Lift coefficient

$cost_{el}$ Cost of the electronics

$cost_{kite}$ Cost of the kite structure

$cost_t$ Cost of the tower

$cost_{te}$ Cost of the tether

$cost_{TOs}$ Cost of the take-off sub-system

$C_\perp$ Drag coefficient of the tether.

c_t Factor for the manufacturing cost of the tower

D Aerodynamic drag force

d Tether diameter

Δ Additional kite inclination due to the flying mass

δ Maximum allowed structural deflection evaluated in the wing center and wing tip. It is expressed as a percentage of the span.

δ_{in} Deflection evaluated in the wing centre

δ_{out} Tip deflection

E_{gen} Generators power density

eta_d^{min} Minimum allowed efficiency due to disc theory of on-board turbines.

η_{in} Efficiency of the reel-in phase.

η_{out} Efficiency of the reel-out phase; it includes efficiency of trajectory and power conversion on the ground

η_{pr} Efficiency of propellers with respect to disc theory

η_t Efficiency of the on-board power generation; it does not include disc thery losses

$\eta_{t\,pr}$ Efficiency of the turbines used as propellers with respect to disc theory

E_{TO} Energy spent during the take-off

$f_{r.\,gl}$ Frequency of replacement of the kite

$f_{r.\,te}$ Frequency of tether replacement

f_{te} Cost factor that takes into account the manufacturing of a tether with power transmission

g Gravity acceleration constant.

γ_{in} Ratio between reel-in velocity and wind velocity: $\gamma_{in} = \frac{V_{in}}{V_w}$

γ_{out} Ratio between reel-out velocity and wind velocity: $\gamma_{out} = \frac{V_{out}}{V_w}$

γ_t Ratio between drag given by on-board turbines and aerodynamic drag: $\gamma_t = D_{turb}/D_{kite} = C_{d\,turb}/C_d$.

G_e Glide ratio

h Operational altitude

h_{min} Minimum operational altitude

h_t Tower height

h_t^{max} Upper bound for the tower height

i Discout rate

L Aerodynamic lift force

λ Lagrange multiplier

λ_{CL} Lagrange multiplier on the lift coefficient upper bound

$\lambda_{\delta in}$ Lagrange multiplier on the structural deflection evaluated at the wing centre

$\lambda_{\delta out}$ Lagrange multiplier on the tip structural deflection

λ_{hmin} Lagrange multiplier on the minimum operational altitude contraint

λ_{ht} Lagrange multiplier on the tower height upper bound

λ_M Lagrange multiplier on the structural material strength constraint

λ_{Prated} Lagrange multiplier on the rated power contraint

λ_{te} Lagrange multiplier on the tether strength constraint

m_{el} Electronics on-board mass

m_{gl} Structural mass

m_{te} Tether mass

m_{TO} Take-off mass

m_{tot} Total flying mass

n_y Number of operational years

OC Operation cost

p_{Ag} Price per unit area for the take-off structure

P_{cycle} Mean power output over the generation and recovery phases

p_{el} Price of electricity

P_{FG} Power generated with on-board turbines, without reel-out.

P_{GG} Power ground generated, in case of no on-board generation

P_{gr} Power ground generated.

Π Annual profit

P_{ob} Power on-board generated.

p_{te} Tether material price

P_w Power density: $P_w = \frac{1}{2}\rho_{air}V_w^3$

p_{wing} Wing structural material price

Q Thrust force during take-off

r Tether length

R_a Aerodynamic resultant force

ρ_{air} Air density

ρ_{carb} Structutal material density

s Wing span

$SF_{\sigma lim}$ Safety factor on the tether strength

T Force acting on the tether

$Tether$ Cable connecting the aicraft to the ground

θ Inclination of the tether at the connection with the kite

V Line voltage on the electric transmittion in the tether.

V_{in} Cut-in wind velocity

V_{out} Reel-out velocity of the tether

V_r Component of the wind speed perpendicular to the kite wing area

V_w Wind speed

$V_{w\|}$ Component of the wind speed perpendicolar to the kite wing area

Chapter 1

Introduction

The first news related to the use of a kite to pull a load dates back to the early 1800, when George Pocock (1774–1843) [1] invented the "Charvolant", a kite-drawn carriage patented in 1826. Only in 1980, almost two centuries later, the kites were brought back to the attention of the scientific community by M. L. Loyd [2], with a short paper describing the physics of kites flying crosswind. In this paper [2], discussed in Section 3.1 and 3.2, the author shows that the potential power output from an ideal kite flying crosswind is much higher than a traditional wind turbine, for the same lifting area. However, the absence of a cheap and reliable control system in the 1980-s, has made it difficult to commercialize the concept.

Loyd pointed out that kites flying crosswind can harvest power from the wind in two ways. In the first way, the kite pulls and unwinds a tether. The power is generated on the ground, using an electrical generator. In this thesis this system is called Ground Generation Airborne Wind Energy System (GG-AWES). In the second way, the kite generates power onboard with some wind turbines and transmits it to the ground through an electric cable. In this thesis this system is called Fly Generation Airborne Wind Energy System (FG-AWES). Figure 1.1 outlines the two concepts.

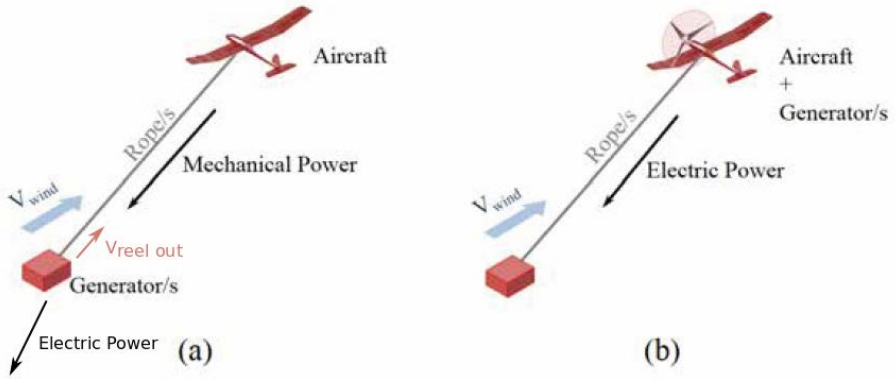

Figure 1.1: Distinction between GG-AWES (a) and FG-AWES (b) [3].

Only in the last two decades, the computational and sensory progress have been making kites a realistic way of extracting power from the wind. Moreover, society is asking more and more to enhance the renewable energy production, thus incentives are available for new companies aiming to produce green energy. All these factors have promoted the birth of many start-ups, developing slightly different concepts from each other, and stimulating researcher's interest. Figure 1.2 gathers all the researcher groups and the companies worldwide. Most of the activities are concentrated in Europe and USA.

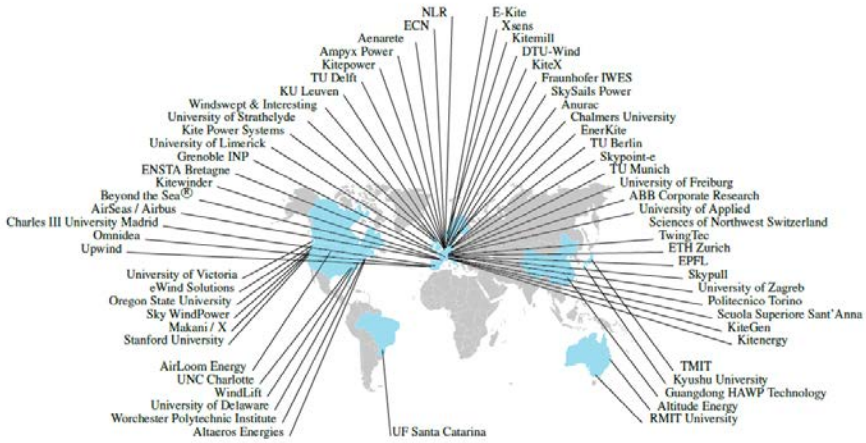

Figure 1.2: AWE research and development activities in 2017. [4]

1.1 Motivations

Researches and companies are studying and developing GG-AWES or FG-AWES. A comparison between the two crosswind generation types is often driven by qualitative considerations or by a comparison between the final design performances. The motivation of this thesis is to look for a systematic method to evaluate crosswind AWESs, studying them from one perspective. The impact of uncertainties, new technologies, unknown performances, different designs and design constraints on the design should be estimated. In this way, one can evaluate the strong configurations and understand the level of technology that needs to be developed. So, this work is looking into optimal crosswind AWES designs *in the future*.

1.2 Overview of the work

This thesis is divided into nine chapters.

Chapter 2 is giving an overview on the main characteristics of crosswind AWES.

Chapter 3 shows the physical model used in this thesis. Initially, the power equations for GG-AWES and FG-AWES are derived with a refinement of the Loyd [2] formulation. Later, one unified power equation for a generic crosswind AWES is derived. A structural and a take-off model allow the computation of the system mass. A refinement of the power equation for a generic crosswind AWES is then proposed, to take into account the system mass.

Chapter 4 presents the methods used to evaluate the model. A gradient based optimisation algorithm is used to perform the kite design. Multiple sensitivity analysis techniques are proposed in the chapter. These techniques aim to give a complete picture of the kite optimal designs. The local sensitivity analyses, performed by taking the gradients and by looking at the Lagrange multipliers of the optimal solutions, give a local understanding of the kite design. The global sensitivity analysis, performed with a *variance based decomposition*, gives an understanding on how the designs change with a large change of the inputs. In this way, the impact of uncertainties, new technologies, unknown performances, different designs and design constraints can be evaluated.

Chapter 5 shows the results for the annual energy production maximisation. The model

presented in Chapter 3 is implemented in an optimisation algorithm. The optimiser preforms the kite design, maximising the energy production. With the global sensitivity analysis, it is investigated how the uncertainties related to the model propagate. In this way, the design drivers and the strong configurations can be found.

Chapter 6 presents the cost model of a generic crosswind AWES. The main subsystems are considered and the cost functions given.

Chapter 7 shows how kite designs look like, if profit is maximised. With the global sensitivity analysis, how the physical and economical uncertainties propagate throughout the designs is studied.

Chapter 8 proposes future works.

Finally, Chapter 9 gathers the main findings of this thesis.

Chapter 2

Background

The aim of this chapter is to give an overview of the characteristics of Airborne Wind Energy Systems flying crosswind. Initially, some considerations related to the wind power at high altitudes are presented. Later, a classification of the crosswind AWES is shown and the main take-off strategies introduced.

2.1 Wind resources at high altitude

One of the reasons why AWES is so interesting is the possibility of accessing high wind resources located at high altitudes. Different concepts of AWES have different technical limits in altitude, ranging from some hundred meters to several kilometres [3]. Thus, it is interesting to study how much kinetic power can be extracted from the wind at different heights. Archer in [5] and [6] tries to give an estimation of the available power and proposes some atmospheric models. Later Bechtle [7] assesses the wind potential all over Europe, showing wind profiles and wind distributions for AWES.

To compare wind resources at different altitudes, the available power should be considered, instead of the wind speed. The power carried from the wind passing through an area A is indeed function of the air density ρ and the wind velocity V_w:

$$\mathrm{P}=\frac{1}{2}\rho A V_w^3 \tag{2.1}$$

The air density is decreasing with the altitude, while the wind speed is generally increasing.

At high altitude ($h > 1000$ m) the wind speed is due to geographic differences in pressure and Coriolis Forces. These forces produce high wind speed with low turbulence.

In Figure 2.1, the power available at different altitudes is shown for three percentiles. The percentiles are showing with which frequency the power density is higher than the highlighted one. Clearly, an increase in the power density can be seen with an increase in altitude. The first image, at a level of 80 m, is representative of a traditional wind turbine: only in a few location across the globe, the median power density is about 0.3 kW/m^2. With increasing altitude, more and more locations have the same power. This highlights another important aspect, accessing wind at higher altitudes makes wind energy feasible in more locations.

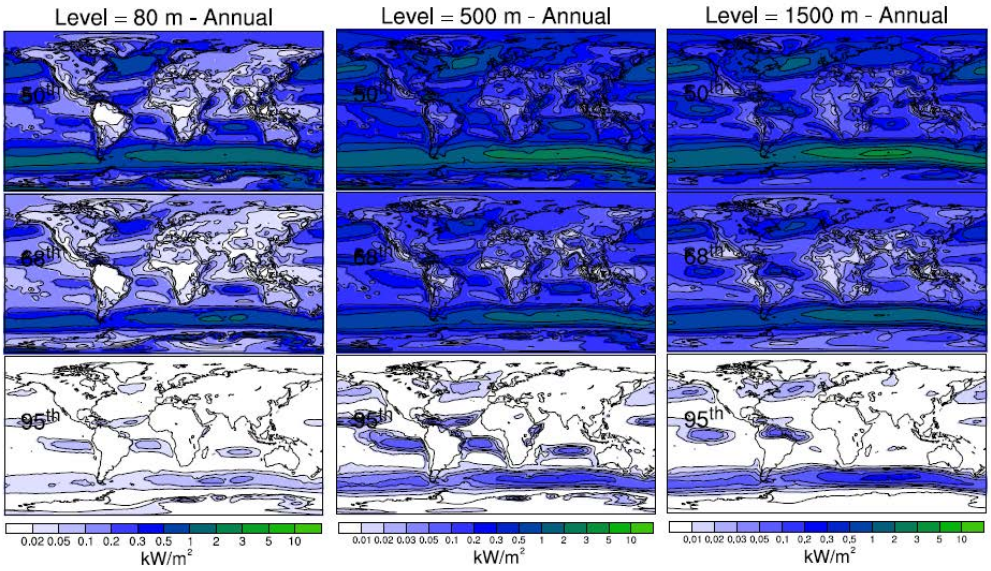

Figure 2.1: 50^{th}, 68^{the} and 95^{th} percentiles of wind power density at three heights above the ground. [6]

2.2 Classification of Airborne Wind Energy Systems

Airborne Wind Energy Systems AWESs are generally composed of two main parts: a ground station and at least one aircraft mechanically connected to the ground station. The main distinction between AWES is the way in which power is harvested.

Ground Generation Airborne Wind Energy Systems (GG-AWES) produce power on the ground: the aerodynamics force on the kite pulls and unwinds a tether. The mechanical power is transmitted by means of the pulling force and the reel-out velocity. Finally, it is transformed into electricity using an electrical generator (Figure 1.1(a)). Once the tether is completely unwound, the kite needs to go back to the starting point. The power generation is then composed of a generation and a recovery phase.

Fly Generation Airborne Wind Energy Systems (FG-AWES) can be classified as crosswind systems and non-crosswind systems depending on how they produce power [8]. FG-AWES flying crosswind generate power on-board with some small wind turbines and transmit it to the ground through an electric cable (Figure 1.1(b)). In this case, the tether is not reeled out: power is produced continuously. In this thesis only crosswind FG-AWES are considered.

2.3 Ground-Generation Airborne Wind Energy Systems

2.3.1 Generation strategies

Considering Ground Generation Airborne Wind Energy System, different strategies are studied for the power conversion. This leads to a distinction between *fixed ground station* systems, where the ground station is fixed, and *moving ground station*, where the mechanical force is moving a vehicle.

One of the characteristics of the *fixed ground station* GG-AWES is the periodicity of the power output. The power generation cycle is indeed composed of a generation and a recovery phase.

Referring to Figure 2.2, in the generation phase, the aircraft is pulling and unwinding the tether, connected to a generator. In the recovery phase, the aircraft changes the aerodynamic configuration to close the loop going back to the initial point, while the tether is wound back. In this phase, a small amount of power is spent. To analyse the total power output both phases need to be taken into consideration.

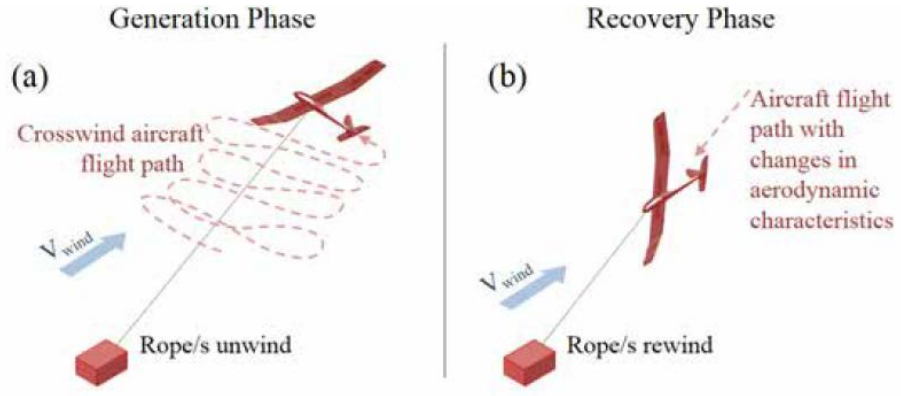

Figure 2.2: Graphical representation of the two GG-AWES phases [3].

For *moving ground station* GG-AWES, the main concepts are represented in Figure 2.3. The aim of having the power production on a moving ground station is to continuously produce energy, avoiding the recovery phase.

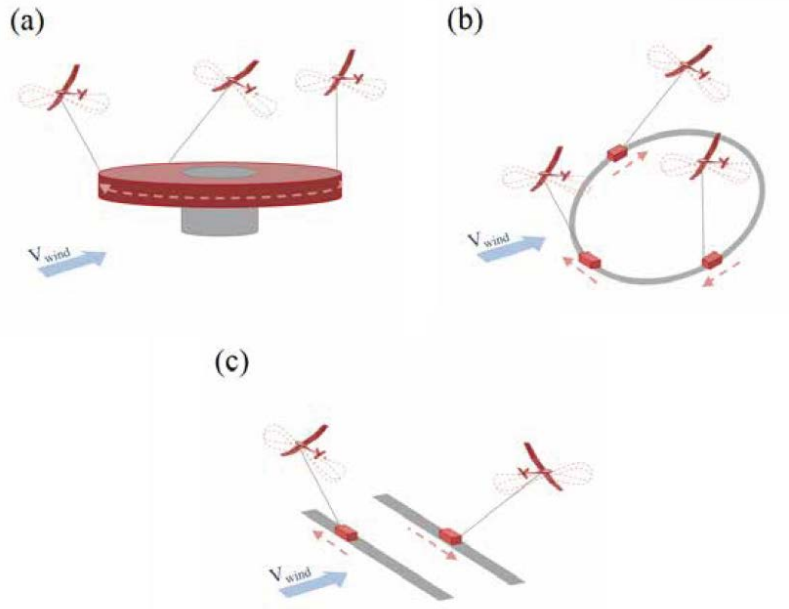

Figure 2.3: Three concepts of *moving ground station* GG-AWES.Carousel (a), closed loop rail (b) and open loop rail (c) [3].

The carousel configuration (a) consists of multiple GG-AWESs connected to the same rotor. All the GG-AWESs drive the generator, allowing a continuous power production. With the closed loop rail configuration (b) a number of wagons are carried by the kites along a closed track [9]. The wagons are generating power when the wind is perpendicular to the direction of the movement. They exploit aerodynamic drag when the movement is in the same direction of the wind and they spend some power when the movement is opposite to the wind direction. Finally, the open loop rail concept (c) is similar to the closed loop rail,

the wagons move only perpendicular to the wind direction. However, the wagon has to stop and change direction when the rail ends and this system can operate only with wind perpendicular to the rail direction.

In this thesis, only *fixed ground station* GG-AWES are considered.

2.3.2 Aircraft types

Different aircraft types could be suitable for a Ground Generation Airborne Wind Energy System. Figure 2.4 gathers the main concepts. The main characteristics of each of them are listed below.

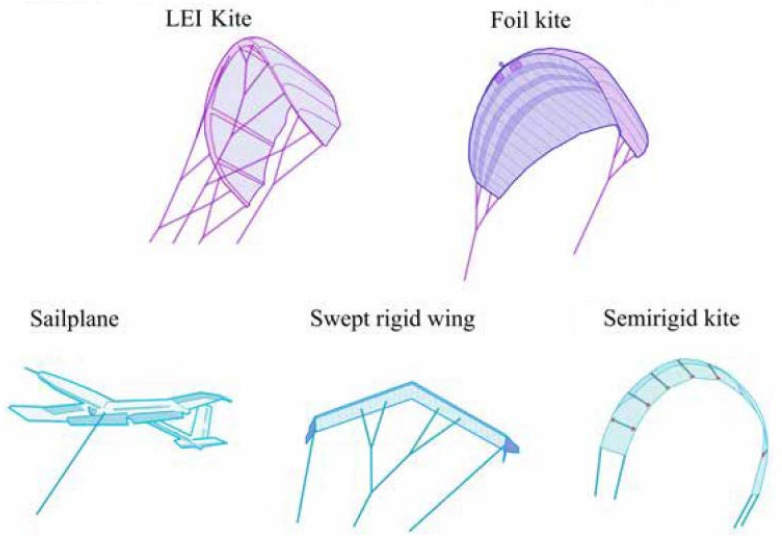

Figure 2.4: Different aircraft types for Ground Generation Airborne Wind Energy Systems [3].

LEI Kite This concept of soft kite was patent in 1987 [10], it is still used mainly for sub-components testing of AWES and on small scale prototypes. It consists of a single layer kite with an inflatable structure on the leading edge. The main problem of this kite is the scalability to bigger size, that makes this design less attractive [3].

Foil kites This concept is based on two layers, constituting canopy cells from leading to trailing edge. [11] The cells are inflated through some opening on the leading edge. Comparing this design with the LEI Kite, the foil wings have better aerodynamic performances and the size can be much bigger. The main problem for fabric wing is the durability, besides an automated launching and landing. It has been estimated that the lifetime is around several hundred hours [12].

Semi-rigid wings This concept is composed of many short rigid parts together with some fabric parts. The results is a structure lighter than a rigid wing and more durable than a fabric one [3].

Sailplane or Gliders This concept is based on a solid structure, that leads to high aerodynamics performances. Compared to soft kites, they are heavier, more expensive but they can be designed to infinite lifetime [13].

Swept rigid wings This concept is similar to gliders, but without any fuselage and tail. The stability is more challenging, it has to be attained with the bridle system and the sweep angle [3].

2.4 Fly-Generation Airborne Wind Energy System

A Fly Generation Airborne Wind Energy System produces electric energy on-board, while flying, using turbines. The power is transmitted to the ground trough an electric cable. Compared to GG-AWES, this concept produces power continuously (with still some fluctuations due to the trajectory), and the tether is unrolled only during the take-off and landing manoeuvres.

Only a few aircraft designs have been proposed for this concept: a glider from *Makani Power* [14] and a biplane, initially from *Joby Energy* [3] and recently from *KiteKraft* [15].

Cherubini [3] and the Danish Company *KiteX* [16] are investigating a possible solution to drastically reduce the drag due to the tether by flying two drones on the same line (Figure 2.5). By reducing drag, multiple drones could fly at a higher altitude, with more available wind power.

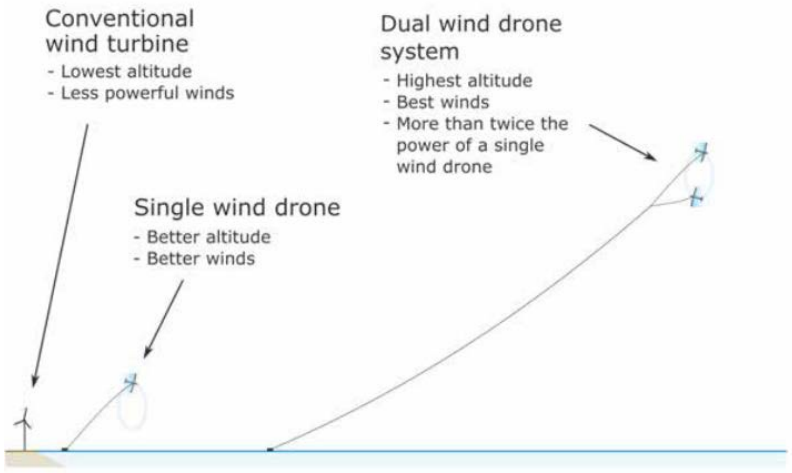

Figure 2.5: Comparison between different wind energy technologies [3].

2.5 Take-off

Take-off is known to be one of the critical phases of the design of an AWES. According to the power production technique, different take-off strategies are investigated in literature.

The state of art of take-off for FG-AWES is the vertical take-off, using the turbines as propellers [14] [15]. This strategy is considered to be the best, as the turbines have already the dimensions to lift the kite vertically. Thus no significant modification to the structure has to be done. The control system, making the kite to fly as a drone, takes care of taking off and landing on the platform. A high reliability of the procedure can be attained. It is worth mentioning the researches related to take-off of multiple drones connected to the same line. For this concept, Cherubini [3] proposes a rotational take-off.

For GG-AWES, there are different techniques currently being investigated. The first distinction is between soft and hard kites. For soft kites, a telescopic mast that holds the kite can be used, while the canopy inflates [17]. Also the landing exploits the same mast. For hard kites three solutions are studied: linear, rotational and vertical take-off:

Linear The kite has to be equipped with on-board propellers. This technique is currently implemented by Ampyx Power [13], and is studied initially in [17] and [18]. The

aircraft is initially accelerated along a runway by an external device, that usually is the winch itself. Once the kite has started to flight, the necessary thrust to climb is given by on-board propellers.

Rotational This strategy is studied in literature in [17] and [18]. It is implemented by the German company *EnerKite* [19]. With this technique, the aircraft is accelerated using a rotating arm. Exploiting the lift given by the tangential velocity, the aircraft takes off and the tether is released accordingly. No on-board propeller is needed.

Vertical This technique is studied widely, since can used by both GG-AWES [20] [21] and FG-AWES [14]. The on-board propellers carry the kite up to the necessary altitude.

Chapter 3

Physical modelling of a generic crosswind AWES

In this chapter, the physical modelling related to the power production is presented.

Initially, a refined model for GG-AWES and for FG-AWES from literature are introduced. These models are based on the assumptions of steady state flight and negligible mass.

After, a unified model, which can handle ground and on-board generation at the same time, is derived. Then, the flying mass is estimated with a structural model and a take-off model. Once the flying mass is computed, the unified model is modified to take into account the power losses due to mass.

The model presented in this chapter aims to resolve the main characteristics and the most important physics of crosswind AWES, without looking at the details of each sub-system.

Since in this work the model is implemented in an optimisation algorithm, analytical equations are needed to make the computation fast. The unified model is derived to let the optimiser to choose how to generate power and to look at crosswind AWES as a whole. Moreover, the optimiser should be able to perform a structural design and decide on the take-off strategy.

The models proposed in this work are only representative of hard kites.

In this chapter the wing area is defined as A for readability.

3.1 Power equation of Ground-Gen Airborne Wind Energy System

In this section, the main passages of a refined derivation for the power equation of a GG-AWES proposed by Loyd [2] are shown. The aim of this section is to make the reader familiar with the terminology and to introduce the main physical principles used later in this chapter. The main assumptions of this derivation are:

1. The external forces acting on the kite are considered in equilibrium and the inertia forces are insignificant. In this analysis, the mass and the trajectory are neglected. However, in many efficient systems, the effects of these are small during the production phase [22] [23] [24].
2. The tether is considered straight and without mass.

3. The power equation is describing only the production phase. Thus, when considering the whole cycle, the power output is lower.

The last two assumptions will be addressed later in this section, with additional models available in literature.

3.1.1 Derivation

Considering Figure 3.1, the wind is blowing from left to right (along the x-axis) and the kite is moving out of the page (along the y-axis). The wind speed seen from the kite is reduced by the factor $\cos(\theta)$, where θ represents the inclination of the tether at the connection with the kite ($V_{w\parallel} = V_w \cos\theta$).

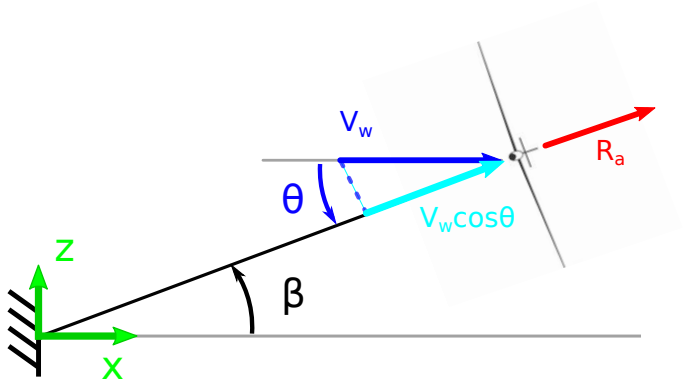

Figure 3.1: Tether elevation and relative wind velocity seen from the kite.

Looking at Figure 3.2, L represents the kite lift, D the drag and R_a the resultant aerodynamic force. The tether force T is equal to the resultant aerodynamic force R_a. V_{out} is the reel-out velocity of the tether. The wind speed along the tether direction seen from the kite is therefore: $V_r = V_{w\parallel} - V_{out}$. The power for a GG-AWES can be found by multiplication of the tether force T and the reel-out velocity V_{out} [2]:

$$P_{GG} = T \cdot V_{out} \tag{3.1}$$

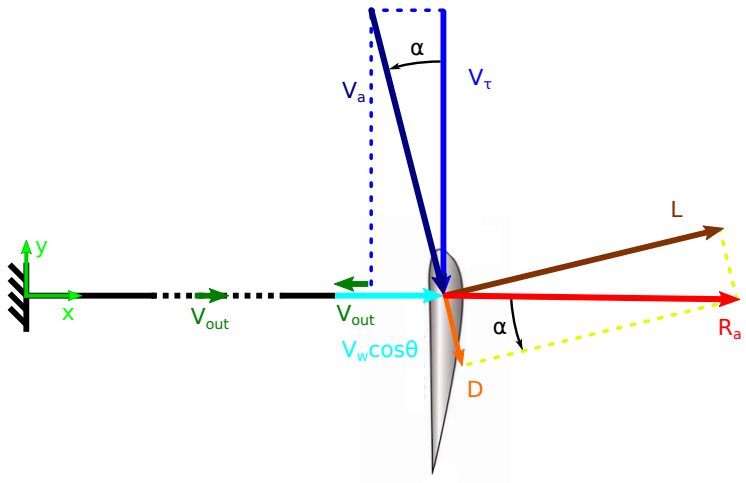

Figure 3.2: Velocity triangle and aerodynamic forces seen from the top for a GG-AWES.

Considering that the system is in equilibrium, R_a is in the opposite direction of the tether and D is parallel to the relative velocity V_a, the following proportion can be found:

$$\frac{L}{D} = \frac{\frac{1}{2}\rho_{air} A C_L V_a^2}{\frac{1}{2}\rho_{air} A C_d V_a^2} = \frac{C_L}{C_d} = \frac{V_\tau}{V_r} \tag{3.2}$$

Where ρ_{air} is the air density, A the kite lifting area, C_L and C_d are lift and drag coefficient of the kite and V_a is the relative wind velocity seen from the kite.

The tangential velocity V_τ can be expressed as a function of the wind speed, the aerodynamic coefficients and the reel-out velocity:

$$V_\tau = V_r \cdot \frac{C_L}{C_d} = (V_{w\parallel} - V_{out}) \cdot \frac{C_L}{C_d} \tag{3.3}$$

Defining the glide ratio $G_e = \frac{C_L}{C_d}$ the relative velocity is:

$$V_a^2 = \big((V_{w\parallel} - V_{out}) \cdot G_e\big)^2 + \big(V_{w\parallel} - V_{out}\big)^2 = (V_{w\parallel} - V_{out})^2 \cdot (1 + G_e^2) \tag{3.4}$$

The tether force, as function of the reel-out speed, is:

$$\begin{aligned} T = R_a &= \sqrt{L^2 + D^2} = \frac{1}{2}\rho_{air}\ A\ C_d \sqrt{1 + \frac{C_L^2}{C_d^2}} \cdot (V_{w\parallel} - V_{out})^2\ \left(1 + G_e^2\right) \\ &= \frac{1}{2}\rho_{air}\ A\ C_d\ (V_{w\parallel} - V_{out})^2\ \left(1 + G_e^2\right)^{3/2} \end{aligned} \tag{3.5}$$

The power equation can now be derived:

$$\boxed{P_{GG} = T \cdot V_{out} = \frac{1}{2}\rho_{air}\ A\ C_d\ (V_{w\parallel} - V_{out})^2\ V_{out}\ \left(1 + G_e^2\right)^{3/2}} \tag{3.6}$$

By taking the derivative of P_{GG} with respect to V_{out}, it can be demonstrated that the maximum power is harvested when $V_{out} = V_{w\parallel}/3$. The maximum power is:

$$P_{GG,max} = \frac{4}{27} P_w\ \cos\theta^3\ A\ C_d\ \left(1 + G_e^2\right)^{3/2} \tag{3.7}$$

With the power density:

$$P_w = \frac{1}{2}\rho_{air} V_w^3 \tag{3.8}$$

Considering high glide ratios, the power output can be approximated as:

$$P_{GG,max} \approx \frac{4}{27} P_w\ \cos\theta^3\ A\ C_L\ G_e^2 \tag{3.9}$$

When the production power is maximised ($V_{out} = V_{w\parallel}/3$), the tether force becomes:

$$T_{GG,max} = \frac{2}{9}\rho_{air}\ A\ V_w^2 \cos\theta^2 C_d\ \left(1 + G_e^2\right)^{3/2} \tag{3.10}$$

Given the importance of C_L, glide ratio and elevation, additional models are developed for these terms.

3.1.2 Finite wing aerodynamics

To model the aerodynamics of a finite wing, Pradtl lifting-line theory [25] is considered. With this theory, the lift and drag coefficient of a wing can be found, given the properties of the airfoil and the aspect ratio $AR = \frac{s^2}{A}$ (s is the wing span and A the area).

With the assumption of elliptical wing, the lift distribution along the span is also elliptical and the downwash velocity is constant for the whole wing [25]. Considering thin airfoils the slope of the lift coefficient C_L with respect to the angle of attack (a_0) can be approximated to $a_0 \approx 2\pi$.

With these considerations, the aircraft drag has a component of induced drag. It is function of the square of the lift coefficient and of the wing aspect ratio:

$$Cd_i = \frac{C_L^2}{\pi ARe} \tag{3.11}$$

where e is the Oswald efficiency, considered to be 0.9 [26][1].

3.1.3 Additional drag due to the tether

Since the power is increasing with the square of G_e, particular attention should be given to the estimation of the glide ratio. The drag coefficient is representative of the drag of the whole system, not only of the kite itself. Thus, a contribution from the tether has to be evaluated.

The line normal force per length dF (crossflow principle) is given by:

$$dF = \frac{1}{2}\rho_{air} d\, C_\perp V_n^2 \tag{3.12}$$

where the diameter is indicated by d, the perpendicular aerodynamic drag coefficient of the tether by $C_\perp$ and the tether transverse velocity by V_n.

V_n is equal to V_τ at the kite level and null at the ground: $V_n = V_\tau \frac{l}{r}$. r is the tether length and l the tether longitudinal coordinate. The equivalent force acting on the kite can be found matching the torque around the generator point [22]:

$$\begin{aligned} F_{tether} \cdot r &= \frac{1}{2}\rho_{air} d\, C_\perp \int_0^r \left(\frac{V_\tau l}{r}\right)^2 l\, dl \\ F_{tether} &= \frac{1}{2}\rho_{air} d\, C_\perp\, V_\tau^2\, \frac{r}{4} \end{aligned} \tag{3.13}$$

The additional drag coefficient is then [22]:

$$C_{d,tether} = C_\perp\, \frac{d\, r}{4\, A} \tag{3.14}$$

Finally the total drag is expressed as:

$$C_d = C_{d0} + \frac{C_L^2}{\pi ARe} + \frac{C_\perp dr}{4A} \tag{3.15}$$

C_{d0} is the drag coefficient at zero lift of the kite. The second term represents the lift induced drag introduced in the previous section.

[1] For a straight infinite wing $e = 1$. Non-ideal load shapes for a flat wing make the Oswald efficiency to become smaller. Non-planar wings, for instance winglets, can have $e > 1$. This expression can thus be used to simulate all kinds of different wing shapes.

3.1.4 Elevation angle & tether sag

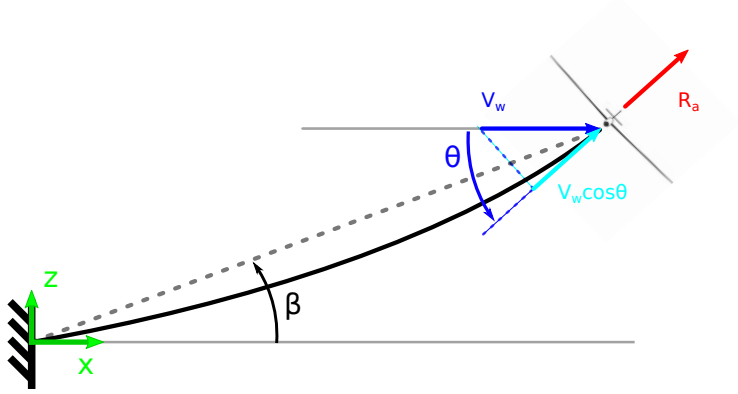

Figure 3.3: Tether elevation β, wind speed and total aerodynamic force on a kite flying crosswind considering the tether sag. θ is the inclination of the tether at the kite connection.

The tether sag can be found by considering the mass per unit length of the tether and the normal force. The mass per unit length is:

$$m_r = A_\sigma \rho_\sigma + \eta_{is} A_{el} \rho_{el} \tag{3.16}$$

Where the tether area A_σ represents the section carrying the load, the electric cable area A_{el} transmits the power onboard generated. The term η_{is} takes into account the isolation coating needed for the cable [3]. ρ_σ and ρ_{el} are respectively the mass densities of the structural and electrical material.

To model the inclination of the tether at the kite connection, the tether sag is approximated with a parabola [3]. Using a parabola instead of the catenary curve is a good approximation with small sag [27]. Considering the parabola equation $z = a\ x^2 + a\ b\ x$, the a term is given by [27]:

$$a = \frac{m_r \cdot g}{2T} \tag{3.17}$$

where T is the tether force and g the gravity acceleration. The b term is [27]:

$$b = \frac{\tan\beta}{2a} - \frac{r\cos\beta}{2} \tag{3.18}$$

Finally, the angle between the tether and the x axis at the kite point is [27]:

$$\theta = \arctan\left(2a(r\cos\beta + b)\right) \tag{3.19}$$

3.1.5 Influence of the recovery phase

To maximize the cycle power, the power equation of production and of recovery phases should be included into one model.

Considering Eq. (3.6), a non-dimensional coefficient $\gamma_{out} = \frac{V_{out}}{V_w}$ can be used to express the power equation during the production phase:

$$P_{pr} = P_w\ A\ \gamma_{out}\ (cos(\theta) - \gamma_{out})^2\ C_d\ \left(1 + G_e^2\right)^{3/2} \tag{3.20}$$

with $P_w = \frac{1}{2}\rho_{air} V_w^3$ (Eq. (3.8)).

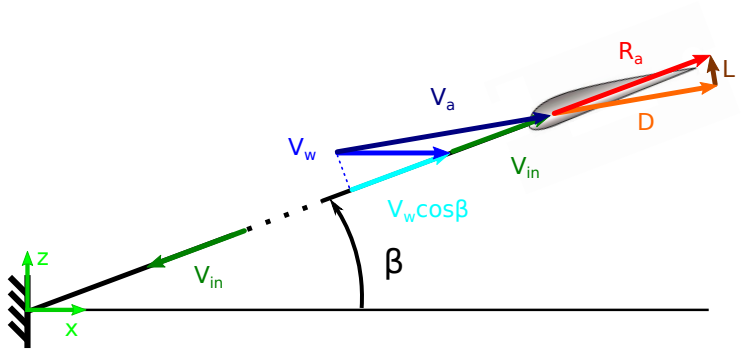

Figure 3.4: Velocity triangle and aerodynamic forces during the reel-in phase. β is the tether elevation.

More strategies are available for the retraction phase [28], the one modelled in this work is possible only for a solid aircraft. It is assumed that the kite is brought back to the initial position with a straight path (Figure 3.4) [29]. This solution is not suitable for a soft kite, because the wing cannot be oriented in this configuration and the reel-in forces would be too high for an efficient overall power production [30]. The transition phases between production and recovery are neglected. The relative velocity seen from the kite is:

$$V_a^2 = V_w^2 + V_{in}^2 + 2V_w V_{in} \cos\beta \tag{3.21}$$

Where $V_{in} = \gamma_{in} V_w$. Assuming the kite to be in equilibrium during the reel-in, the aerodynamic resultant force R_a lays along the tether direction and D is parallel to V_a, the angle between V_a and the tether is equal to the angle between R_a and D:

$$\frac{L}{D} = \frac{V_w \sin\beta}{V_w \cos\beta + V_{in}} = \frac{\sin\beta}{\cos\beta + \gamma_{in}} \tag{3.22}$$

The tether force during the retraction phase is then:

$$T_r = \sqrt{D^2 + L^2} = D\sqrt{1 + \left(\frac{\sin\beta}{\cos\beta + \gamma_{in}}\right)^2} \tag{3.23}$$

Considering that β is typically less that 30° and γ_{in} typically above 1, a good approximation is $R_a \approx D$ [29]. Thus:

$$\begin{aligned} T_r &= \frac{1}{2}\rho_{air} A\, C_{d0} \left(V_w^2 + V_{in}^2 + 2V_w V_{in}\cos\beta\right) \\ &= \frac{1}{2}\rho_{air}\, V_w^2 A\, C_{d0} \left(1 + \gamma_{in}^2 + 2\gamma_{in}\cos\beta\right) \end{aligned} \tag{3.24}$$

The power spent during the recovery is then:

$$P_r = P_w\ A\ C_{d0}\ \gamma_{in}\ \left(1 + \gamma_{in}^2 + 2\gamma_{in}\cos\beta\right) \tag{3.25}$$

The mean power can be finally derived, considering that the ratio between the production time and the recovery is proportional to the ratio between reel-out and reel-in velocities. The ratio of the time of the production phase τ_{out} and of the recovery phase τ_{in} are:

$$\tau_{out} = \gamma_{in}/(\gamma_{in} + \gamma_{out}) \qquad \tau_{in} = \gamma_{out}/(\gamma_{in} + \gamma_{out}) \tag{3.26}$$

The mean power can now be derived, considering Eq. (3.20):

$$\begin{aligned} P_{cycle} =& P_{pr}\ \tau_{out} - P_r\ \tau_{in} \\ =& P_w A \left((cos(\theta) - \gamma_{out})^2\ C_d\ \left(1 + G_e^2\right)^{3/2} - C_{d0} \left(1 + \gamma_{in}^2 + 2\gamma_{in} \cos\beta\right) \right) \cdot \\ & \left(\frac{\gamma_{in}\gamma_{out}}{\gamma_{in} + \gamma_{out}} \right) \end{aligned} \tag{3.27}$$

The maximum value of the mean power output during a cycle is then the maximum value of the function $P_{cycle}(\gamma_{in}, \gamma_{out})$.

3.1.6 Other losses

To model the efficiency of the conversion from mechanical to electric power and to take into account a power loss due to trajectory, some efficiency factors are introduced. During the reel-out phase, the losses due to conversion are:

$$\eta_{out} = \eta_{gen}\eta_{tr} \tag{3.28}$$

Where η_{gen} is the electric generator efficiency and η_{tr} the trajectory efficiency

During the reel-in phase, the power loss due to motor and to the batteries on the ground that store energy:

$$\eta_{in} = \eta_{mot}\eta_{batt} \tag{3.29}$$

Where η_{mot} is the efficiency of the generator used as a motor. η_{batt} is the efficiency of the storage of the power used during the reel-in, if this strategy is used. This efficiency η_{in} can be additionally reduced, to consider the transition phases and the low model accuracy with a low efficiency.

Finally the power equation for the cycle power:

$$\begin{aligned} P_{cycle} = P_w A \Big[& \eta_{out}\ (cos(\theta) - \gamma_{out})^2\ C_d\ \left(1 + G_e^2\right)^{3/2} - \\ & - \frac{C_{d0}}{\eta_{in}} \left(1 + \gamma_{in}^2 + 2\gamma_{in} \cos\beta\right) \Big] \cdot \left(\frac{\gamma_{in}\gamma_{out}}{\gamma_{in} + \gamma_{out}} \right) \end{aligned} \tag{3.30}$$

3.2 Power equation of Fly-Gen Airborne Wind Energy System

The power equation for a FG-AWES can be derived taking the same assumptions listed at the beginning of Section 3.1.

3.2.1 Derivation

Considering Figure 3.1, the wind is blowing from left to right (along the x-axis) and the kite is moving out of the page (along the y-axis). The wind speed seen from the kite is reduced of the factor $\cos(\theta)$, where θ represents the inclination of the tether at the connection with the kite ($V_{w\|} = V_w \cos\theta$).

The velocity triangle and the force balance for a Fly Generation Airborne Wind Energy System are presented in Figure 3.5.

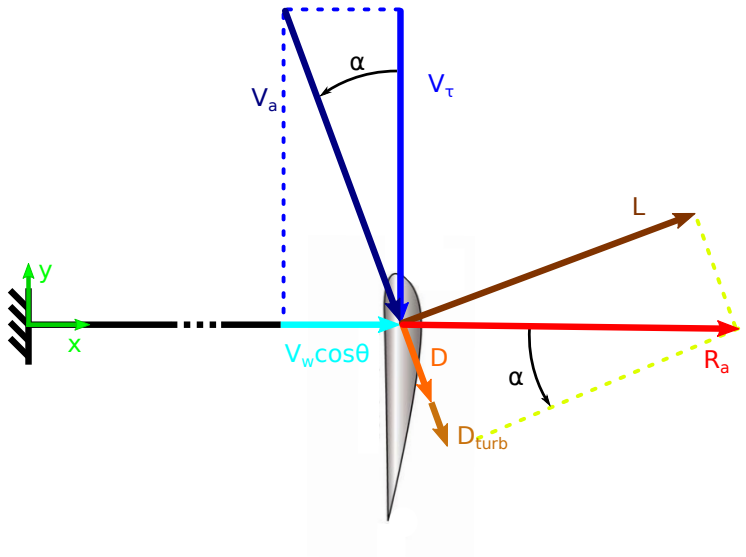

Figure 3.5: Velocity triangle and aerodynamic forces seen from the top for a FG-AWES.

The presence of on-board turbines, extracting power, can be modelled as an additional drag D_{turb} applied to the kite. The maximum possible power is:

$$P_{FG} = D_{turb} \cdot V_a \tag{3.31}$$

Considering that the system is in equilibrium, R_a is in the opposite direction of the tether and D and D_{turb} are parallel to the relative velocity V_a, the following proportion can be found:

$$\frac{L}{D + D_{turb}} = \frac{\frac{1}{2}\rho_{air} A C_L V_a^2}{D + D_{turb}} = \frac{V_\tau}{V_{w\|}} \tag{3.32}$$

Where L is the lift force and D the drag.

D_{turb} can be formulated considering the kite area A as reference:

$$D_{turb} = \frac{1}{2}\rho_{air} A C_{d\,turb} V_a^2 \tag{3.33}$$

Defining $\gamma_t = D_{turb}/D_{kite} = C_{d\,turb}/C_d$, the relative wind velocity is:

$$V_a^2 = V_{w\|}^2 + \left(V_{w\|}\frac{L}{D_{kite} + D_{turb}}\right)^2 = V_{w\|}^2\left(1 + \left(\frac{Ge}{1+\gamma_t}\right)^2\right) \tag{3.34}$$

Considering Eq. (3.31), the ideal power production for a FG-AWES is:

$$P_{FG} = \left(\frac{1}{2}\rho_{air} A\, C_{d,turb}\, V_{w\|}^2\left(1 + \left(\frac{Ge}{1+\gamma_t}\right)^2\right)\right) \cdot \left(V_{w\|}\sqrt{1 + \left(\frac{Ge}{1+\gamma_t}\right)^2}\right)$$

$$\boxed{P_{FG} = P_w A\, \gamma_t\, C_d\, \cos\theta^3 \left(1 + \left(\frac{Ge}{1+\gamma_t}\right)^2\right)^{3/2}} \tag{3.35}$$

Where $P_w = \frac{1}{2}\rho_{air}\, V_w^3$.

By taking the derivative of P_{FG} with respect to γ_t, it can be demonstrated that for high glide ratios the maximum power is harvested when $D_{turb} = D_{kite}/2$ (i.e. $\gamma_t = 1/2$), thus the maximum power production for a FG-AWES is [2]:

$$P_{FG,max} \approx \frac{4}{27}\, P_w A\, \cos\theta^3\, C_L\, G_e^2 \tag{3.36}$$

It can be seen that the power equation with the assumption of high glide ratio is the same for a FG-AWES as it is for a GG-AWES (eq. (3.9)).

The tether force can be derived, considering the vectorial summation of the lift and drag forces:

$$\begin{aligned} T &= \frac{1}{2}\rho_{air}\, A\, \sqrt{(C_d(1+\gamma_t))^2 + C_L^2} \cdot V_{w\|}^2 \left(1 + \left(\frac{Ge}{1+\gamma_t}\right)^2\right) \\ &= \frac{1}{2}\rho_{air}\, V_w^2\, A\, C_d(1+\gamma_t)\, \cos\theta^2 \left(1 + \left(\frac{Ge}{1+\gamma_t}\right)^2\right)^{3/2} \end{aligned} \tag{3.37}$$

The tether force at the maximum production ($\gamma_t = 1/2$) and for high glide ratio is:

$$T_{FG,max} \approx \frac{2}{9}\rho_{air}\, A\, C_L\, G_e V_w^2 \cos\theta^2 \tag{3.38}$$

3.2.2 Additional drag due to the tether & tether sag

The influence of the tether on the total drag and the tether sag are the same as for GG-AWES, thus the equations in Section 3.1.2, 3.1.3 and 3.1.4 can be used.

3.2.3 Other losses

Later in this chapter, a model for the disc theory power losses and for the power losses due to mass are included. At this stage, to take into account the efficiency of the turbine, the power losses due to mass, trajectory and the power transmission, an efficiency η_t can be defined.

Finally, the maximum power that can be harvested for high glide ratio is:

$$P_{FG,max} = \frac{4}{27}\, \eta_t\, P_w\, A\, C_L\, G_e^2\, \cos\theta^3 \tag{3.39}$$

3.3 Unified model

3.3.1 Derivation

In this section, the power equation for a system with ground and on-board generation is derived.

Considering Figure 3.6, the wind speed seen from the kite is reduced of the factor $\cos(\theta)$, where θ represents the inclination of the tether at the connection with the kite ($V_{w\|} = V_w \cos\theta$). V_{out} represents the reel-out velocity, D_{turb} the drag induced by the on-board turbines and V_a the relative wind velocity. In equilibrium, the tether force is equal to the aerodynamic force $T = R_a$. The power production in this model has two contributions:

$$\boxed{P = T \cdot V_{out} + D_{turb} \cdot V_a} \tag{3.40}$$

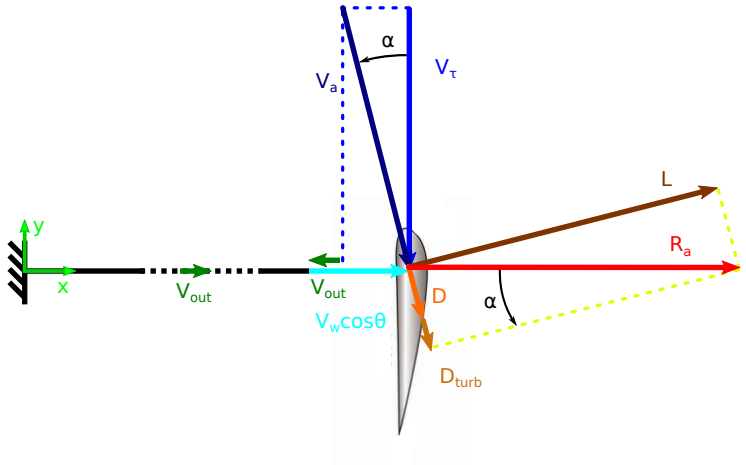

Figure 3.6: Velocity triangle and aerodynamic forces seen from the top for a generic crosswind AWES.

To find a power equation for this system, all the terms in the latter equation should be re-formulated. Considering the proportions between forces and velocities, the relative velocity V_a can be expressed as:

$$V_a^2 = \left(V_{w\parallel} - V_{out}\right)^2 + \left(\left(V_{w\parallel} - V_{out}\right)\frac{C_L}{C_d + C_{d,turb}}\right)^2 \tag{3.41}$$

Where C_L and C_d are defined in Section 3.1.2 and 3.1.3, they take into account the tether and the finite wing. Defining $\gamma_{out} = \frac{V_{out}}{V_w}$ and $\gamma_t = \frac{C_{d,turb}}{C_d}$:

$$\boxed{V_a^2 = V_w^2 \left(\frac{\cos\theta - \gamma_{out}}{1+\gamma_t}\right)^2 \left((1+\gamma_t)^2 + Ge^2\right)} \tag{3.42}$$

A general expression for the aerodynamic force can be found with a vectorial summation of the lift and drag forces:

$$\begin{aligned} R_a &= \sqrt{(D + D_{turb})^2 + L^2} \\ &= \frac{1}{2}\rho_{air} A \sqrt{C_L^2 + (C_d + C_{d,turb})^2} \cdot V_a^2 \\ &= \frac{1}{2}\rho_{air}\ A\ C_d\ \sqrt{(1+\gamma_t)^2 + Ge^2} \cdot V_w^2 \left(\frac{\cos\theta - \gamma_{out}}{1+\gamma_t}\right)^2 \left((1+\gamma_t)^2 + Ge^2\right) \end{aligned}$$

$$\boxed{R_a = \frac{1}{2}\rho_{air}\ A\ C_d\ V_w^2 \left(\frac{\cos\theta - \gamma_{out}}{1+\gamma_t}\right)^2 \left((1+\gamma_t)^2 + Ge^2\right)^{3/2}} \tag{3.43}$$

The drag force due to the turbines $D_{turb} = \frac{1}{2}\rho_{air}\ A\ \gamma_t C_d\ V_a^2$ can be expressed as:

$$\boxed{D_{turb} = \frac{1}{2}\rho_{air}\ A\ \gamma_t\ C_d\ V_w^2 \left(\frac{\cos\theta - \gamma_{out}}{1+\gamma_t}\right)^2 \left((1+\gamma_t)^2 + Ge^2\right)} \tag{3.44}$$

The power equation of the ground generated power P_{gr} can be expressed as the product

between the tether force T and the reel-out speed V_{out}:

$$\begin{aligned} P_{gr} =& \left[\frac{1}{2}\rho_{air}\ A\ C_d\ V_w^2\ \left(\frac{\cos\theta-\gamma_{out}}{1+\gamma_t}\right)^2\left((1+\gamma_t)^2+Ge^2\right)^{3/2}\right]\cdot\left[V_w\gamma_{out}\right]= \\ =& \frac{1}{2}\rho_{air}\ A\ C_d\ V_w^3\ \gamma_{out}\ \left(\frac{\cos\theta-\gamma_{out}}{1+\gamma_t}\right)^2\left((1+\gamma_t)^2+Ge^2\right)^{3/2} \end{aligned} \tag{3.45}$$

The power generated on board P_{ob} can instead be expressed as the product between drag produced by the on-board turbines D_{turb} and the relative velocity V_a:

$$\begin{aligned} P_{ob} =& \left[\frac{1}{2}\rho_{air}\ A\ \gamma_t\ C_d\ V_w^2\ \left(\frac{\cos\theta-\gamma_{out}}{1+\gamma_t}\right)^2\left((1+\gamma_t)^2+Ge^2\right)\right]\cdot \\ & \left[V_w\ \left(\frac{\cos\theta-\gamma_{out}}{1+\gamma_t}\right)\sqrt{(1+\gamma_t)^2+Ge^2}\right]= \\ =& \frac{1}{2}\rho_{air}\ A\ C_d\ V_w^3\ \gamma_t\ \left(\frac{\cos\theta-\gamma_{out}}{1+\gamma_t}\right)^3\left((1+\gamma_t)^2+Ge^2\right)^{3/2} \end{aligned} \tag{3.46}$$

Finally, the total power during the production phase is the sum of P_{gr} and P_{ob}:

$$\boxed{P_{out} = \frac{1}{2}\rho_{air}\ A\ V_w^3\ C_d\ \left((1+\gamma_t)^2+Ge^2\right)^{3/2}\left[\gamma_{out}\ \left(\frac{\cos\theta-\gamma_{out}}{1+\gamma_t}\right)^2+\gamma_t\ \left(\frac{\cos\theta-\gamma_{out}}{1+\gamma_t}\right)^3\right]} \tag{3.47}$$

For high glide ratio, the latter equation can be formulated as:

$$P_{out} \approx \frac{1}{2}\rho_{air}\ A\ C_L\ G_e^2\ V_w^3\left[\gamma_{out}\left(\frac{\cos\theta-\gamma_{out}}{1+\gamma_t}\right)^2+\gamma_t\left(\frac{\cos\theta-\gamma_{out}}{1+\gamma_t}\right)^3\right] \tag{3.48}$$

It can be demonstrated that the power equation for Ground Generation Airborne Wind Energy System and for Fly Generation Airborne Wind Energy System are special cases of this last general power equation. The case with $\gamma_t = 0$ and $\gamma_{out} = \cos\theta/3$ describes the maximum power for GG-AWES, while with $\gamma_t = 1/2$ and $\gamma_{out} = 0$ the power for FG-AWES.

To conclude the unified derivation of the power output, the recovery phase should be considered (Section 3.1.5). Equation (3.24) is then necessary to model the power during the reel-in phase.

The mean power over a cycle is then:

$$\begin{aligned} P_{cycle} =& \frac{\gamma_{in}}{\gamma_{in}+\gamma_{out}}\cdot P_{out}+ \\ & -\frac{\gamma_{out}}{\gamma_{in}+\gamma_{out}}\left(\frac{1}{2}\rho_{air}\ A\ V_w^3\ \gamma_{in}\ C_{d0}\left(1+\gamma_{in}^2+2\gamma_{in}\cos\beta\right)\right) \end{aligned} \tag{3.49}$$

Finally, considering Eq (3.47) the power equation of a generic crosswind AWES can be written as:

$$\boxed{\begin{aligned} P_{cycle} =& \frac{1}{2}\rho_{air}\ A\ V_w^3\left[C_d\ \left((1+\gamma_t)^2+Ge^2\right)^{3/2}\ \left(\left(\frac{\cos\theta-\gamma_{out}}{1+\gamma_t}\right)^2+\frac{\gamma_t}{\gamma_{out}}\left(\frac{\cos\theta-\gamma_{out}}{1+\gamma_t}\right)^3\right)+\right. \\ & \left.-C_{d0}\left(1+\gamma_{in}^2+2\gamma_{in}\cos\beta\right)\right]\cdot\frac{\gamma_{in}\gamma_{out}}{\gamma_{in}+\gamma_{out}} \end{aligned}} \tag{3.50}$$

3.3.2 Example

To understand the influence of the glide ratio G_e on the power equation (3.47), Figures 3.7 show how the power varies with γ_t and γ_{out} for a glide ratio of 5 and of 15. Considering only on-board generation ($\gamma_{out} = 0$) and high G_e (Figure 3.7a), the highest power can be harvested with $\gamma_t \approx 1/2$. The region ranging from 0.42 and 0.60 has a power higher that 99 % of the maximum, highlighting that the neighbour of the maximum is an almost flat region. With a decrease of G_e (Figure 3.7b) the optimum value of γ_t increases. Considering only ground generation ($\gamma_t = 0$), the optimum is always at $\gamma_{out} = \cos(\theta)/3$.

For low glide ratios, a FG-AWES can reach higher powers compared to a GG-AWES. This is due to the presence of the term $\left((1+\gamma_t)^2 + Ge^2\right)^{3/2}$ in Equation (3.47).

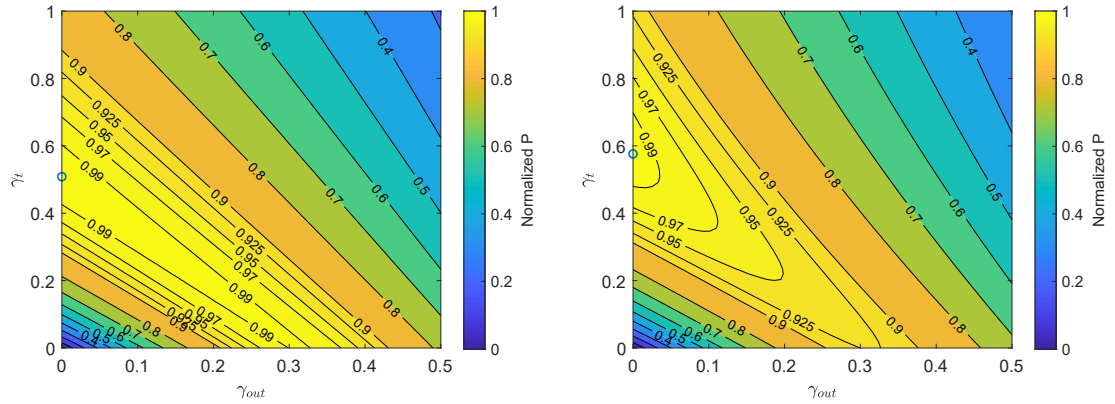

(a) (b)

Figure 3.7: Normalized power during the generation phase as function of γ_{out} and γ_t for $\theta = 20°$ for $G_e = 15$ (a) and $G_e = 5$ (b).

3.4 Mass model

In this section, a mass model is introduced. There are many reasons for the introduction of a mass model, all of them aim to penalize heavy designs. A high mass kite should be penalized because it can hardly be built (i.e. really high aspect ratio and high lift coefficients), it needs more power to take off and has relevant power losses due to gravity.

Many designs are possible for the manufacturing of the kite, thus the structural model should be general enough to capture the main physics. Later, through a sensitivity analysis the influence of the structural model on the power output is investigated. Only hard kites are represented by the model proposed in this work.

In Figure 3.8, an approximation of the loads on the wings is shown. It is assumed that the aerodynamic load has an elliptical distribution, following the assumptions introduced during the aerodynamic modelling (Section 3.1.2).

The wings should be designed for the maximum aerodynamic forces. Therefore, the integral of the distributed load is equal to the maximum aerodynamic force $Ra_{max} = \int_0^s q_{aer}(x_w)dx_w$. It can be described by:

$$q_{aer}(x_w) = \frac{4}{\pi}\frac{Ra_{max}}{s}\sqrt{1-\left(\frac{2x_w}{s}-1\right)^2} \tag{3.51}$$

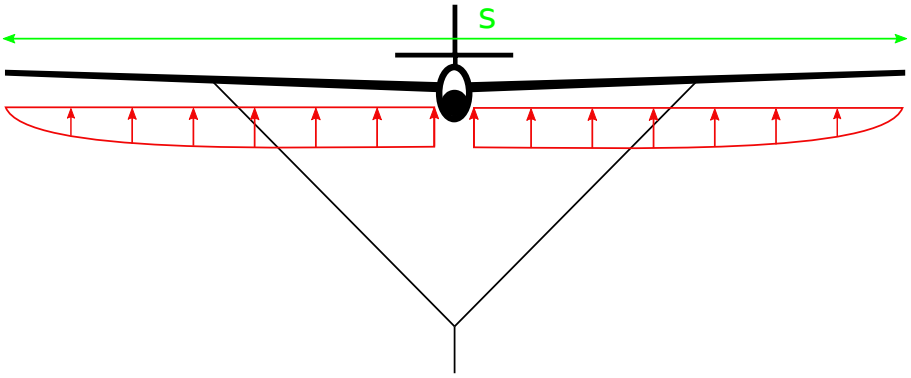

Figure 3.8: Aerodynamic load on the kite wing.

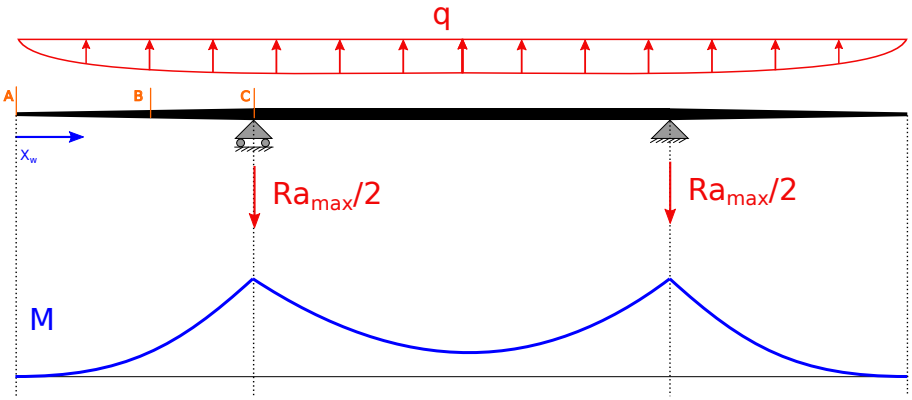

Figure 3.9: Loads on the wing, represented as a simply supported beam.

To lighten the structure, the tether is often split in two and connected to the structure as in Figure 3.8. The wings can be represented by a simply supported beam. The connection of the tether with the structure can be considered a support since it is constraining the structure displacement but not the rotation.

With this simplification, the bending moment distribution can be found, as function as the distributed load $q_{aer}(x_w)$ and of the support position x_c. The bending moment, given by the the aerodynamic load, can be computed as:

$$M_x^{(aero)}(x_w) = \int_{x=0}^{x=x_w} (x - x_w) q_{aer}(x) dx \tag{3.52}$$

Performing the variable substitution $t = \frac{2x}{s} - 1$, the integral can be solved:

$$\begin{aligned} M_x^{(aero)}(t_w) &= \frac{Ra_{max} s}{\pi} \int_{t=-1}^{t=t_w} (t - t_w)\sqrt{1-t^2}\, dt \\ &= -\frac{Ra_{max} s}{\pi} \left(\frac{\pi t_w}{4} + \frac{t_w^2 \sqrt{(1-t_w^2)}}{6} + \frac{t_w \arcsin(t_w)}{2} + \frac{\sqrt{(1-t_w^2)}}{3} \right) \end{aligned} \tag{3.53}$$

The contribution on the bending moment, given by the reaction forces of the supports, is instead linear with the distance:

$$M_x^{(support)} = -\frac{Ra_{max}}{2}(x_c - x_w) \qquad x_w > x_c \tag{3.54}$$

Once the loads are found, a model for the structure should be considered.

The structures that withstand the load are considered to be the spar caps. In the aerospace industry wings are usually manufactured to carry normal load with booms, here represented by spar caps. In Figure 3.10 the spar caps dimensions of a generic section are shown.

It should be remarked that the height h and the width b are considered functions of the chord ($h = 0.1c$, $b = 0.25c$), which has an elliptical trend:

$$c(x_w) = \frac{4A}{\pi s}\sqrt{1 - \left(\frac{2x_w}{s} - 1\right)^2} \tag{3.55}$$

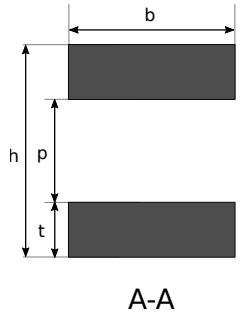

Figure 3.10: Spar cap dimensions.

The inertia can be found:

$$I(x_w) = \frac{bh^3}{12} - \frac{bp^3}{12} \tag{3.56}$$

Once the inertia is found, the stress in the spar caps can be compared to the strength of the material (usually carbon fibre-epoxy composite material):

$$\sigma_{lim} > \frac{h/2 \cdot M_x}{I} \tag{3.57}$$

Where σ_{lim} in this work is fixed to 570 MPa, typical value of carbon fibre-epoxy composite material. An other constraint should be set on the displacement, which can be found with a double integration of the curvature:

$$\delta = \int_0^s \int_0^s \frac{M}{EI} dx_w + Ax + B \tag{3.58}$$

Where E is the material Young Modulus, in this work fixed to 70 GPa, typical value of carbon fibre-epoxy composite material. The integration constants A and B can be found by setting the boundary conditions:

$$\frac{d\delta(x_w = s/2)}{dx} = 0 \qquad \delta(x_w = x_c) = 0 \tag{3.59}$$

In Figure 3.11, a typical trend of the aerodynamic load (q_{aer}), of the bending moment applied to the wing M_x and of the deflection δ are shown.

Finally, the structural mass of the wing can be found:

$$m_{wing} = 2 \cdot \rho_{carbon} \cdot \int_0^s b(x_w) \cdot t(x_w) dx_w \tag{3.60}$$

In this work, no constraint on the buckling is considered.

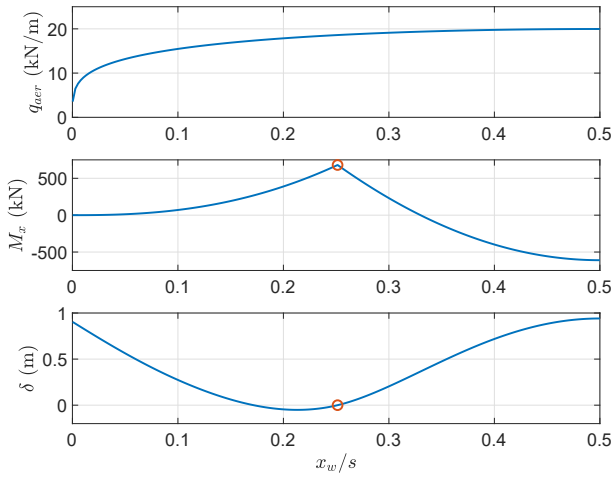

Figure 3.11: Typical aerodynamic load, bending moment and deflection along half span. The red circle highlights the support position.

The total flying mass takes into account the mass of the structural material not included in the model, the mass of the power electronic, the mass of the tether and the additional mass of the take off system.

The mass of the structural material, not included in the model (wing skin, shear webs, support structure, fuselages), is considered a fixed percentage of the spar caps mass. The total aircraft mass is then:

$$m_{gl} = m_{wing} + k \cdot m_{wing} \tag{3.61}$$

The factor k is estimated to be $k \approx 1.5$ [31].

The mass of the power electronic is a function of the power produced on board. It can be approximated with the mass of the generators. Thus, considering a power density of the on board generators, the mass can be found.

The mass needed to take off and to land is instead computed with the model proposed in the following section.

3.5 Take-off model

To complete the flying mass estimation, a model for the take-off has to be included. The aim of this model is to estimate the additional on-board mass needed to take off and to determine which take-off strategy is preferable from a system perspective.

For hard kites, three take-off strategies are studied in literature: vertical take-off with rotors, rotational take-off and linear take-off with on-board propellers. Fagiano [18] shows the key equations for these three methods with respect to GG-AWES. By comparing the power, the additional on-board mass and the area on the ground needed to take off, the author concludes that vertical and linear take-off are favourable, compared with rotational. Thus, in this work these two strategies are considered.

To include the take-off into the optimisation problem, the vertical and linear model are incorporated into one model. The climbing can be characterised by a climb angle α_{TO}, that can vary between low values, simulating a linear take-off, and $\alpha_{TO} = 90°$, representing a vertical take-off. The system is considered in equilibrium and the initial acceleration

phase neglected.

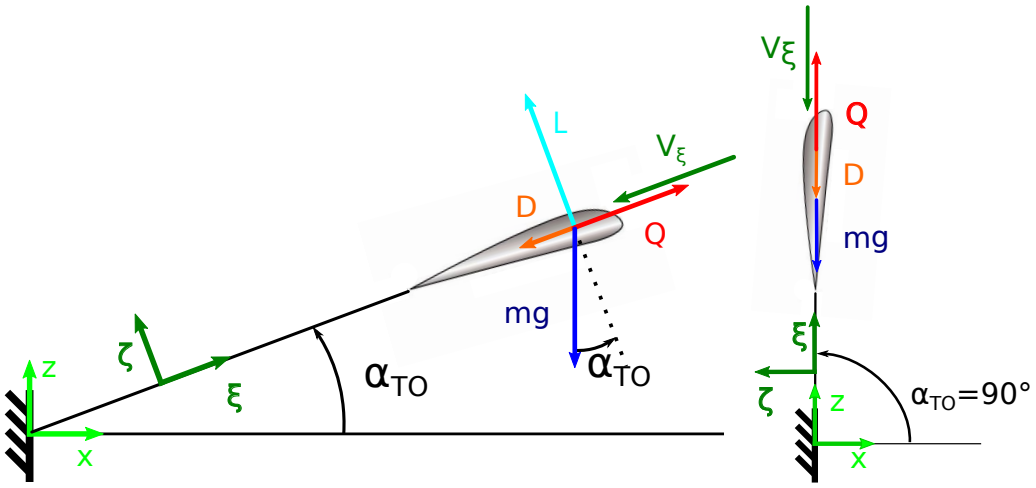

Figure 3.12: Forces acting during linear (a) and vertical (b) the take-off.

Considering Figure 3.12a, a force balance can be written with respect to the coordinate system (ξ, ζ):

$$\begin{cases} Q = D + mg\sin(\alpha_{TO}) \\ L = mg\cos(\alpha_{TO}) \end{cases} \tag{3.62}$$

Q is the thrust force given by the propellers, D and L the aerodynamic drag and lift, m the flying mass and g the gravitational acceleration. The wind velocity is neglected, following the assumption from [18]. This assumption is conservative, since a take-off facing the wind requires less power. The C_L is considered the maximum used during the production phase. The drag coefficient C_d does not include the tether contribution, because the tether is considered parallel to the kite climbing direction: this can be considered true during the first part of the climbing. An accurate modelling would include a variable mass to account for the changing mass of the tether. The total mass of the tether is instead assumed always active. The tether tension, necessary to have a reasonable sag, is neglected in Equation (3.62).

From the second equation, the climbing velocity can be found:

$$V_\xi = \sqrt{\frac{2mg\cos(\alpha_{TO})}{\rho_{air} A C_L}} \tag{3.63}$$

The first equation gives an expression for the necessary thrust Q.

In the extreme case of vertical take off (Figure 3.12b), the second equation loses meaning, the thrust force can be set to a multiple of the gravity force.

The thrust needed to take off Q can be provided by on-board turbines $Q_{(turb)}$, used as propellers, and at the same time by propellers $Q_{(prop)}$, used only during the climbing phase. To find the power and the additional mass needed to take-off, the first step is to design the turbines area necessary during the production phase. The turbines should be designed to give a thrust force equal to D_{turb} (Eq. (3.44)) during the production phase:

$$D_{turb} = \frac{1}{2}\,\rho_{air} V_a^2 \cdot 4a(1-a)A_{turb} \tag{3.64}$$

Where the right hand side formulation comes from disc theory of wind turbines: a represents the induction factor, A_{turb} the turbine area and V_a the tangential velocity of the kite:

$$V_a^2 = V_w^2 \left(\frac{\cos\theta - \gamma_{out}}{1+\gamma_t}\right)^2 \left((1+\gamma_t)^2 + Ge^2\right)$$

The turbines are considered to be orientated in the same direction as the relative velocity. Defining a minimum allowed efficiency due to disc theory η_d^{min}, the power at the rotor can be defined as:

$$P_{rot} = \frac{1}{2}\,\rho_{air} V_a^3 \cdot 4a(1-a)^2 A_{turb} = \eta_d^{min}\, P_{ob} \tag{3.65}$$

Where P_{ob} (Eq. (3.46)) is the power that would be harvested without disc losses.

Equation (3.64), considering Eq. (3.44), can be reformulated as:

$$4a(1-a)\,A_{turb} = \frac{\frac{1}{2}\rho_{air}\,A\,\gamma_t\,C_d\,V_w^2\,\left(\frac{\cos\theta-\gamma_{out}}{1+\gamma_t}\right)^2\left((1+\gamma_t)^2+Ge^2\right)}{\frac{1}{2}\rho_{air}\,V_w^2\,\left(\frac{\cos\theta-\gamma_{out}}{1+\gamma_t}\right)^2\left((1+\gamma_t)^2+Ge^2\right)} = A\,\gamma_t\,C_d \tag{3.66}$$

In a similar fashion, equation (3.65), considering Eq. (3.46), can be expressed as:

$$\begin{aligned} 4a(1-a)^2\,A_{turb} =& \eta_d^{min}\frac{\frac{1}{2}\rho_{air}\,A\,C_d\,V_w^3\,\gamma_t\,\left(\frac{\cos\theta-\gamma_{out}}{1+\gamma_t}\right)^3\left((1+\gamma_t)^2+Ge^2\right)^{3/2}}{\frac{1}{2}\rho_{air}\,V_w^3\,\left(\frac{\cos\theta-\gamma_{out}}{1+\gamma_t}\right)^3\,\left((1+\gamma_t)^2+Ge^2\right)^{3/2}} \\ =& \eta_d^{min}\,A\,\gamma_t\,C_d \end{aligned} \tag{3.67}$$

A_{turb} can be found, by considering Eq. (3.66):

$$A_{turb} = \max\left(\frac{A\,\gamma_t\,C_d}{4a^{(1)}(1-a^{(1)})}\right) \tag{3.68}$$

Where $\gamma_t(V_w)$ and $C_d(V_w)$ are function of the wind speed. $a^{(1)}$ is found by dividing Equation (3.67) with (3.66):

$$a^{(1)} = 1 - \eta_d^{min} \tag{3.69}$$

Finally the induction factor, for all the wind speeds, can be derived by Eq. (3.66):

$$4a(1-a) = \frac{A\,\gamma_t\,C_d}{A_{turb}} \qquad a = \frac{1-\sqrt{1-\frac{A\,\gamma_t\,C_d}{A_{turb}}}}{2} \tag{3.70}$$

Once the turbine area is evaluated, the propulsion power $P_{t,\,pr}$ that allows the turbine to give the thrust $Q_{(turb)}$ should be computed. To do this, the impulse disc theory can be used to have an upper bound of the efficiency $\eta_{t,\,pr,\,disc}$ [32] of the turbines used as propellers.

Thus, the upper limit for the efficiency given by disc theory is:

$$\eta_{turb,\,prop,\,disc} = \frac{2}{1+\sqrt{1+\frac{Q_{turb}}{1/2\rho_{air}A_{turb}V_\xi^2}}} \tag{3.71}$$

To have a realistic value of thrust, considering that the turbine is likely optimised for the power production phase and not the propulsion, another efficiency should be applied $\eta_{t\,pr}$. Therefore the power necessary to produce the thrust force is:

$$P_{t,\,pr} = \frac{Q_{(turb)}V_\xi}{\eta_{t\,pr}\;\eta_{t,\,pr,\,disc}} \tag{3.72}$$

The remaining thrust $Q_{(prop)} = Q - Q_{(turb)}$ can be given from on-board propellers, with an additional mass. The power requested by the propellers P_{pr} can be estimated in a similar fashion, by assuming a propeller area proportional to the average chord.

The additional mass, needed to take-off, can be found using the energy density of batteries and motors [18]:

$$m_{TO} = P_{prop}\left(\frac{h}{V_z E_{batt}} + \frac{1}{E_{motors}}\right) \tag{3.73}$$

3.6 Influence of flying mass on the power production

3.6.1 Derivation

Once the flying mass is estimated, a model to include the power losses due to mass in the power production is necessary to penalize high mass solution. Referring to Figure 3.13, θ represents the inclination of the tether at the connection with the kite. Thus, the tether force T lays in this direction. The total aerodynamic force R_a has an higher inclination, to compensate the gravity, acting along the vertical direction.

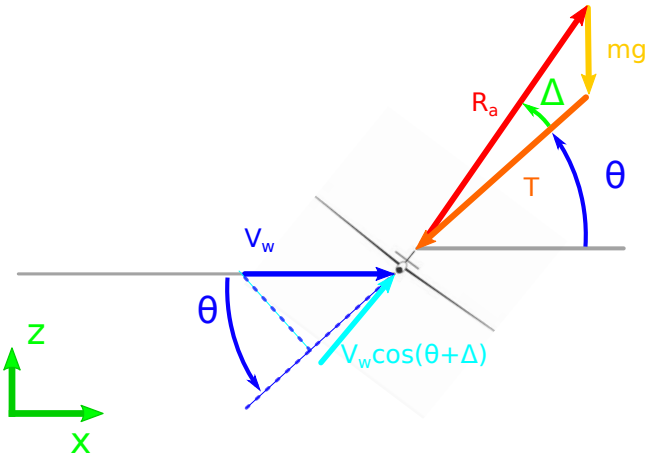

Figure 3.13: Force balance and relative wind velocities considering the mass.

In equilibrium, the forces are in balance. The projections on the x and z axes are:

$$\begin{cases} T\cos(\theta) = R_a\cos(\theta+\Delta) \\ T\sin(\theta) + mg = R_a\sin(\theta+\Delta) \end{cases} \tag{3.74}$$

The sines and cosines can be written again, noticing that Δ is small for a good design:

$$\begin{aligned} \cos(\theta+\Delta) &\approx \cos(\theta) - \Delta(\cos(\theta) + \sin(\theta)) \\ \sin(\theta+\Delta) &\approx \sin(\theta) - \Delta(\sin(\theta) - \cos(\theta)) \end{aligned} \tag{3.75}$$

Modifying eq. (3.74) with these formulations of sines and cosines, the tether traction force is:

$$\begin{cases} T = R_a\left(1 - \Delta - \Delta\tan(\theta)\right) \\ T = R_a\left(1 - \Delta + \frac{\Delta}{tan(\theta)}\right) - \frac{mg}{\sin(\theta)} \end{cases} \tag{3.76}$$

The angle Δ can be derived subtracting the two previous equations:

$$\Delta = \frac{mg}{R_a\cos(\theta)\left(\tan(\theta)^2 + 1\right)} \tag{3.77}$$

Ra is a function itself of the angle Δ (Eq. (3.43) modified into Eq. (3.83)):

$$R_a = \frac{1}{2}\rho_{air}\ A\ C_d\ V_w^2\ \left(\frac{\cos(\theta+\Delta)-\gamma_{out}}{1+\gamma_t}\right)^2 \left((1+\gamma_t)^2+Ge^2\right)^{3/2}$$

Defining, for readability, M^* as:

$$M^* = \frac{mg}{\cos(\theta)\left(\tan(\theta)^2+1\right)} \tag{3.78}$$

and Q^* as:

$$Q^* = \frac{1}{2}\frac{\rho_{air}\ A\ C_d\ V_w^2\ \left((1+\gamma_t)^2+Ge^2\right)^{3/2}}{(1+\gamma_t)^2} \tag{3.79}$$

Eq. (3.77) can be re-written as:

$$\Delta\left(\cos(\theta+\Delta)-\gamma_{out}\right)^2 = \frac{M^*}{Q^*} \tag{3.80}$$

Considering the Taylor series approximation (eq. (3.75)), the angle needed to compensate gravity is finally expressed as:

$$\boxed{\Delta^3\left(\sin\theta+\cos\theta\right)^2 - 2\Delta^2\left(\sin\theta+\cos\theta\right)\left(\cos\theta-\gamma_{out}\right) + \Delta\left(\cos\theta-\gamma_{out}\right)^2 - \frac{M^*}{Q^*} = 0} \tag{3.81}$$

3.6.2 Example

To understand the order of magnitude of the angles, an example is presented. In Table 3.1 the magnitude of the parameters necessary to evaluate the additional inclination Δ is given. The two cases of pure on-board generation (case FG) and ground generation (case GG) are investigated. For these two cases the angles are:

Case FG $\Delta = 3.34°$

Case GG $\Delta = 4.29°$

Interestingly, for the same geometry and mass the GG case has an higher additional inclination due to mass compared to the FG case. However Δ is not defining the magnitude of the power losses: a reformulation of the unified model is necessary to take into account this additional angle.

Case	Name	Value	Units	Description
	θ	20	$^\circ$	Inclination of the tether at the kite connection
	G_e	10	-	Glide ratio
	C_d	0.15	-	System drag coefficient
	A	100	m^2	Kite area
	m	2000	kg	System mass
	ρ_{air}	1.225	kg/m^3	Air density
	V_w	10	m/s	Wind speed
GG	γ_t	0	-	
	γ_{out}	0.33	-	
FG	γ_t	0.5	-	
	γ_{out}	0	-	

Table 3.1: Parameters for the evaluation of the additional inclination Δ for the GG and FG example.

3.7 Unified model including mass losses

3.7.1 Derivation

In this section a modification of the power production model to take into account the influence of the mass is presented. The derivation is similar to the one presented in Section 3.3, thus only the main equations are shown. Referring to Figure 3.14 the wind velocity seen form the kite is now reduced by a factor $\cos(\theta + \Delta)$: $V_{w\|} = V_w \cos(\theta + \Delta)$.

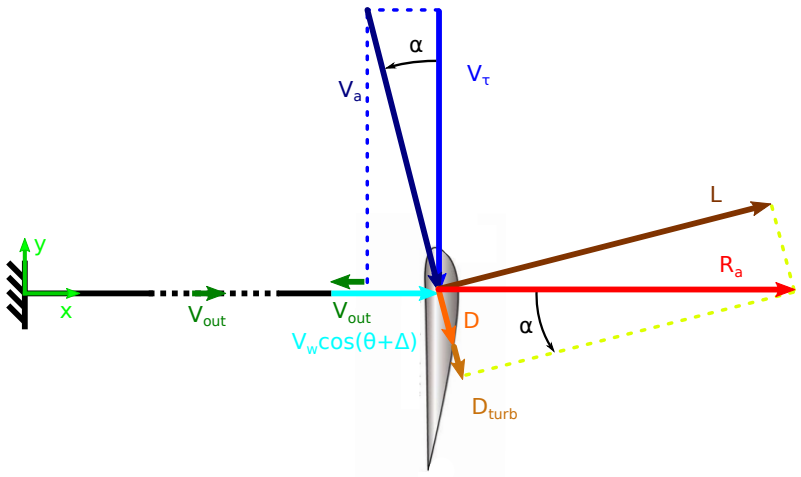

Figure 3.14: Velocity triangle and aerodynamic forces seen from the top for a generic crosswind AWES, including the mass effects.

Defining $\gamma_{out} = \frac{V_{out}}{V_w}$ and $\gamma_t = \frac{C_{d,turb}}{C_d}$, the relative velocity is:

$$\boxed{V_a^2 = V_w^2 \left(\frac{\cos(\theta + \Delta) - \gamma_{out}}{1 + \gamma_t}\right)^2 \left((1 + \gamma_t)^2 + Ge^2\right)} \tag{3.82}$$

A general expression for the aerodynamic force R_a can be found:

$$R_a = \frac{1}{2}\rho_{air}\, A\, C_d\, V_w^2 \left(\frac{\cos(\theta + \Delta) - \gamma_{out}}{1 + \gamma_t}\right)^2 \left((1 + \gamma_t)^2 + Ge^2\right)^{3/2} \tag{3.83}$$

Considering that $T = Ra\,(1 - \Delta - \Delta\tan(\theta))$ (eq. (3.76)), the tether force can be expressed as:

$$\boxed{T = \frac{1}{2}\rho_{air}\ A\ V_w^2\ C_d\ \left(\frac{\cos(\theta+\Delta) - \gamma_{out}}{1+\gamma_t}\right)^2 \left((1+\gamma_t)^2 + Ge^2\right)^{3/2}\ (1 - \Delta - \Delta\tan(\theta))} \tag{3.84}$$

The drag force due to the turbines $D_{turb} = \frac{1}{2}\rho_{air}\ A\ \gamma_t C_d\ V_a^2$ can be expressed as:

$$\boxed{D_{turb} = \frac{1}{2}\rho_{air}\ A\ \gamma_t\ C_d\ V_w^2\ \left(\frac{\cos(\theta+\Delta) - \gamma_{out}}{1+\gamma_t}\right)^2 \left((1+\gamma_t)^2 + Ge^2\right)} \tag{3.85}$$

Defining $\eta_\Delta = (1 - \Delta - \Delta\tan(\theta))$ and $\phi = \theta + \Delta$, the power ground generated P_{gr} can be expressed as:

$$P_{gr} = \left[\frac{1}{2}\rho_{air}\ A\ V_w^2\ C_d\ \left(\frac{\cos\phi - \gamma_{out}}{1+\gamma_t}\right)^2 \left((1+\gamma_t)^2 + Ge^2\right)^{3/2} \eta_\Delta\right] \cdot \left[V_w \gamma_{out}\right]$$

$$\boxed{P_{gr} = \frac{1}{2}\rho_{air}\ A\ V_w^3\ \eta_\Delta\ \gamma_{out}\ C_d\ \left((1+\gamma_t)^2 + Ge^2\right)^{3/2} \left(\frac{\cos\phi - \gamma_{out}}{1+\gamma_t}\right)^2} \tag{3.86}$$

The power onboard generated P_{ob} can be expressed as:

$$\begin{aligned} P_{ob} = &\left[\frac{1}{2}\rho_{air}\ A\ \gamma_t\ C_d\ V_w^2\ \left(\frac{\cos\phi - \gamma_{out}}{1+\gamma_t}\right)^2 \left((1+\gamma_t)^2 + Ge^2\right)\right] \cdot \\ &\left[V_w\ \left(\frac{\cos\phi - \gamma_{out}}{1+\gamma_t}\right) \sqrt{(1+\gamma_t)^2 + Ge^2}\right] \end{aligned}$$

$$\boxed{P_{ob} = \frac{1}{2}\rho_{air}\ A\ V_w^3\ \gamma_t\ C_d\ \left((1+\gamma_t)^2 + Ge^2\right)^{3/2}\ \left(\frac{\cos\phi - \gamma_{out}}{1+\gamma_t}\right)^3} \tag{3.87}$$

The total power generated is the summation of P_{gr} and P_{ob}:

$$\begin{aligned} P_{out} = &\frac{1}{2}\rho_{air}\ A\ C_d\ V_w^3\ \left((1+\gamma_t)^2 + Ge^2\right)^{3/2} \cdot \left[\gamma_{out}\eta_\Delta \left(\frac{\cos\phi - \gamma_{out}}{1+\gamma_t}\right)^2 + \right. \\ &\left. + \gamma_t \left(\frac{\cos\phi - \gamma_{out}}{1+\gamma_t}\right)^3\right] \end{aligned} \tag{3.88}$$

The reel-in phase and the relative efficiency η_{in} model the whole cycle. The efficiency of the reel-out phase η_{out} (Section 3.1.6) takes into account the power losses due to the trajectory and to the ground power conversion. The induction factor a (Eq. (3.70)) models the disc theory losses of the on board wind turbines. Finally, the efficiency γ_t includes generation and transmission power losses of the on board power generation. Therefore, the mean power equation is:

$$\boxed{\begin{aligned} P_{cycle} = &\frac{1}{2}\rho_{air}\ V_w^3\ A\ \left[C_d\ \left((1+\gamma_t)^2 + Ge^2\right)^{3/2} \cdot \right. \\ &\left(\eta_{out}\eta_\Delta \left(\frac{\cos\phi - \gamma_{out}}{1+\gamma_t}\right)^2 + \frac{\eta_t\ (1-a)\ \gamma_t}{\gamma_{out}} \left(\frac{\cos\phi - \gamma_{out}}{1+\gamma_t}\right)^3\right) + \\ &\left. - \frac{C_{d0}}{\eta_{in}} \left(1 + \gamma_{in}^2 + 2\gamma_{in}\cos\beta\right)\right] \cdot \frac{\gamma_{in}\gamma_{out}}{\gamma_{in} + \gamma_{out}} \end{aligned}} \tag{3.89}$$

3.7.2 Example

Referring to the data in Table 3.1, the two cases are considered to analyse the power losses.

For the GG-AWES case, the angle Δ is found to be 4.29°. Thus the term $\eta_\Delta = (1 - \Delta - \Delta\tan(\theta)) = 0.90$. The power for this case, not including power losses due to mass, is found to be: $P_{GG} = 1.14$ MW. Considering the power losses, the power is computed with eq. (3.86) to be: $P_{GG} = 0.93$ MW. The power is therefore reduced by 18 %, if the mass losses are included.

Considering the FG-AWES case, the angle Δ is 3.34°. The power not including losses is $P_{FG} = 1.16$ MW. Including the losses: $P_{FG} = 1.09$ MW. Thus, the power is reduced by 7 %.

This example is showing that for the same geometry and mass a FG-AWES has less power losses due to mass. However, it should be remarked that often a FG-AWES is heavier than a GG-AWES, because of the presence of the on-board turbines. Thus, this should be considered when the systems are compared.

3.8 Atmospheric model

In this work, the atmospheric model proposed by Arecher [5] [6] is used. As both air density and wind speed vary with the altitude, both components are considered. The air density is described by:

$$\rho(z) = \rho_0 e^{-\frac{z}{H_p}} \tag{3.90}$$

with $\rho_0 = 1.225$ kg/m^3 and $H_p = 8550$ m [23]. The wind speed at altitude z is instead computed through a friction coefficient α:

$$v_w(z) = v_w(z_{ref}) \left(\frac{z}{z_{ref}}\right)^\alpha \tag{3.91}$$

It is assumed that above 500 m the wind speed remains constant, as the boundary layer effects terminate [6]. A list of friction coefficients, with the relative terrain type, is presented in Table 3.2.

Terrain characteristics	**Friction coefficient** α
Smooth hard ground, calm water	0.10
Tall grass on level ground	0.15
High crops, hedges and shrubs	0.20
Wooded countryside, many trees	0.25
Small town with trees and shrubs	0.30
Large city with tall buildings	0.40

Table 3.2: Friction coefficient a for various terrain types [6].

In Figure 3.15a, the typical trends of the atmospheric quantities are displayed. With this wind model, the maximum power is set to 500 m. Bechtle [7] shows that, depending on the time of the day, the maximum power can be found also at lower altitudes. Thus, the kite should be able to adjust the operational altitude to harvest the maximum power.

The location is characterized also by a wind distribution, often described with a Weilbull probabilistic function [33]:

$$f(v_w) = \frac{k}{A}\left(\frac{v_w}{A}\right)^{k-1} \exp\left(-\left(\frac{v_w}{A}\right)^{k}\right) \tag{3.92}$$

where $f(v_w)$ represents the frequency for each wind speed at the reference altitude, k the form Weibull parameter and A the scale parameter [33].

In this work, the nominal values are a reference height of 20 m with a wind shear of $\alpha = 0.2$, a form Weibull parameter k= 2.12 and a scale parameter A =9.5 m/s [2]. The Weibull probabilistic function for these values is shown in Figure 3.15b.

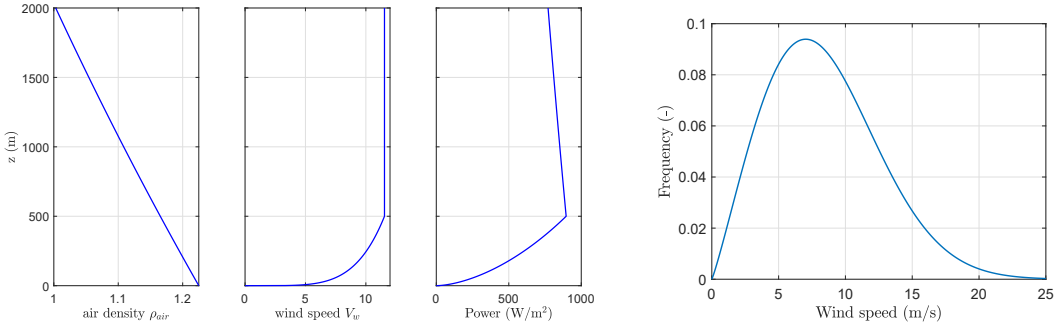

(a) (b)

Figure 3.15: Typical profiles of air density (Eq. (3.90)), wind speed (Eq. (3.91)) and Power density (a). Nominal Weibull probability density function considered in this work (b).

3.9 Model limitations

The main limitations of the physical model are due to the necessity of have simple analytic models.

The steady state flight assumption leads to neglect the trajectory and thus the relative losses. The effects of the tether sag in the direction of the kite velocity (sag due to aerodynamic forces) is also neglected. These losses are included in the present model as efficiencies, instead of being function of the trajectory.

The reel-in model is also approximative if compared to reality. It indeed neglects the transition phase between retraction and generation phases.

The structural model does not include the design of shear panels, shear webs, fuselages and tail. Moreover, no constraint on the bucking is included. However, the main physic is modelled.

The take-off model describes approximative the climbing phase. However, the main physic is considered.

3.10 Model development history

The model has been developed in an iterative way, the development steps are:

1. Derivation of the unified model for high glide ratios.

[2] These values represent the Weibull distribution in Beldringe, Denmark [34]

2. Introduction of a structural model, considering a uniform distributed load.
3. Derivation of the function for the additional inclination angle Δ due to mass.
4. Derivation of the unified model for high glide ratios including the mass losses.
5. Introduction of the take-off model.
6. Refinement of the structural model, after a global analysis highlighted an high importance of the mass. Introduction of the elliptical load distribution.
7. Removal of the high glide ratio assumption from all the derivations. This hypothesis is not always met.

3.11 Summary & Contributions

In this chapter, the physical model of a generic crosswind AWES is presented. Initially, two refined models for the power production of FG-AWES and GG-AWES are shown with the assumption of steady state flight.

In Section 3.3, the power equation for a generic crosswind AWES is derived by the author, with the assumption of steady state flight.

In Section 3.4 a structural model, performed with Euler–Bernoulli beam theory, is presented. Section 3.5 presents a take-off model. The on-board wind turbines area is modelled using disc theory. The structural and take-off models aim to estimate the flying mass.

The additional kite inclination due to the flying mass can be found with the derivations, performed by the author, presented in Section 3.6.

Finally, in Section 3.7, a refinement of the unified power equation to include the power losses due to mass is derived by the author. This derivation can be useful to crosswind AWES designers, providing an analytic formulation to estimate the power losses due to mass. This formulation does not use the assumption of high glide ratios. To the best knowledge of the author, no literature sources are showing these equations.

Chapter 4

Design evaluation methods

In this chapter, the methods used to evaluate the model proposed in the previous chapter are described and explained. Given the complexity of the system, some advanced analysis techniques are needed to help the understanding of the model.

In this chapter, one example is presented in order to make the methods clear to the reader and make easier the understanding of the results. The example concerns the design of a rectangular cantilever beam with a distributed load. The design is subject to structural constraints.

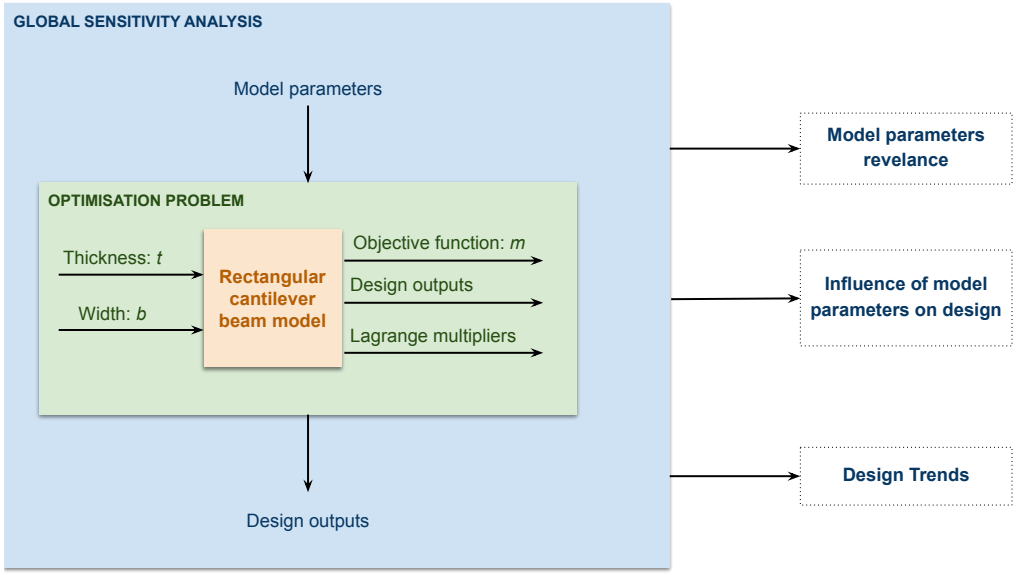

Figure 4.1: Design evaluation framework for the cantilever beam example.

Referring to Figure 4.1, the design of the cantilever beam is performed by means of an optimisation algorithm. The optimisation is meant to model the design process. In Section 4.1, the methods to solve an optimisation problem are presented.

The design process is influenced by some model parameters that are fixed within an optimisation problem. For instance, two model parameters for the cantilever beam example can be the the Young modulus and the strength of the material. Given the model parameters, the design process, performed by the optimiser, is fully deterministic. The design is characterised by the objective function, which is the function the optimiser minimises, by design outputs, which describe the solution, and by Lagrange multipliers, which are properties of the optimal solution. Once the optimisation is performed, the

design can be analysed with a local sensitivity analysis. In this way, an investigation on the sensitivity of the design with respect to the model parameters can be carried out. In Section 4.2 the methods to analyse the optimum design are shown.

The optimisation problem is a design process that for some given model parameters is performing the design. Some model parameters have high uncertainty. A local sensitivity analysis cannot capture the non-linearity of the model, thus a global approach is proposed. The uncertainties of the model parameters are initially to be evaluated. Later, a global sensitivity analysis can assess how these uncertainties propagate throughout the design process. The aim of the global sensitivity analysis is to give a complete picture of the design, considering the uncertainties. In Section 4.3, the methods to perform a global sensitivity analysis are shown.

4.1 Optimisation

4.1.1 Problem formulation

To understand the methods to solve an optimisation problem, the example is introduced here. A rectangular cantilever beam has to withstand a distributed load, not exceeding the maximum stress level σ_{lim} at the root and a maximum deflection δ_{max} at the tip. Moreover, the beam cannot be designed with an aspect ratio higher that a fixed value, for manufacturing reasons. With these three constraints, the mass of the beam should be minimized.

The generalized problem can be expressed as:

$$\begin{aligned} \underset{\boldsymbol{x}}{\text{minimize}} \quad & f(\boldsymbol{x}) \\ \text{subject to} \quad & l \leq \boldsymbol{x} \leq \boldsymbol{u} \\ & \boldsymbol{g}(\boldsymbol{x}) \leq 0 \\ & \boldsymbol{h}(\boldsymbol{x}) = 0 \end{aligned} \tag{4.1}$$

Where f is the objective function, $\boldsymbol{l}$ and $\boldsymbol{u}$ are the lower and upper bounds of the design variables, $\boldsymbol{g}$ represents the inequality constraints and $\boldsymbol{h}$ are the equality constraints.

Letting b to be the width and t the thickness of the cross-section of the cantilever beam, the problem ,in this case, can be expressed as:

$$\begin{aligned} \underset{\boldsymbol{q}}{\text{minimize}} \quad & m = \rho \cdot q_b \cdot q_t \cdot L \\ \text{subject to} \quad & t_{min} \leq q_t \leq t^{max} \qquad b_{min} \leq q_b \leq b^{max} \\ & \delta_{tip} = \frac{wL^4}{8EI} \leq \delta_{max} \\ & \sigma_{root} = \frac{wL^2 t}{4} \leq \sigma_{lim} \\ & \frac{t}{b} \leq AR_{lim} \qquad \frac{b}{t} \leq AR_{lim} \end{aligned} \tag{4.2}$$

Where q indicates the design variables, ρ the material density, w the distributed load, L the length of the beam, E the Young Modulus and I the inertia:

$$I = \frac{1}{12} q_b q_t^3 \tag{4.3}$$

Taking the numerical values of the parameters given in Table 4.1, the optimisation problem can be solved by an optimisation algorithm.

Name	Value	Units	Description
t_{min}	0	m	Minimum beam thickness
t^{max}	1	m	Maximum beam thickness
b_{min}	0	m	Minimum beam width
b^{max}	1	m	Maximum beam width
w	100	kN/m	Distributed load
L	10	m	Beam length
ρ	1600	kg/m^3	Material density
E	70	GPa	Young Modulus
σ_{lim}	570	MPa	Stress limit
δ_{max}	0.2	m	Maximum deflection
AR_{lim}	3	-	Maximum aspect ratio

Table 4.1: Numerical values of the model parameters used in the example.

4.1.2 Optimisation algorithm

In this section, the optimisation algorithm used in this work is introduced. Since the nature of the model, presented in the previous chapter, is continuous, a gradient-based algorithm is suitable for the problem.

Gradient-based algorithms are first order iterative algorithms that find minima of a given objective function.

One of the most effective methods for non-linearly constrained optimisation generates steps by solving quadratic sub-problems [35]. Sequential Quadratic Programming (*SQP*), used in this work, solves a sequence of optimisation sub-problems. Each sub-problem optimises a quadratic model of the objective, subject to a linearisation of the constraints [35].

SQP methods are well-known to be efficient, robust and accurate for continuous optimisation problems of the sizes considered in this thesis.

Coming back to the example of the cantilever beam, Figure 4.2 shows a contour plot of the objective function. The lines represent the constraints and the dot the optimum solution, found with the usage of a *SQP* method. In this thesis, the MATLAB function *fmincon* [36] is used.

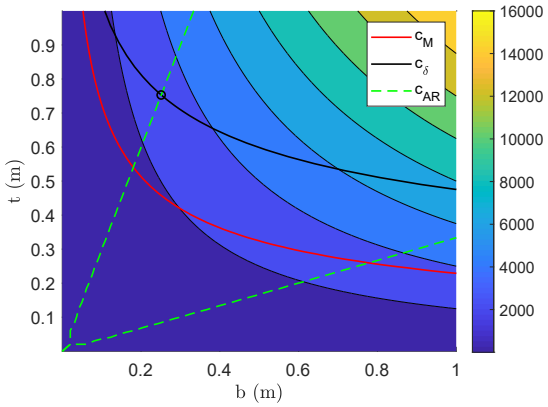

Figure 4.2: Mass as function of the two design variables. The red line represents the limit of the stress constraint, the black of the tip displacement and the green the aspect ratio. The optimum mass, defined by a circle ∘, is 3023 kg.

4.2 Design sensitivity analysis

Once the design is evaluated with the optimisation algorithm, a local sensitivity analysis can help the understanding of the optimum solution. Thus, a local sensitivity analysis can be carried out in two ways. The first (Post-optimal sensitivity analysis) is to analyse the Lagrange multipliers of the solution, to understand how the constraints influence the objective function. The second is to compute the gradients of some outputs with respect to some inputs in order to study the sensitivity.

4.2.1 Post-optimal sensitivity analysis

The solution, as shown in Figure 4.2, is determined by the constraint on the deflection and by the constraint on the aspect ratio. Since these limits are arbitrary determined, the variation of the mass according to a small change of the constraint limit should be analysed. A simple way to do this is to look at the Lagrange multipliers of the solution.

The KKT conditions [35] must be satisfied for a locally optimal solution:

$$\begin{gathered} \nabla f + \nabla \boldsymbol{g} \boldsymbol{\lambda}_i + \nabla \boldsymbol{h} \boldsymbol{\lambda}_e = \mathbf{0} \\ \boldsymbol{g}(\mathbf{0}) \leq \mathbf{0} \\ \boldsymbol{g}(\mathbf{0}) \boldsymbol{\lambda}_i = \mathbf{0} \\ \boldsymbol{\lambda}_i \geq \mathbf{0} \end{gathered} \tag{4.4}$$

Where $\boldsymbol{\lambda}_i$ and $\boldsymbol{\lambda}_e$ are the Lagrange multipliers on the inequality and equality constraints respectively. The meaning of the Lagrange multiplier $\boldsymbol{\lambda}$ is explained with the help of the example. The first KKT condition (eq. (4.4)), called *stationary condition*, for the two dimensional example of the cantilever beam, can be written as:

$$\begin{bmatrix} \frac{\partial m}{\partial b} \\ \frac{\partial m}{\partial t} \end{bmatrix} + \begin{bmatrix} \lambda_b^{upper} \\ \lambda_t^{upper} \end{bmatrix} + \begin{bmatrix} \lambda_b^{lower} \\ \lambda_t^{lower} \end{bmatrix} + \begin{bmatrix} \frac{\partial c_M}{\partial b} & \frac{\partial c_\delta}{\partial b} & \frac{\partial c_{AR}^{(1)}}{\partial b} & \frac{\partial c_{AR}^{(2)}}{\partial b} \\ \frac{\partial c_M}{\partial t} & \frac{\partial c_\delta}{\partial t} & \frac{\partial c_{AR}^{(1)}}{\partial t} & \frac{\partial c_{AR}^{(2)}}{\partial t} \end{bmatrix} \begin{bmatrix} \lambda_{CM} \\ \lambda_{C\delta} \\ \lambda_{CAR}^{(1)} \\ \lambda_{CAR}^{(2)} \end{bmatrix} = \begin{bmatrix} 0 \\ 0 \end{bmatrix} \tag{4.5}$$

Considering the numerical values given in Table 4.1, only $\lambda_{C\delta}$ and $\lambda_{CAR}^{(1)}$ are different from zero, highlighting the fact that these two constraints are active:

$$\begin{bmatrix} \frac{\partial m}{\partial b} \\ \frac{\partial m}{\partial t} \end{bmatrix} = \begin{bmatrix} \frac{\partial c_\delta}{\partial b} & \frac{\partial c_{AR}^{(1)}}{\partial b} \\ \frac{\partial c_\delta}{\partial t} & \frac{\partial c_{AR}^{(1)}}{\partial t} \end{bmatrix} \begin{bmatrix} \lambda_{C\delta} \\ \lambda_{CAR}^{(1)} \end{bmatrix} \tag{4.6}$$

The Lagrange multipliers give an estimation of how much the objective function changes with a change of the constraint limit, or in other words how strongly the constraint is limiting the solution. The Lagrange multiplier of the tip deflection is:

$$\lambda_{C\delta} = 7550 \ \frac{\text{kg}}{\text{m}} \approx \frac{\partial m}{\partial c_\delta} \tag{4.7}$$

If the designer changes the maximum allowed displacement of 0.01 m, the gain in mass is:

$$\lambda_{C\delta} \cdot 0.01 = 75.5 \text{ kg} \tag{4.8}$$

If the optimisation problem is solved with a new maximum displacement of 0.21 m (0.01 m of difference), the saved mass is $\Delta m = 73$ kg, similar to the one predicted by the Lagrange multipliers. In Figure 4.3, a zoom on the reference solution with $\delta_{max} = 0.2$ m and on the new solution with $\delta_{max} = 0.21$ m is shown, outlining a decrease of about 75 kg.

If the same procedure is applied to a change in the maximum displacement of 0.1 m (i.e. maximum displacement of 0.3 m), the Lagrange multiplier predicts a mass change of 755 kg, while the optimum found by solving a new optimisation problem has a saved mass of 554 kg. This highlights the fact that this sensitivity analysis works only locally.

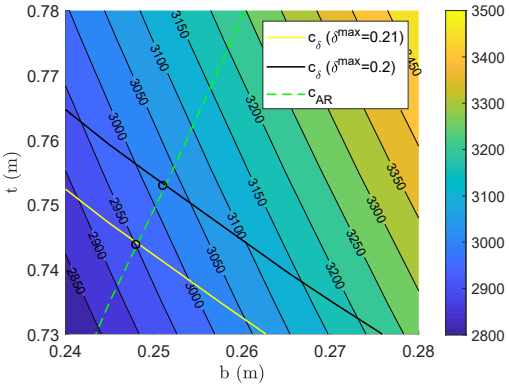

Figure 4.3: Contour plot of the mass showing the two optimum solutions with $\delta_{max} = 0.2$ m and $\delta_{max} = 0.21$ m.

Another interpretation of the Lagrange multiplier is related to the strength of the constraint. If a Lagrange multiplier is high, it means that it is strongly constraining the solution, preventing the objective function to decrease of a high quantity. On the other hand, if a Lagrange multiplier is low, the constraint is weak and the objective function would decrease of a small quantity with a change of the limit. If a Lagrange multiplier for the inequality constraint is zero, the relative constraint is not active. A strong constraint is therefore driving the design, while a weak one can often be neglected in the analyses.

When Lagrange multipliers are compared, one should consider the units of the constraints. Therefore, in this thesis, the Lagrange multipliers are normalized with the constraint limit value. They show how the objective function changes with a relative change of the constraint limit. In this way, different Lagrange multipliers with different units can be compared.

4.2.2 Sensitivity analysis with gradients

The classical way of doing sensitivity analysis is to look at the partial derivative of the outputs with respect to the inputs.

Thus, some interesting outputs describing the design should be selected. For the cantilever beam example, the mass m, which is the objective function of the optimisation problem, and the two beam dimensions b and t, the design variables, are considered.

To understand how the design varies locally with some model parameters, one can take the gradients of the outputs with respect to them. Thus, a study on how the maximum aspect ratio AR_{lim}, the maximum tip deflection δ_{max}, the Young modulus E and the material strength σ_{lim} are influencing the outputs is carried out by taking the gradients.

To do this, the selected model parameters are varied of a small increment and the optimisation is run with the new set of model parameters. The gradients can be attained numerically.

In Table 4.2, the gradients evaluated in the reference point (Table 4.1) of three considered design outputs with respect to the four inputs (model parameters) is shown. The gradients have been normalised with the nominal value to make a comparison possible. Thus they show how a non-dimensional change of the model parameter X_i impacts the output.

$\mathbf{X}$	AR_{lim}	δ_{max}	E	σ_{lim}
$\frac{\partial m}{\partial X_i}$	-1542	-1000	-902	0
$\frac{\partial b}{\partial X_i}$	-0.19	-0.03	-0.02	0
$\frac{\partial t}{\partial X_i}$	0.20	-0.21	-0.22	0

Table 4.2: Gradient of mass m in kg/-, width b and thickness t in m/- with respect to the model parameters $\mathbf{X}$.

The mass m is strongly influenced by the aspect ratio AR_{lim}, by the maximum tip deflection δ_{max} and the Young modulus E. The mass is not sensitive to the material strength σ_{lim} because the relative constraint is not active. Thus, a change in the limit is not influencing the result. Similar conclusions can be drawn for the width and the thickness.

This way of performing sensitivity analysis is a point evaluation. It could be interesting to understand how the outputs vary with a big variation of the inputs. A way to study the model sensitivity, considering the model parameter ranges, would be to look at the gradients in many points. An other is to perform a variance based sensitivity. The basic idea of this method is to understand how much of the outputs variance is due to the inputs variance.

4.3 Global sensitivity analysis

In many engineering models, the model parameters are subject to high uncertainties and a local sensitivity analysis would not capture the non-linearities of the model. Thus, a global sensitivity analysis, where the model parameters can vary within all the ranges, would be more informative.

A graphical representation of the framework to carry a global sensitivity analysis is presented in Figure 4.4.

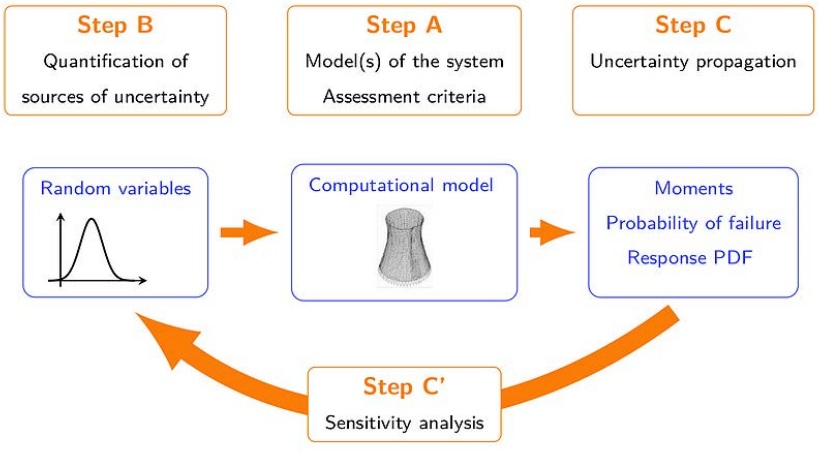

Figure 4.4: The general uncertainty quantification framework [37].

Step A in this work represents the optimisation problem itself. Looking at other engineering problems related to kites, the computational model could be a dynamic model, a *CFD* of the wings, a *FE* structural analysis, an electrical design and so on. The computational model is seen from the global sensitivity framework as a black box, with inputs (model

parameters) and outputs (design outputs).

Step B refers to the understanding of the uncertainties: the sources of uncertainty should be identified and quantified.

Once *Step A and B* are completed, the uncertainty in the outputs can be evaluated, and by relating this to the sources of uncertainty, the sensitivity analysis can be completed (*Step C*).

Some quantitative examples are given later in this section. To perform the global sensitivity analysis, the MATLAB toolbox *UQLab* [38] is used.

4.3.1 Uncertainty Quantification

Every model engineers are dealing with is influenced by the numerical values of the model parameters. Often these parameters are subject to uncertainty, or even unknown. Thus, when dealing with models, particular attention should be given to the estimation of these parameters and to the understanding of which are more relevant for the final result. The estimation of the parameters uncertainty comes first, later a global sensitivity analysis can establish the most critical parameters.

The uncertainty quantification, during the modelling phase, can also be a decision tool to understand when it is necessary to develop a more sophisticated model or when an approximate one is enough. For example, in the design of kites, the designer does not know *a priori* if the mass is relevant for the power output, thus a simple structural model with a high uncertainty is sufficient at the beginning. If the mass uncertainty has a strong influence on the results, then a more accurate model is justified. Therefore, high uncertainty on some parameters can be representative of many possible modelling strategies.

The uncertainty quantification can also be useful during the design phase. The performance of an undeveloped component can be modelled as a source of uncertainty. If a subsystem is not relevant for the final output, there is no need of spending time and money on the detailed design and optimisation of that specific subsystem.

Another application of the uncertainty quantification is to model the technological development of a component. For example, talking about kites, an uncertainty on the tether strength can represent the technological development of the component. By studying how this uncertainty propagate throughout the model, one can understand the benefit of a technological improvement.

Coming back to the design of the cantilever beam, the uncertainties of the model parameters are given in Table 4.3. If the model parameter is a material property, a Gaussian distribution can be assigned (aleatory uncertainty). If the parameter represents a design limit, then a uniform distribution may be a good choice (epistemic uncertainty). In other words, parameters with epistemic uncertainties are sources of uncertainty because they are unknown at a first design stage, but in the future they will be fixed. For example, the maximum tip deflection of the beam during the first analysis is unknown. In the future, the designer, with the help of the considerations given by the sensitivity analysis, will fix this value.

The aim of the global sensitivity analysis is to understand how these uncertainties influence the design.

Name	Min	Max	Units	Distribution
AR_{lim}	1.5	4.5	m	Uniform
δ_{max}	0.05	0.35	m	Uniform
Name	Mean	Std	Units	Distribution
E	70	5	GPa	Gaussian
σ_{lim}	570	57	MPa	Gaussian

Table 4.3: Uncertainly of the model parameters for the cantilever beam example.

4.3.2 Statistics of the evaluations over the model parameter space

Once the uncertainties are defined, the design can be evaluated in many points of the model parameter space. Considering the example, one could sample many points based on the uncertainties given in Table 4.3. Then, the design can be evaluated for each point.

The first analysis is to look at mean and variance of the outputs of these evaluations. The mean of the optimal outputs is the expected optimal design configuration, this can also be considered the centre of the design space. The variance of the outputs is showing which outputs are more or less sensitive to uncertainty.

Considering the cantilever beam example, multiple outputs of the optimisation problem can be considered for the uncertainty propagation:

m**:** This is the objective function for the optimisation problem.

b**:** The beam width of the optimum solution. For the optimisation problem it is a design variable, but it can be seen as an optimisation output.

t**:** The beam thickness of the optimum solution. For the optimisation problem it is a design variable, but it can be seen as an optimisation output.

λ_δ**:** The Lagrange multiplier of the deflection constraint. This is a property of the optimum solution, but it can be seen as an optimisation output.

λ_{AR}**:** The Lagrange multiplier of the aspect ratio constraint. This is a property of the optimum solution, but it can be seen as an optimisation output.

λ_σ**:** The Lagrange multiplier of the strength constraint. This is a property of the optimum solution, but it can be seen as an optimisation output.

Multiple outputs help the understanding of the design. In Table 4.4 the mean and the standard deviation of the selected outputs are shown.

	m	b	t	λ_δ	λ_{AR}	λ_σ
units	kg	m	m	kg/-	kg/-	kg/-
mean	3557.2	0.26	0.86	1973.8	1583.4	0
std	772.9	0.06	0.09	849	610.2	0

Table 4.4: Means and standard deviations of the evaluation outputs for the cantilever beam example.

The mass m, width b and thickness t represent the most likely design, while the average Lagrange multipliers give information on how strong the constraints are. Lagrange multipliers are normalized with the constraint limit. Thus a change of 1 % of the maximum deflection would, on average, change the mass of $\lambda_s \cdot 0.01 = 20$ kg. Comparing the three Lagrange

multipliers, it turns out that the constraint on the tip displacement is, on average, stronger. The statistics of Lagrange multiplier of the strength constraint outline that this constraint is never active.

Generally speaking, by looking at the standard deviation, it is possible to understand if the outputs are sensitive to uncertainty or not. If a parameter has low standard deviation, then it is not sensitive to the inputs uncertainties and it can be fixed to the mean value. On the opposite, if a certain output has high variance, then this output deserves extra studies to understand it. Similar considerations can be done for Lagrange multipliers. If a Lagrange multiplier has low mean and low variance, then the respective constraint is rarely design driving and it can most of the times be ignored. If a Lagrange multiplier has high mean and low variance, then this constraint is always active and it should be included in all the studies. If a Lagrange multiplier has high mean and high variance it means that some aspects in the design influence the constraint. In other words, this constraint can be really important in some cases, but in others not.

4.3.3 Average gradients over the model parameter space

It can be interesting to investigate how the sensitivity varies in the model parameter space. One could evaluate the gradient in many points, according to the model parameters uncertainties. Then, the mean and the standard deviation of the absolute value of the gradients can be found. The mean represents the average sensitivity of one output with respect to a model parameter. The standard deviation gives an indication on how the sensitivity varies in the model parameter space.

In Table 4.5 the mean and the standard deviation of the absolute values of the gradients of mass and beam dimensions with respect to the model parameters are given.

	$\mathbf{X}$	AR_{lim}	δ_{max}	E	σ_{lim}
mean	$\frac{\partial m}{\partial X_i}$	1609	2110	2140	0
std		525	1088	1556	0
mean	$\frac{\partial b}{\partial X_i}$	0.198	0.099	0.105	0
std		0.062	0.069	0.106	0
mean	$\frac{\partial t}{\partial X_i}$	0.18	0.175	0.171	0
std		0.025	0.042	0.058	0

Table 4.5: Average and standard deviation of the absolute value of the gradient of mass m in kg/-, width b and thickness t in m/- with respect to the model parameters $\mathbf{X}$.

The mass has, on average, a high sensitivity to the Young modulus E. Second, it is sensitive to the maximum tip displacement and to the maximum aspect ratio. The mass is not sensitive to the material strength. The constrain on the material strength is indeed never active, as shown in the previous section. Thus, the design is not modified by a change in the constraint limit itself.

The gradient of the mass with respect to the Young modulus has high standard deviation compared to the mean value. This outlines that in some cases the mass is highly sensitive to E, in other it is less.

However, to carry out this analysis, many evaluations of the design are to be performed. With an increase of the model parameter space dimension and of the computational time for the design process (the optimisation), this approach is too computational demanding. Thus, the methods explained in the next two sections are used in this work.

4.3.4 Uncertainty propagation & surrogate models

Referring to Figure 4.4, many techniques are available for uncertainty propagation. The most famous is Monte Carlo Simulation [39], where the input variables are sampled based on random numbers simulations. Unfortunately, this method requires a high number of evaluations and can be carried out only when the model is not too computational demanding

Other more efficient methods, based on surrogate models, are nowadays studied, making possible a small number of evaluations (typically 2-3 order of magnitude less than Monte Carlo [37]). A surrogate model, or metamodel, is a function that emulates the real model with a negligible computational cost and can be produced by a number of evaluations.

The first step for the creation of a metamodel is the sampling. It is done with different techniques. The most common are *Latin hypercube sampling* for its attractive space filling property and *quasi-random sequences* [37]. Since the evaluation points are not related to each other, the computations can be performed in parallel. Once the model is evaluated in various points, a functional shape of the metamodel has to be chosen. Some common shapes are *Polynomial chaos expansions*, *Low-rank tensor approximations*, *Kriging (a.k.a Gaussian processes)* and *Support vector machines*. The one used in this work is *Polynomial chaos expansions*. This metamodel consists in a polynomial approximation of the output made of multivariate orthogonal polynomials [37].

After the sampling, the metamodel can be created and finally, using it, a *variance based sensitivity analysis* carried out. For the creation of the metamodels the MATLAB toolbox *UQLab* [38] is used in this work.

4.3.5 Variance based sensitivity analysis

In this section, the technique used for the interpretation of the sensitivity in the whole model parameter space is introduced, with the help of the cantilever beam example.

The methods used in this work is the variance based sensitivity analysis. The aim of this technique is to quantify how much of the output variance is due to each of the model parameter variance. This information can be really valuable to the designer, by identifying where the greatest focus is. To determine the sensitivity of the model, the Variance Based Decomposition (VBD), is presented.

Considering a random input vector with mutually independent variables $\mathbf{X} = (X_1, \dots, X_d)$, a deterministic model f and the output $Y = f(\mathbf{X})$, the variance of the output can be decomposed as:

$$\mathrm{Var}(Y) = \sum_{i=1}^{d} D_i(Y) + \sum_{i<j}^{d} D_{ij}(Y) + \cdots + D_{12\dots d}(Y) \tag{4.9}$$

where $D_i(Y)$ represents the variance of the expected value of Y, given X_i: $D_i(Y) = \mathrm{Var}\left[\mathbb{E}\left(Y|X_i\right)\right]$, $D_{ij}(Y) = \mathrm{Var}\left[\mathbb{E}\left(Y|X_i, X_j\right)\right] - D_i(Y) - D_j(Y)$ and so on for higher order interactions. The so-called "*Sobol' indices*" or "*variance based sensitivity indices*" [40] are obtained as follows:

$$S_i = \frac{D_i(Y)}{\mathrm{Var}(Y)}, \quad S_{ij} = \frac{D_{ij}(Y)}{\mathrm{Var}(Y)}, \quad \dots \tag{4.10}$$

In this work, the first-order Sobol' indices S_i and the total Sobol' indices are used. The

total are defined as:

$$S_{T_i} = S_i + \sum_{i<j} S_{ij} + \sum_{j\neq i, k\neq i, j<k} S_{ijk} + \ldots = \sum_{l\in \#i} S_l \tag{4.11}$$

The total Sobol' indices give an indication of the contribution of the model parameter X_i to the output Y, including all its interactions with any other model parameter. The first-order Sobol' indices are a measure of the contribution of varying X_i alone to the output variance. In other words, the first-order Sobol' index depicts how much the output variance is influenced by an input, if all the other inputs are fixed. The total Sobol' index outlines how much the output variance is influenced by an input.

To better understand the meaning of these, a variance based decomposition has been carried on the cantilever beam example. Considering the uncertainties listed in Table 4.3, a metamodel has been created thanks to a number of evaluations of the optimisation problem. Using the metamodel, the Sobol' indices are computed. To understand the whole potential of this tool, the six outputs of the optimisation problem considered for the statistical analysis (Section 4.3.2) are considered. Since the Lagrange multiplier on the material strength is always null (Table 4.5), it is not considered in this analysis.

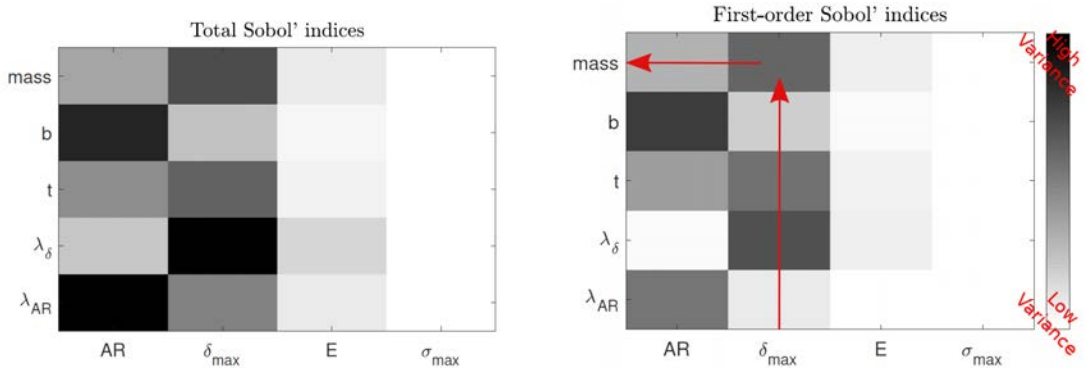

(a) (b)

Figure 4.5: Total and first order Sobol' indices graphical representation. A darker colour highlights a strong influence between the model parameter variance (x-axis) and the output variance (y-axis).

Considering Figure 4.5, it is possible to understand how much of the outputs variance (y-axis) is due to the inputs variance (x-axis). Looking at the Total Sobol' indices, Figure 4.5a, it is clear that the mass variance is strongly influenced by the variance on the deflection limit, secondly by the variance on the aspect ratio. The uncertainties in Young modulus E and material strength σ_{lim} are not influencing the mass compared to the other two model parameters.

This information is slightly different from the one obtained by taking the mean of the absolute value of the gradients (Table 4.5). The mean gradient over the model parameter space indicates how sensitive are, on average, the outputs with respect to the inputs. The Sobol' indices indicate how sensitive are, on average, the outputs variances with respect to the input variances.

For instance, the mass is highly sensitive to the Young modulus, as shown in Table 4.5. Considering the model parameters uncertainties given in Table 4.3, the variance on the Young modulus is influencing less the mass variance compared to the maximum aspect ratio and the maximum tip deflection variance. This is because the *variance based decomposition* takes into account also the distributions and the ranges of the model parameters.

Similar considerations can be done by looking at the other outputs and at the first order Sobol' indices. This information can be used by the designer in many ways. At a modelling level, it can be useful to understand which parameters are driving the design, to spend more efforts on the modelling and design of a critical sub-system. At a system design level, it can be useful to understand where to change the design to have the biggest benefits. Hence, in many engineering applications, this can be a useful decision making tool.

In this thesis, the MATLAB toolbox *UQLab* [38] is used to evaluate the Sobol' indices.

4.3.6 Generic sensitivity analysis

A simple method to explore the model parameter space is to look at the correlations between the outputs and interpret them. In Figure 4.6, the evaluations computed to generate the metamodel are displayed.

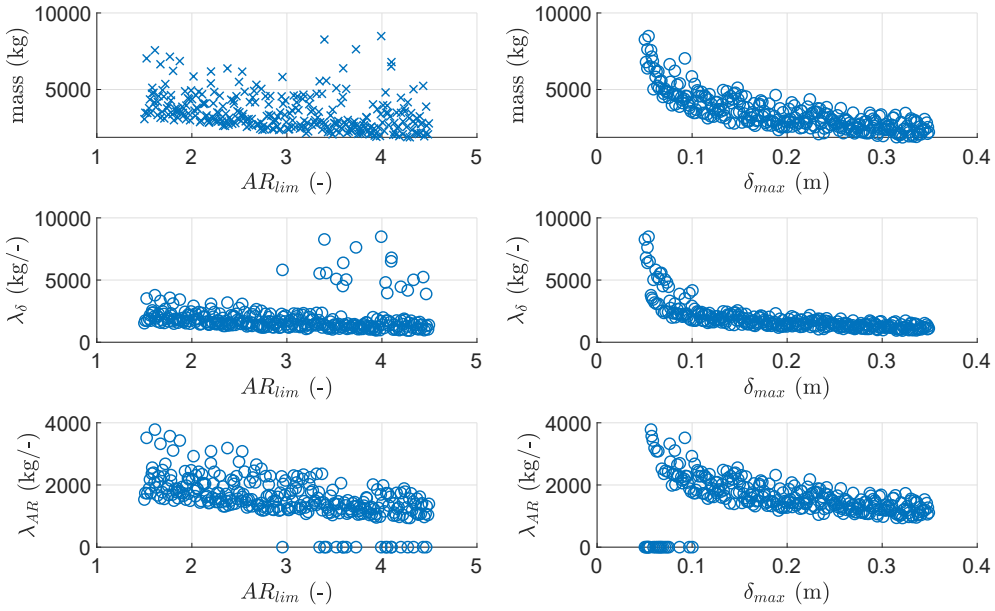

Figure 4.6: Scatter plots of the model evaluations, showing the main trends.

In the top figures, the mass is displayed with the two most relevant model parameters, according to the Sobol analysis. In both cases, the trend is decreasing. In the figures in the second row, the Lagrange multipliers of the displacement constraint are shown. A group of evaluations for high AR and low δ_{max} have significant higher λ_δ, and λ_{AR} equal to zero. This fact shows that, in this region, the aspect ratio constraint is not active and the maximum deflection is driving the design.

If two model parameters turn out to be important for one output, then a surface plot can be a useful visualisation of trends. The metamodel created for the evaluations of the Sobol' indices can be used to visualize the output. Figure 4.7 shows the contour plot of the mass as function of the maximum tip deflection δ_{max} and maximum aspect ratio AR_{lim} When these two values are small, then a high *mass* is found. The trends of the isolines can be a useful indication on how to obtain the same output (mass in this case) with different strategies. It should be remarked that these plots show the average trends of the evaluations.

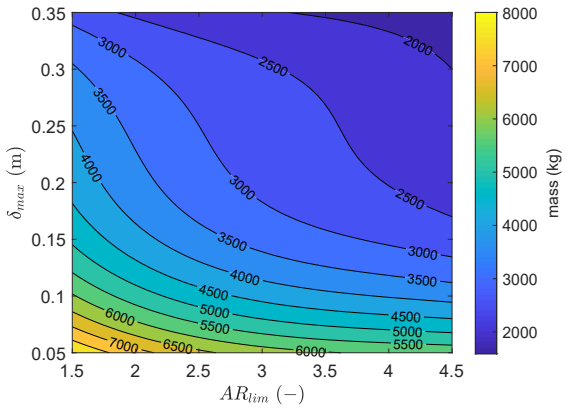

Figure 4.7: Contour plot of metamodel of the mass as function of maximum tip displacement δ_{max} and maximum aspect ratio AR_{lim} .

4.4 Summary

In this chapter, the methods used in this thesis are introduced with the help of one example.

Initially, the optimisation problem formulation is presented. Later, all the methods used to analyse the results are introduced.

The techniques for a local design sensitivity analysis are proposed. It is shown how to interpret Lagrange multipliers and how to carry out a sensitivity analysis with gradients.

In the last part of the chapter, the framework of a global sensitivity analysis is introduced. The sources of uncertainty can be classified as epistemic and aleatory. To evaluate how these uncertainties propagate throughout the model, a variance based decomposition can be performed and the key trends analysed.

Chapter 5

Annual energy production maximisation

In this chapter, the crosswind AWES designs, which maximise the annual energy production given a rated power, are analysed. Initially, the optimisation problem formulation is shown. Some tests aim to validate the code and to benchmark it with some commercial solutions. Later, one example of a typical result is shown. One evaluation can be useful to the reader to get familiar with the results, but it is not very informative because many parameters have high uncertainty. Finally, a global sensitivity analysis is carried out to understand how the chosen model parameters are influencing the design.

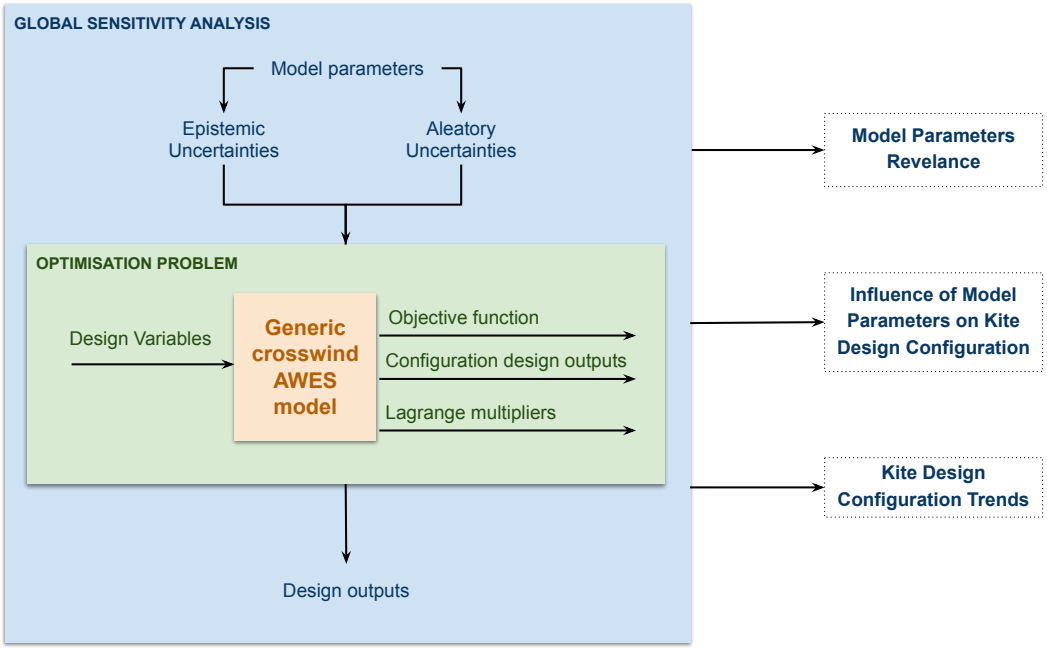

Figure 5.1: Evaluation framework of the generic crosswind AWES model.

In Figure 5.1, the evaluation framework of the model is summarized. The light orange box represents the model introduced in the Chapter 3. An optimisation algorithm can modify the design variables to minimise the objective function. Once the minimum is found, a kite design configuration is also obtained.

The optimisation problem can be seen as an engineering computational model, influenced

by some model parameters. These parameters are uncertain, thus the global sensitivity analysis evaluates how these uncertainties propagate throughout the optimisation problem.

5.1 Problem formulation

The model, as introduced in Chapter 3, is suitable for a gradient based optimisation algorithm: it is indeed continuous. Moreover, the model uses only analytic equations that allow a fast computation of the design. All the parameters describing the physics should be optimised with respect to an objective function, defined accordingly to the stage of the problem. In this chapter, the objective function represents the annual energy production (AEP).

5.1.1 Design Variables

The design variables are given in Table 5.1. Some of them are related to the geometry of the system: span, aspect ratio, tether diameter, tether length. Others are referring to the structural design, such as the thickness of the spar caps and the position of the supports. Most of them are performance parameters, that will drive a more accurate design. These are the elevation and the climbing angle, the velocities of cut-in and out, the percentage of the thrust given by the on-board turbine during the take-off, the lift coefficient and the parameters describing the ground and on-board generation.

DV	Dim	Units	Description
q_s	1x1	m	Kite wing span
q_{AR}	1x1	-	Kite wing aspect ratio
q_d	1x1	m	Tether diameter of the
q_r	1x1	m	Tether length
q_α	1x1	rad	Climbing angle during the take-off
q_β	1x1	rad	Elevation angle
$q_{V_{in}}$	1x1	m/s	Cut-in wind speed
$q_{V_{out}}$	1x1	m/s	Cut-out wind speed
$q_{Q_{turb}}$	1x1	-	Percentage of the thrust given by the on-board turbine during the take-off
q_{t_A}	1x1	m	Spar cap thickness (Fig. 3.10) in Section A (Fig. 3.8)
q_{t_B}	1x1	m	Spar cap thickness (Fig. 3.10) in Section B (Fig. 3.8)
q_{t_C}	1x1	m	Spar cap thickness (Fig. 3.10) in Section C (Fig. 3.8)
q_{x_C}	1x1	m	Position of the support (Fig. 3.9)
$\mathbf{q}_{\gamma_t}$	1xn	-	Coefficient of induced drag from on-board production
$\mathbf{q}_{CL}$	1xn	-	Lift coefficient of the kite
$\mathbf{q}_{\gamma_{out}}$	1xn	-	Reel-out velocity coefficient
$\mathbf{q}_{\gamma_{in}}$	1xn	-	Reel-in velocity coefficient

Table 5.1: Description of the design variables. n represents the number of wind speeds between cut-in and cut-out considered in the design.

5.1.2 Constrains

A few constraints are included in the optimisation: one on the tether strength, one on the rated power, one on the wing area, one on the minimum operational altitude and two related to the structural design.

The tether has two components. A section carries the load and a section transmits power. To design the section of the electric cables, the power generated on-board is estimated.

Considering the on-board maximum power $P_{ob,\,max}$, the section of the electric cables A_{el} is computed with the following equations [3]:

$$I = \frac{V}{P_{ob,\,max}} \qquad R = \frac{P_{loss}}{I^2} \qquad A_{el} = \; 2\frac{r\;\rho_{cu}}{R} \tag{5.1}$$

Where V represents the Voltage, P_{losses} the maximum power that can be lost during the transmission. ρ_{cu} the resistivity of copper and the factor 2 represents the two cables needed for the transmission.

Once the section for the electric cables A_{el}, that is not carrying any load, is computed, the constraint on the tether strength is:

$$\mathbf{T} - \sigma_{lim} \cdot \left(\pi \frac{q_d^2}{4} - A_{el} \right) \leq 0 \tag{5.2}$$

Where $\mathbf{T}$ is a vector with the reel-out tether force (eq. (3.84)) and the reel-in (eq. (3.24)) for each wind speed. σ_{lim} is the tether strength, set to 1.5 GPa.

The constraint of the rated power P_{rated} limits the power to a fixed value. Also the power during the reel-in phase cannot exceed a fixed value.

The constraint of the kite area forces the aspect ratio and the span to give a defined wing area.

A constraint on the minimum operational altitude is added: $h \geq h_{min}$.

Finally, the constraints related to the structural design of the wing are due to the strength of the material and of the displacement (Section 3.4).

5.1.3 Objective function

The objective function is the Annual Energy Production AEP minus the energy spent to take off, with the assumption of one take-off a day. AEP is computed as the integral of the power production curve times the Weibull wind distribution.

5.2 Model implementation

The physical model introduced in Chapter 3 is implemented in MATLAB. The code has to compute the annual energy production, AEP, given the design variables listed in Table 5.1. Figure 5.2 shows the flowchart of the code.

The aerodynamic drag coefficients are computed with Equations (3.15) for each wind speed. The wind speed (Eq. (3.91)) and the air density (Eq. (3.90)) is computed knowing the operational altitude. With an approximation of the on-board power generation, the section for the electric power can be found and the tether sag computed with the model proposed in Section 3.1.4. The structural design is carried out with the model in Section 3.4. The take-off sub-system design follows the procedure shown in Section 3.5. Once the total flying mass is evaluated, the additional angle due to mass can be found with Equation (3.77). Finally, the power curve can be found with Equation (3.89). The AEP is then the integral of the product between the power curve and the Weibull distribution.

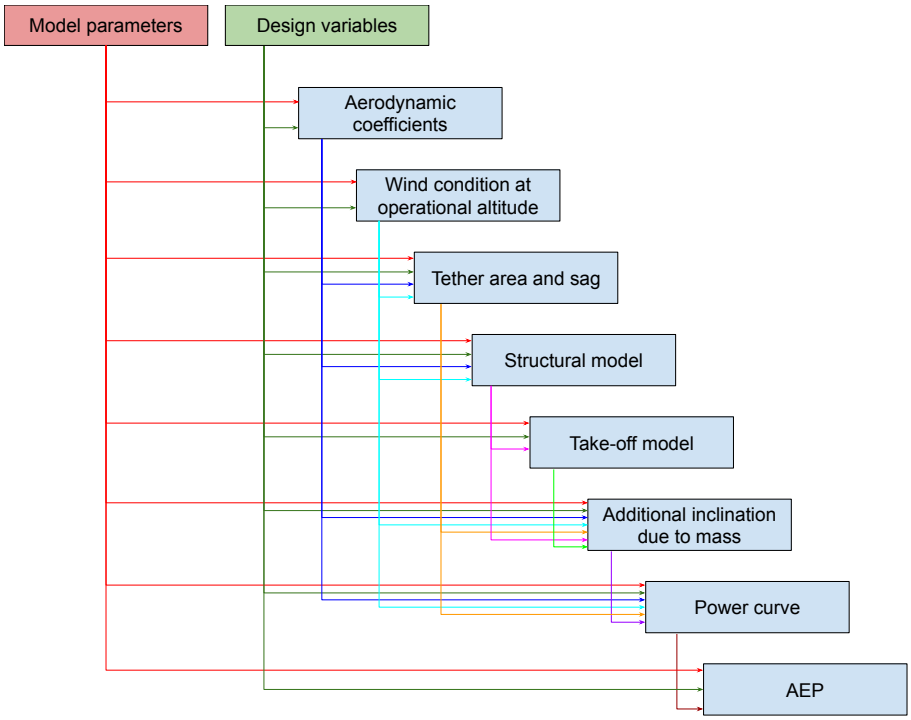

Figure 5.2: Flowchart of the code to evaluate the objective function AEP.

5.3 Algorithm validation

In this section, the validation of the optimisation is presented. Initially, a test to understand if the problem is well posed is performed. Later, a validation with literature benchmarks is carried out.

5.3.1 Algorithm reliability

A first test that can be performed to prove the reliability of the code is now presented. A single parameter, which is expected to influence the objective function, is varied within a range. The objective function should be a continuous and smooth function of this parameter.

This problem can be written as:

$$\begin{aligned} \min \quad & f(\mathbf{x}, \eta) \\ \text{s.t.} \quad & g(\mathbf{x}, \eta) < 0 \end{aligned} \tag{5.3}$$

where η represents the parameter to vary. The solution $f(\mathbf{x}, \eta)$, if plotted as function of the parameter η, is expected to be continuous and smooth. On the contrary, the norm of the design variables $\|\mathbf{x}\|(\eta)$ can have discontinuities.

This test is performed by making the upper bound of the design variables $\mathbf{q}_{CL}$ (Figure 5.3a) and the kite wing area (Figure 5.3b) to vary. To avoid local minima, each blue cross in Figure 5.3 is the best of 10 converged optimisation problems run with random initial conditions. $C_{L\,max}$ has been found to be critical for the convergence when it is higher than about 3. Thus, in this case, 15 optimisation problems are considered for the convergence (red crosses). The objective function, considering the scale of the images, is considered smooth enough.

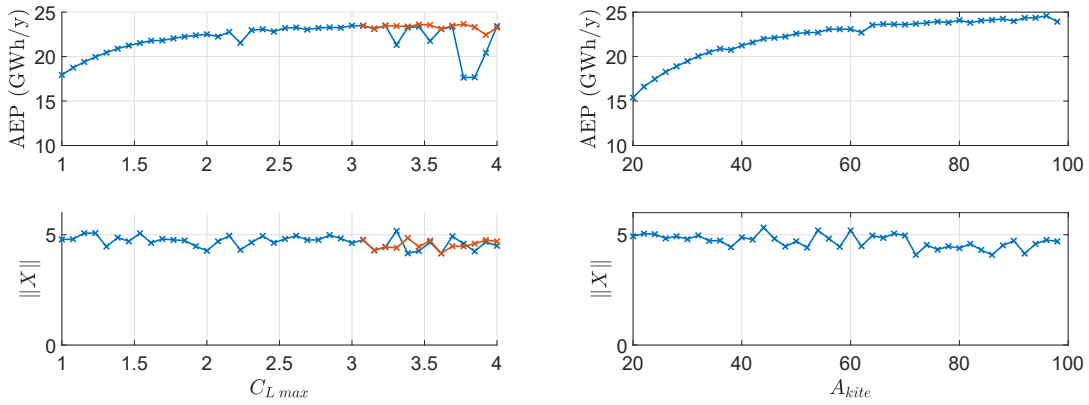

(a) (b)

Figure 5.3: Objective function and norm of the design variables as function of the maximum lift coefficient (a) and of the kite wing area (b). The blue line represents the best of 10 optimisation problems, the red of 15.

5.3.2 Validation

To validate the optimisation problem two benchmark solutions should be considered: one for the FG-AWES and one for the GG-AWES. The aim of the validation is not to perfectly replicate the literature design, but to verify if the model produces expected results.

The verification is based on two commercial designs, where only parts of the design and performance are published. Since not all the information are available, two procedures can be performed for the validation. The first is to set all the known parameters to reference values and to manually tune the others till when the the reference power curve is similar to the optimisation output. This first approach is difficult and time-consuming because the reference power curves are not necessary thought to maximise the power production and then the results may be very different.

The second is to set all the known parameters to reference values and the unknown to reasonable values. The objective function is changed to be the difference between the reference power curve and the optimisation output. In this way the two power curves lay on the top of each other. Finally, the design variables should be checked to be reasonable.

The second procedure is then used, as it is considered faster to implement and more precise.

Validation of FG-AWES

To validate the FG-AWES model, the simulated power curve of the *Wing 7* from *Makani Power* [41] is considered. The specifications of this technological demonstrator are given in Table 5.2. These information are taken from Table 28.8 of the book: *Airborne Wind Energy 2013* [42] and from other sources [43] [44].

The design variables for this problem are the lift coefficient and γ_t for all the wind speeds.

By running the optimisation, the main outputs are showed in Figure 5.4. Vander Lind in [41] showed that the design of *Wing 7* was performed by dividing the power curve into 4 regions according to the wind speed:

Maintenance of flight In this region, the tether tension is constant and the power increases linearly with the wind speed. The power could also be negative.

Generation In this region, the power and the tether tension are unconstrained, thus they are set to the Loyd optimum.

Tension contrained generation In this region, the tether tension is maximum and the power is linear.

Maximum power In this last region, the power is constant and the tether tension is decreasing.

par		Units	Description
A	3.96	m^2	Wing area
s	8	m	span
m	60	kg	Wing mass
$C_{L\ max}$	2	-	Maximum lift coefficient
β	40	°	Mean elevation angle
r	144	m	Tether length
P_{rated}	20	kW	Rated power

Table 5.2: Model parameters for the FG-AWES validation.

Referring to Figure 5.4, these four regions can be spotted. In the first part the tether tension is nearly constant and the power varies linearly. Between 7 and 9 m/s the power generation is unconstrained. Later, at around 10 m/s, the system reaches the maximum tether force and power output. Thus, optimisation outputs are found to have similar trends to the literature ones.

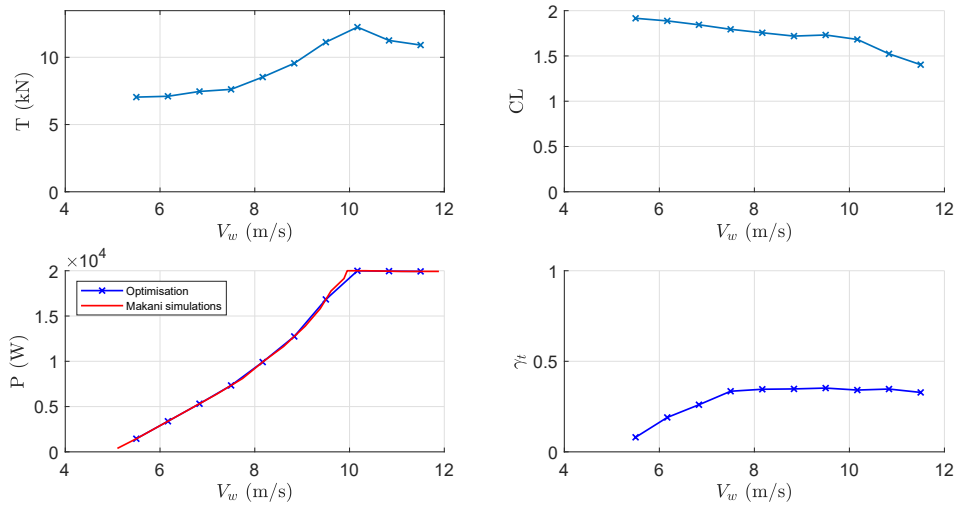

Figure 5.4: Relevant plot for the FG-AWES validation. On the top-left plot, the tether force is shown. On the top-right, the lift coefficient trend is plotted. On the bottom-left, the reference power curve and the optimisation outputs are shown. On the bottom-right, the coefficient for the on-board production is plotted.

Validation of GG-AWES

Concerning GG-AWES, the model has been validated with the second prototype *AP2* of the company *Ampyx Power* [13]. This prototype consists in a rigid wing aircraft, suitable for a comparison with the model. The power reference curve is taken from the simulations to optimize the trajectory proposed by Licitra [45], with the aircraft data given in a previous

work [46]. The simulations from Licitra are validated with the experimental data presented by Ruiterkamp [47]. The model parameters are given in Table 5.3.

par		Units	Description
A	3	m^2	Wing area
s	5.5	m	span
c	0.55	m	chord
m_{gl}	36.8	kg	Wing mass
d	2	mm	Tether diameter
m_t	1.5	kg	Tether mass
$cd_\perp$	1.2	-	Tether drag coefficient

Table 5.3: Model parameters for the GG-AWES validation.

The design variables for this optimisation problem are the tether length, the elevation, the lift coefficient and γ_{out} and γ_{in} for all the wind speeds.

The plots in Figure 5.5 show the reference power curves and some relevant trends out of the optimisation. Interestingly, the reel-out tether force is nearly constant, showing that the system is designed to have the constraint on the tether strength active for the investigated wind speeds. The lift coefficient is decreasing, to make the tether force to stay constant. The reel-in tether force highlights that this constraint is not active, thus γ_{in} is likely selected to maximise the cycle power. The tether length r is found to be 204 m. The elevation has a mean value of 20 °. Thus, the optimisation outputs have reasonable trends.

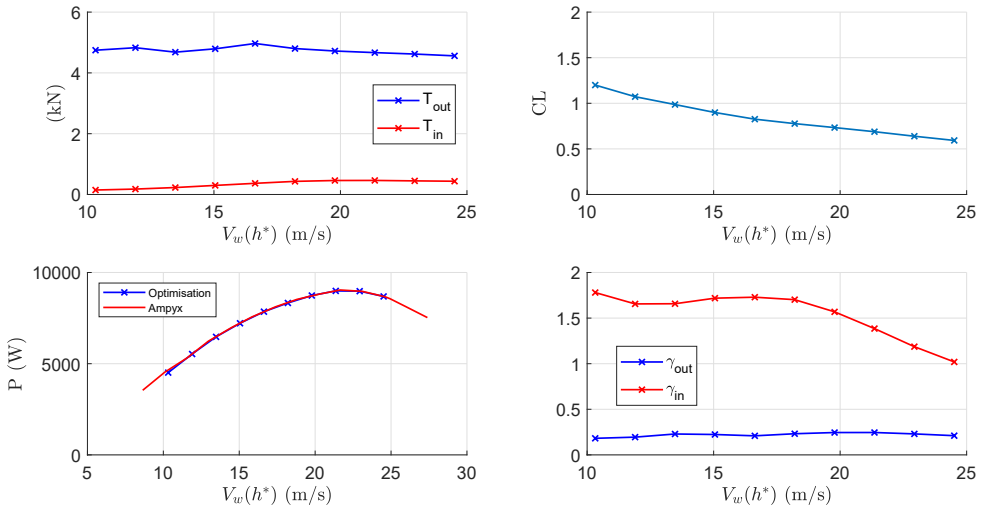

Figure 5.5: Relevant plot for the GG-AWES validation [45]. On the x-axis the wind speed refers to the operational altitude. On the top-left plot, the reel-out and reel-in tether force is shown. On the top-right, the lift coefficient trend is plotted. On the bottom-left, the reference power curve and the optimisation outputs are shown. On the bottom-right, the coefficient for reel-out and reel-in is plotted.

5.4 Optimisation results

In this section, the results of one optimisation problem are presented. The outputs of one optimisation problem are useful to understand in which way the design variables combine with each other to maximise AEP. This evaluation can be representative of a design performed by a engineer totally informed of the magnitude of all the parameters influencing the results.

In Figure 5.6 the main trends and outputs of an optimisation problem are shown. The rated power is set to 3 MW, the wing area to 70 m^2 and the maximum $C_{L\,max}$ to 2. The other parameters (i.e. material densities, efficiencies and so on) are set to the nominal values.

By looking at the figure, it can be noticed that part of the power is generated on-board (red line in the top-left plot) and part on the ground (blue line in the top-left plot). The combination of these power curves results in a smooth curve reaching the rated power at about 11 m/s. On the left, the main optimisation outputs are displayed. This system has a capacity factor of about 56 % and produces in one year 14.7 GWh. The total mass is influencing the Δ angle, showed in the bottom-right plot: at low wind speeds this angle is larger because the aerodynamic forces are smaller. At the cut-in wind speed the power is only ground generated: this can be noticed by looking at the power curves but also at the performance coefficients γ_{out} and γ_t. The lift coefficient is set to the upper bound, when the rated power is not reached. Later, it decreases to lower the glide ratio and thus the kite speed. Finally, the thrust needed to take-off is provided by the on-board turbines: the optimiser discards the configuration with on-board mass not useful for the power generation or for structural reasons.

This solution is not investigated in details because a more informative analysis is presented, with the help of the global sensitivity analysis, in the next sections.

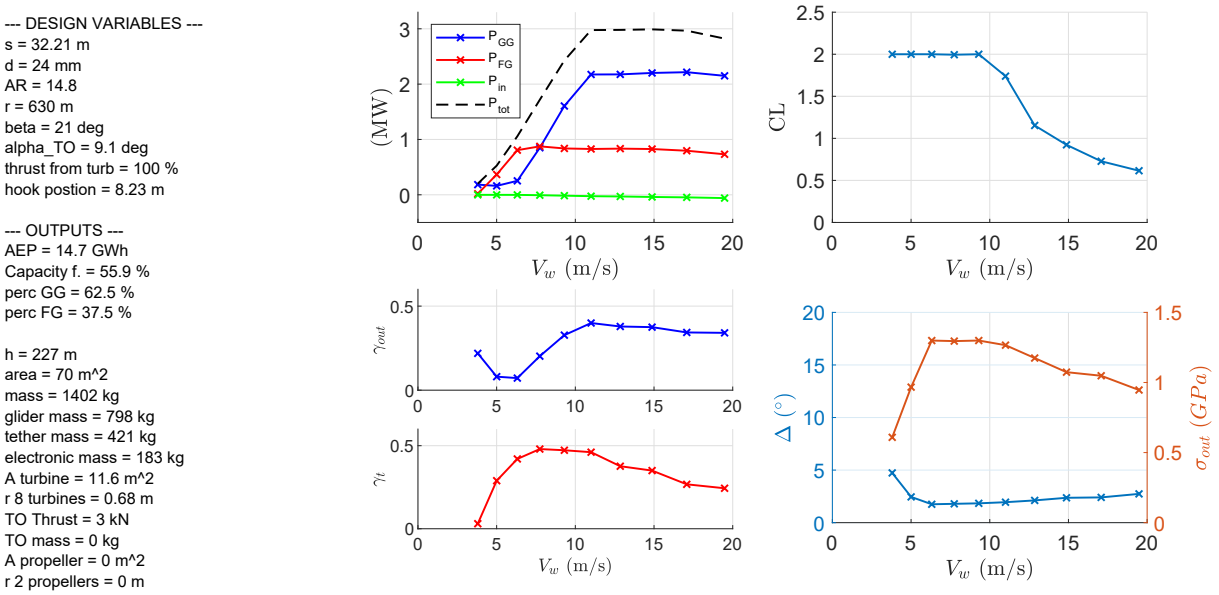

Figure 5.6: Typical results of an optimisation problem for the maximisation of the annual energy production.

5.5 Uncertainty quantification

In this section, the uncertainty quantification is presented. A utility scale system, with a rated power of 3 MW, is considered as study case.

Sixteen model parameters are selected as possible design drivers. Later, the importance of these is investigated with a *variance based decomposition* analysis. The description and the ranges of the parameters are given in Table 5.4. The research and design questions for each of them are outlined below:

$SF_{\sigma\ lim}$ Is the strength of the tether a design driver parameter? Should researchers focus on the development of a stronger material? This parameter can range from low values to quite high ones.

cd_0 Is the kite drag coefficient at zero lift a design driver? It is expected to be so, to which extent? This parameter can range from really low values to quite high ones.

$cd_\perp$ Is the tether drag coefficient a design driver? Does the designer need to think about a way to reduce it, using airfoil-shaped coating [3]? To model these kind of solutions this parameter can reach a lower bound of 0.6.

V Is the voltage of the power transmission lines relevant? Is the model for the electric cable design relevant for the output? A high voltage would decrease the electric cables section in the tether and therefore reduce the system drag. A big uncertainty is given to this parameter to simulate different scenarios.

ρ_{carb} Is the structural material density a design driver? A big uncertainly is given to this parameter, to include different possible design strategies that scale in a similar way (glider, biplane).

η_{out} Is the efficiency of reel-out a design driver? To which extent should the trajectory be optimised and the generator efficiency increased? Values from literature are assigned to this parameter [48] [49].

η_t Is the efficiency of on-board generation a design driver? To which extent should the trajectory be optimised, the generator efficiency increased and the transmission losses reduced? The range of this parameter is assigned after consultation with experts [16].

η_{in} Is the reel-in efficiency a design driver? In particular, to which extent is the reel-in model influencing the result? A big uncertainty to this efficiency is given.

$\eta_{t\ pr}$ Is the efficiency of the turbines used as propellers with respect to disc theory a design driver?

η_{pr} Is the efficiency of the propellers with respect to disc theory a design driver? Values from literature are assigned to this parameter [18].

$C_{L\ max}$ Is the maximum lift coefficient a design driver? To which extent should the aerodynamics be optimised? The mass of high aerodynamic performances will penalize high lift coefficients? This parameter can range between typical airfoil to multi-elements airfoil lift coefficients [50].

E_{gen} Is the power density of the generators a design driver? Should the designer look for really light and innovative solutions, or a traditional generator design would be enough? This parameter can range between typical [18] to really extreme and innovative values [51].

δ Is the maximum displacement of the structure a design driver? This parameter can range within typical values.

η_d^{min} Is the maximum allowed induction factor and turbine dimension relevant for the output? This parameter can range between typical values according to wind energy sector.

h_{min} Is the minimum allowed operational altitude relevant for the output? Considering that a kite producing 3 MW is expected to have big dimensions, a minimum operational altitude for safety reasons should be included in the analysis.

A_{kite} To which extent is the kite area influencing the power production? It is expected to be the most impacting parameter, with which trends? This parameter can range between small area values and large one, if a rated power of 3 MW is considered.

No uncertainty on the atmospheric model have been considered at this stage.

par	Min	Max	Units	Description
$SF_{\sigma\ lim}$	1.1	2	-	Safety factor on the tether strength [a]
cd_0	0.01	0.1	-	Drag coefficient at zero lift
$cd_\perp$	0.6	1.2	-	Cable drag coefficient
V	2	40	kV	Line voltage.
ρ_{carb}	800	2000	kg/m^3	Structural material density.
η_{out}	0.75	0.9	-	Efficiency of reel-out [b]
η_t	0.7	0.85	-	Efficiency of the on-board generation [c]
η_{in}	0.3	0.85	-	Efficiency of reel-in.
$\eta_{t\ pr}$	0.5	0.7	-	Efficiency of the turbine used in propeller mode with respect to disc theory (Section 3.5).
η_{pr}	0.7	0.9	-	Efficiency of the propellers with respect to disc theory
$C_{L\ max}$	1	4	-	Upper bound of the lift coefficient design variables ($\mathbf{q}_{CL}$)
E_{gen}	2.5	16	kW/kg	Power density of the motor/generators[d]
δ	1	10	%	Percentage of the span: this value times the span is the maximum tip and central displacement.
η_d^{min}	0.8	0.95	-	Minimum efficiency due to induction factor (eq. (3.65)) of the on-board turbines.
h_{min}	150	250	m	Minimum allowed operational altitude.
A_{kite}	15	100	m^2	Kite wing area.

[a] Cherubini [3] uses a safety factor of 1.25 on a tether strength of 1.5 GPa for FG-AWES. Bosman [52] gives an accurate description of how to design the cable for GG-AWES. The author highlights that the creep and the bending curvature in the winch are relevant for the design, requiring high safety factor.

[b] The value is comprehensive of losses due to generation and to the trajectory. Fechner [48] predicted that for big generators the efficiency could be of approximately 0.9, Argatov [49] computed a trajectory efficiencies higher than 0.9.

[c] This efficiency excludes disc theory losses, includes trajectory losses, aerodynamic efficiency of the turbines, generation efficiency and transmission.

[d] The reference literature value is 2500 W/kg [18], but a Belgian start-up with a new generator design is able to achieve more than 15000 W/kg [51].

Table 5.4: Model parameters ranges, distributions and descriptions.

5.6 Local sensitivity analysis with gradients

The simplest way to perform a sensitivity analysis is to look at the gradients of the outputs with respect to the inputs (model parameters). This information is showing how the design outputs are influenced by each of the inputs locally. The solution obtained with the mean values of the model parameter ranges (Table 5.4) is considered as reference. To compute the

gradients, each model parameter is varied of a small increment and the new optimisation problem is solved.

The gradients of AEP, of total mass m_{tot} and of tether length r with respect to the model parameters are shown in Table 5.5. The gradients have been normalized to make a comparison possible. Thus, they show how a non-dimensional change of the model parameter X_i impacts the output.

X	$SF_{\sigma\ lim}$	cd_0	$cd_\perp$	V	ρ_{carb}	η_{out}	η_t	η_{in}
$\frac{\partial AEP}{\partial X_i}$	-0.9	-2.36	-0.98	0.21	-0.58	0.53	0	0
$\frac{\partial m_{tot}}{\partial X_i}$	0	341.5	0	0	925.3	0	0	5.7
$\frac{\partial r}{\partial X_i}$	-22.5	75.2	-13.7	80.2	0	-15.7	20.2	11.1
	$\eta_{turb\ prop}$	η_{prop}	$C_{L\ max}$	E_{gen}	δ	η_{mon}^{max}	h_{min}	A_{kite}
$\frac{\partial AEP}{\partial X_i}$	0	0	2.30	0	0	0.22	-0.42	4.22
$\frac{\partial m_{tot}}{\partial X_i}$	710	0	1663.1	0	0	0	-250	4116.8
$\frac{\partial r}{\partial X_i}$	1.4	-34.3	96.6	15.7	0	0	159.6	120.2

Table 5.5: Gradient of AEP in GWh/-, m_{tot} in kg/- and r in m/- with respect to the model parameters **X**.

From this analysis the most relevant parameter for the annual energy production is the wing area A_{kite}. The drag coefficient at zero lift cd_0 and the maximum lift coefficient $C_{L\ max}$ follow. Concerning the mass, the highest sensitivity is also with the wing area. For the tether length, the minimum operational altitude h_{min} is the most important model parameter.

However, this analysis works only locally. To investigate how the model parameter uncertainties influence the outputs, a global approach should be considered.

5.7 Global sensitivity analysis

The procedure explained in Section 4.3.4 is considered to perform a global sensitivity analysis.

5.7.1 Evaluation procedure

A number of evaluations of the optimisation problem (*computational model* in Figure 4.4) has to be performed. These evaluations are taken in points filling the model parameter space.

In Figure 5.7, the process for the evaluation is presented. In Section 5.5, the model parameters that could be design drivers are selected and an uncertainty is assigned. Using the *Latin hypercube sampling* technique, a number *Nsample* of inputs are generated. Each input is a set of model parameters and, if a parallel computing approach is used, is sent to a worker. Each worker has to find the global maximum, given the problem with the selected model parameters. To find the global maximum, a number *N_max* of optimisation problems with different random initial conditions has to converge. Finally, the global maximum for each model parameters set (input) is considered to be the best of the *N_max* converged optimisation problems.

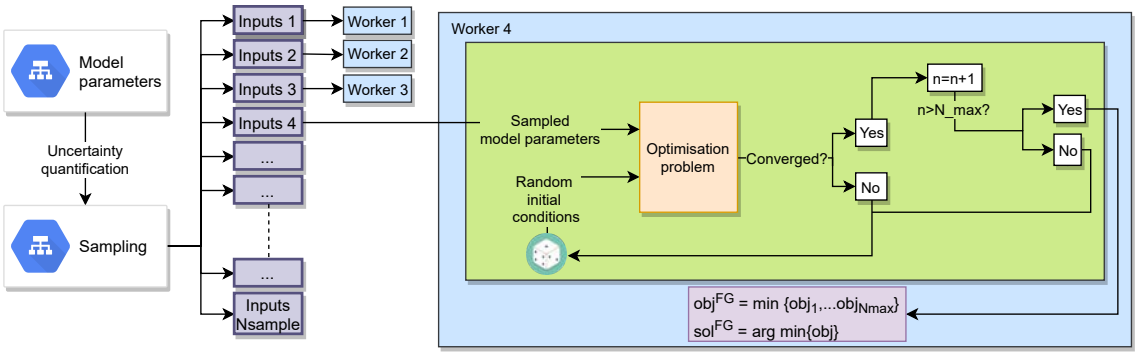

Figure 5.7: Flowchart of the evaluation procedure for a global sensitivity analysis, for the AEP maximisation case.

5.7.2 Output parameters

To describe the kite design, performed by the optimisation algorithm, many parameters can be considered as outputs. The outputs include the performance of the solution (i.e. annual energy production), the design parameters that describe the solution (i.e. mass, tether length etc.) and the Lagrange multipliers of the solution.

These outputs are:

AEP : annual energy production

AEP_{GG} : AEP ground generated

AEP_{FG} : AEP on-board generated

CF : capacity factor

m_{tot} : total mass

m_{gl} : structural mass

m_{el} : electronic mass

m_{te} : tether mass

m_{TO} : take-off equipment mass

r : tether length

β : elevation angle

d : tether diameter

Q : thrust to take-off

V_{in} : cut-in wind speed

V_{out} : cut-out wind speed

B : support position (Fig 3.9)

α_{TO} : climbing angle (Figure 3.12a)

h : operational altitude

s : span

AR : aspect ratio

δ_{out} : tip deflection

δ_{in} : inner deflection

A_{turb} : on-board turbines area

Q_{turb} : percentage of the thrust to climb provided by the turbines

E_{TO} : energy spent to take-off

A_{prop} : propellers area

t_{AA} : spar caps thickness in A (Fig 3.9)

t_{BB} : spar caps thickness in B (Fig 3.9)

t_{CC} : spar caps thickness in C (Fig 3.9)

λ_{te} : Lagrange multiplier of the tether strength constraint

λ_{Prated} : Lagrange multiplier of the rated power

λ_M : Lagrange multiplier of the structural material strength

$\lambda_{\delta out}$: Lagrange multiplier of the deflection at the tip

$\lambda_{\delta in}$: Lagrange multiplier of the deflection in the centre

λ_{CL} : Lagrange multiplier of the C_L upper limit

λ_{Akite} : Lagrange multiplier of the kite area constraint

λ_{hmin} : Lagrange multiplier of operational altitude lower bound

5.8 Global sensitivity analysis results

Once the uncertainties and the outputs are defined, the global sensitivity analysis can be performed, following the methods explained in Section 4.3. To test how many evaluations are necessary for the Sobol' indices to reach stable values, three global sensitivities are carried out with 400, 650 and 900 evaluations. Figure 5.8 shows the total Sobol' indices for the AEP, considering the three cases. The magnitude of the indices is considered stable with 400 evaluations. However, the results obtained with 650 points is shown in this chapter [1].

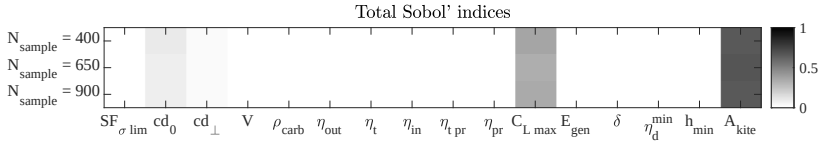

Figure 5.8: Total Sobol' indices for the AEP, considering 400, 650 and 900 evaluations.

Each of these points is the best (in term of objective function) of 10 converged optimisation problems run with random initial conditions (i.e. $N\_max = 10$ in Figure 5.7). If the $C_{L\,max}$ exceed 3, N_max is modified to 15. This is in accord with the tests performed in Section 5.3.1.

5.8.1 Statistics of design outputs

Once the evaluations of the kite design, for each set of model parameters, are carried out, a statistical approach to analyse the outputs can be used. Thus, the mean and standard deviation of the outputs is found.

The mean of the outputs is showing how kites would most likely look like, if AEP is maximised. This is the centre of the design space for future crosswind AWES development.

The standard deviation shows the sensitivity of the outputs to uncertainty. If an output variance is small, that output is likely going to be fixed in the future. If an output variance is high, that output is sensitive to uncertainties. Therefore, it is interesting to understand how it is influenced by the model parameter uncertainties.

In Table 5.6 the mean and standard deviation of the outputs are given.

Design performance

The average AEP is of 21.1 GWh, corresponding to a capacity factor of $CF = 0.80$. This shows the expectation of the system performances.

The average capacity factor is really high, a detailed analysis is necessary.

Design outputs

It can be noticed that most of the power is usually ground generated. All the outputs related to mass have big standard deviation, highlighting that the mass is strongly influenced by the input uncertainties. The tether length suggests that often the optimum is found

[1] To estimate the number of evaluations $Nsample$, one could use: $Nsample = 2n_p^2 + 4n_p + 1$; n_p is the number of model parameters.

	AEP	AEP_{GG}	AEP_{FG}	CF	m_{tot}	m_{gl}	m_{el}	m_{te}	m_{TO}	Δ
units	GWh	GWh	GWh	-	kg	kg	kg	kg	kg	$^\circ$
mean	21.1	15.8	5.3	0.80	3684	2884	160	626	14	8.4
SD	3.6	3.28	1.97	0.14	1705	1475	106	314	48	2.6
	r	d	h	β	V_{in}	V_{out}	s	AR	B	δ_{out}
units	m	mm	m	$^\circ$	m/s	m/s	m	-	m	m
mean	463	38	211	27.4	2.21	19.32	34.91	22.5	8.55	1.34
SD	116	8	45	2.6	0.82	0.61	8.62	3.9	2.16	1.76
	δ_{in}	A_{turb}	Q_{turb}	α_{TO}	Q	E_{TO}	A_{prop}	t_{AA}	t_{BB}	t_{CC}
units	m	m^2	-	$^\circ$	kN	Wh	m^2	mm	mm	mm
mean	1.88	83.6	0.92	24.27	15.69	6311.3	0.11	3	16	29
SD	1.08	59.0	0.19	20.5	12.04	4515.22	0.39	8	14	11
	λ_{te}	λ_{Prated}	λ_M	$\lambda_{\delta out}$	$\lambda_{\delta in}$	λ_{CL}	λ_{Akite}	λ_{hmin}		
units	GWh/-	GWh/-	GWh/-	GWh/-	GWh/-	GWh/-	GWh/-	GWh/-		
mean	1.94	33.27	0.54	0.12	0.29	3.82	4.56	0.91		
SD	1.67	10.56	0.58	0.17	0.31	5.47	3.09	1.14		

Table 5.6: Mean and standard deviation of the outputs for the AEP maximisation.

for short tethers and thus the altitude is low. However, the standard deviations of these two parameters are big, showing that they can vary. Also the tether diameter has a big uncertainty. On the contrary the elevation angle β has a low variance, showing that the configuration with $\beta \approx 27.4^\circ$ is often optimum. The average cut-in wind speed is really low, with a low variance. Considering the given Weibull distribution (Figure 3.15b), the configuration covering all the wind range is, on average, optimum. The span s has a big uncertainty. The aspect ratio AR has an average of 22.5, with a standard deviation of 3.8. The percentage of thrust given by on-board turbines is of 92%, showing that most of the times a take-off with propellers is not convenient.

Constraints

The Lagrange multipliers show how the objective function (AEP) is influenced by a change in the constraint limit. In other words, they outline how strong the constraints are. In this case, the Lagrange multiplier are normalized, to point out how the objective function changes with a relative change of the limit. The constraint with the highest Lagrange multiplier is the power rated constraint. It is limiting the most the power production, but it has also a high variance. Second, the Lagrange multiplier on the kite wing area: by changing this limit of 1%, on average a gain of 45 MWh is attained. However, it has high variance as well. The Lagrange multiplier on the maximum lift coefficient λ_{CL} and on the tether strength λ_{te} have also relevant means with big standard deviations. Finally, the Lagrange multiplier related to the minimum operational altitude λ_{hmin} and to the structural design (material strength λ_M, and deflections $\lambda_{\delta in}$ & $\lambda_{\delta out}$) have low mean and relative low variance. These constraints are not influencing the results, if compared to the others. Thus, they can be ignored in most of the cases.

5.8.2 Sobol analysis and design trends

It is interesting now to look at the sensitivity in the whole model parameter space. The sensitivity of the outputs variance with respect to the model parameters variance is evaluated with a *variance based decomposition*, explained in Section 4.3.5.

Figures 5.9 and 5.12 show the total Sobol' indices. Some plots, showing the key trends in the design, are presented to help the understanding of the indices. Clearly, the uncertainty

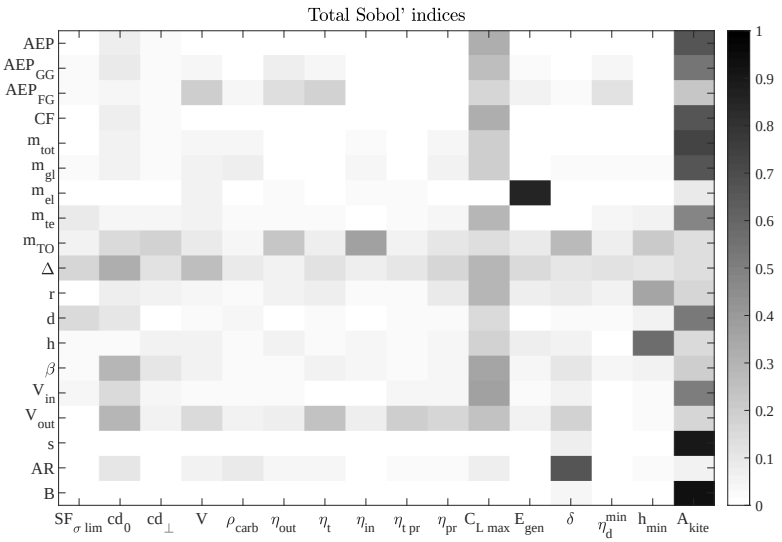

Figure 5.9: Graphical visualization of the total Sobol' indices for the AEP maximisation (first part).

of the wing area (A_{kite}) has the highest impact on almost all the kite subsystems.

The annual energy production AEP variance is mainly influenced by A_{kite}, followed by the maximum lift coefficient $C_{L\,max}$, the drag coefficient at zero lift Cd_0 and the drag coefficient of the tether $C_\perp$: these three last parameters are related to the aerodynamics.

It is interesting to look at the model parameters that are not influencing the outputs. The Sobol' indices on the AEP and on the CF outline that some parameters variance is contributing a little to the performance variance. For instance, the safety factor on the material strength $SF_{\sigma lim}$ variance is not impacting the AEP variance. If $SF_{\sigma lim}$ is fixed to high values, one can design a kite able to give an AEP equal to the one found with $SF_{\sigma lim}$ fixed to low values.

Similar analyses can be carried out for: line voltage V, structural material density ρ_{carb}, efficiency of reel-out η_{out} and reel-in η_{in}, efficiency of on-board generation η_t, efficiency of the propellers η_{pr} and of turbines used as propellers $\eta_{t.pr}$, generators power density E_{gen}, maximum structural displacement δ, minimum efficiency due to disc theory η_d^{min} and minimum operational altitude h_{min}.

Many considerations can be drawn from this analysis. When designing a kite, aiming to maximise AEP, the parameters with a low Sobol' index can be fixed to conservative values. Then, a preliminary kite design can be performed by designing the parameters with high Sobol' indices. Once the preliminary design is performed, one can consider the parameters with low Sobol' indices to evaluate them for the specific kite design.

Thus, an investigation of the high Sobol' indices parameters can give guidelines to the designer.

The metamodels created for the *variance based decomposition* (see Section 4.3.4 for details) can be used to understand the dependencies outlined by the Sobol' indices. In Figure 5.10a, the capacity factor CF is plotted as a surface, function of A_{kite} and $C_{L\,max}$. An increase of the wing area, when the area itself is small, can be really beneficial for the CF. A similar consideration can be derived for $C_{L\,max}$. Really high capacity factors can be attained with an increase of area and maximum lift coefficient. When a crosswind AWES is designed, a big focus should be given to the selection of the airfoil and of the wing area.

For a given rated power, the choice of these two parameters is essential to a obtain high capacity factors.

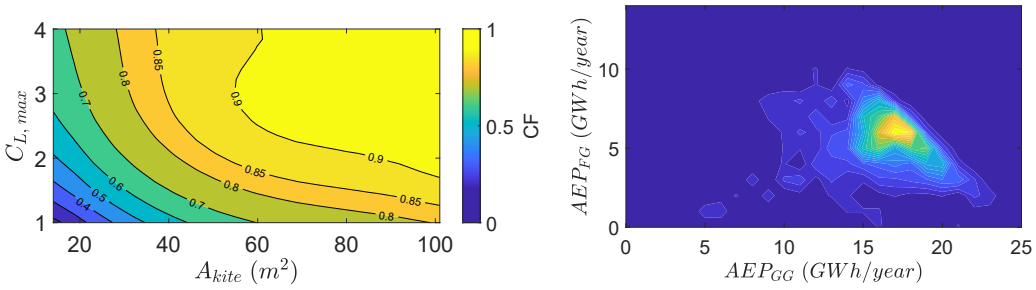

(a) (b)

Figure 5.10: Contour plot of the metamodel of the capacity factor as function of the wing area and the maximum lift coefficient (a) Evaluations density of the combination of annual energy production generated on-board (AEP_{FG}) and on the ground (AEP_{GG}) (b).

It is interesting to understand where the generation of power would be optimum from a physical point of view. Figure 5.10b shows the density of the evaluations of the two annual energy productions types. Most of the time, the power is mainly ground generated (AEP_{GG}) and all the solutions present both the generation types at the same time. The reason why the two generation types coexist is the same as the one given for the optimisation problem result (Section 5.4): it would be optimum, from a physic point of view, to have turbines big enough to take off and use them during the generation phase.

Looking at the power ground and on-board generated, they are highly influenced by the respective efficiencies η_t and η_{out}, besides that by the line voltage V, the aerodynamics and the wing area. In Figure 5.11 the evaluations are shown together with a polynomial fit, highlighting the trends with respect to the efficiencies of reel-out and of on-board generation. As expected more power is ground generated if the efficiency of reel-out η_{out} increases and more power on-board generated is the relative efficiency η_t increases.

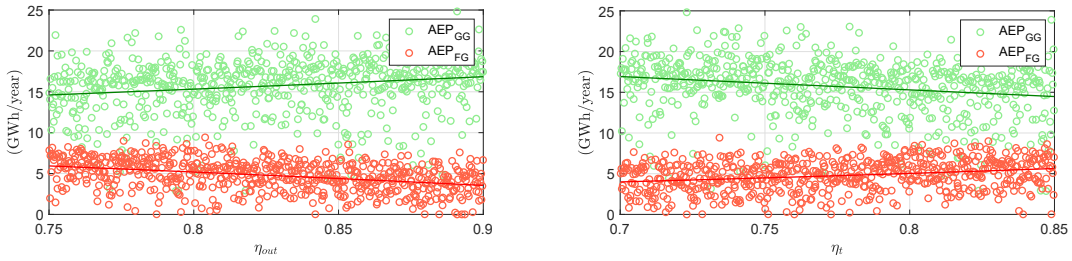

(a) (b)

Figure 5.11: Evaluation of the annual energy ground and on-board production as function of the reel-out (a) and on-board efficiency (b).

The variance of structure, tether and total mass are strongly influenced by the wing area and the maximum lift coefficient.

The tether length and the operational altitude variances are mainly influenced by minimum operational altitude h_{min} and the maximum lift coefficient. The diameter has a dependence on the safety factor $SF_{\sigma\ lim}$, the wing area and the maximum lift coefficient.

The wings geometric dimensions (span s and aspect ratio AR) have to combine to give the wing area A_{kite}. Interestingly the aspect ratio AR is mainly influenced by the maximum

structure deflection while the span by the wing area.

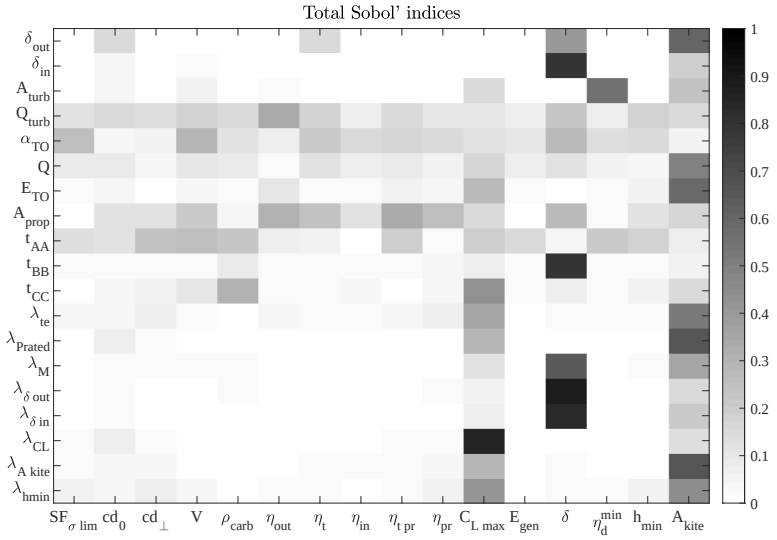

Figure 5.12: Graphical visualization of the total Sobol' indices for the AEP maximisation (second part).

The turbine area is mainly influenced by the minimum allowed efficiency due to disc theory η_d^{min}. The design of the propulsion system is instead of not so clear interpretation. This is because the take-off sub-system mass is generally small (Table 5.6). The climbing angle α_{TO} variance has not any clear dependence. This means that the climbing angle can be any value and the objective function is not influenced. In other words, the take-off strategy does not impact the AEP.

The dimensions of the spar caps in section B are influenced by the maximum structure deflection, while in section C by density of the structural material ρ_{carb} and by the maximum lift coefficient. In section A the thickness and the relative variance are small (Table 5.6).

Finally, the Lagrange multipliers of the structural constraints are on average small (see Table 5.6). They depend manly on the maximum structure deflection. The other Lagrange multipliers depend on the wing area and on the maximum lift coefficient. It is interesting to plot them as surfaces function of these two model parameters.

In Figure 5.13a, the Lagrange multiplier of the tether strength constraint is shown, highlighting that, with an increase of area and maximum lift coefficient, this constraint is weaker and weaker.

Lagrange multipliers are a property of the design, performed by the optimiser. They show how strong the constraint is, once the design is carried out.

In the first part of this section, the Sobol' indices of AEP are analysed. One outcome is that $SF_{\sigma lim}$ is not influencing AEP. One can fix this value and perform the design, based on the high Sobol' indices model parameters. Once the design is performed, the Lagrange multiplier on the tether strength shows how strong this constraint is. In other words, it shows how AEP is sensible to a change in the tether strength (i.e. to a change in the safety factor $SF_{\sigma lim}$). Interestingly, the Lagrange multiplier on the tether strength is not highly dependent on $SF_{\sigma lim}$, according to the Sobol' indices. This means that an improvement on the tether strength would not make the constraint strength to decrease. Instead, an increase of the wing area and of high maximum lift coefficient make the constraint weaker. Thus, the easiest way to have the constraint of the tether strength weak is to design big

kites with high $C_{L\,max}$, it is not to improve the tether strength.

To summarize, the variance of $SF_{\sigma lim}$ is not influencing neither AEP nor the λ_{te}. Thus, high safety factors could be used, not influencing the design performance and the constraint strength. This is because the kite can be designed in other ways, still having the same performance.

In Figure 5.13b, the constraint of the rated power is shown. Clearly, this constraint is stronger when the wing area and the maximum lift coefficient are higher because the system would have a bigger benefit to increase the rated power.

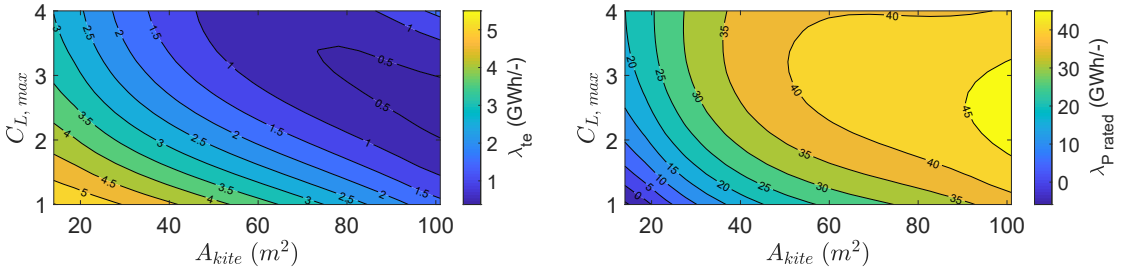

(a) (b)

Figure 5.13: Contour plot of the metamodel of the Lagrange multiplier of the constraint on the tether strength λ_{te} (a) and on the rated power λ_{Prated} (b) as function of the wing area A_{kite} and the maximum lift coefficient $C_{L\,max}$.

In Figure 5.14a, the Lagrange multiplier of the upper bound of the lift coefficient is shown. It should be reminded that $C_{L\,max}$ in the optimisation problem is the upper bound of the design variables $\mathbf{q}_{CL}$. Clearly, this constraint is active and strong when the upper bound itself $C_{L\,max}$ is low. For big wing areas and high $C_{L\,max}$ this constrain is not active or very weak. In other words, a high maximum lift coefficient $C_{L\,max}$ would often not bring any benefit to the annual energy production. The structural material density variance, representing aircraft standard designs and designs with lower mass such as multi-planes, does not influence λ_{CL}. This is showing that the strength of the constraint on the maximum lift coefficient is not influenced by the material density. In other words, designs with low material densities, such as multi-planes, require high lift coefficient as normal aircrafts. However, this analysis is not modelling in an accurate way a multi-plane design, neither the structural design of a high lift coefficient airfoil. These observations are carried out to investigate on the necessity of extremely high lift coefficients in multi-planes [50].

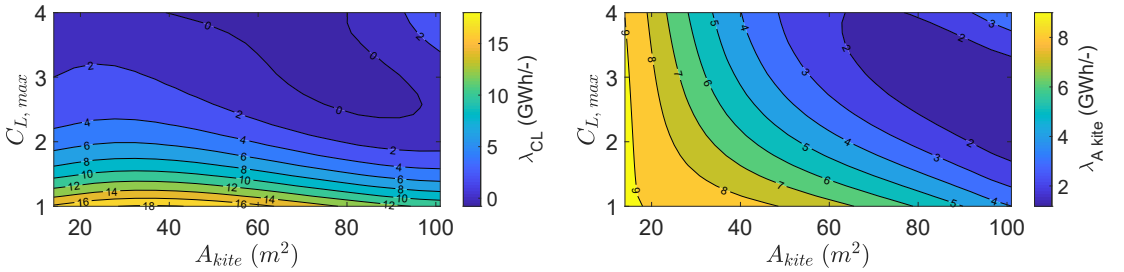

(a) (b)

Figure 5.14: Contour plot of the metamodel of the Lagrange multiplier of the constraint on the lift coefficient λ_{CL} (a) and on the wing area λ_{Akite} (b) as function of the wing area A_{kite} and the maximum lift coefficient $C_{L\,max}$.

In Figure 5.14b, the Lagrange multiplier of the wing area constraint is shown. Also in this

case, the constraint is stronger for low A_{kite} and $C_{L\,max}$.

Finally, to conclude the understanding of the results, the correlations between all the data (inputs and outputs) can be spotted in a statistical way. A polynomial fit can be performed between each pair of data and, if a good correlation is found, the output can be displayed and interpreted. For instance, in Figure 5.15a, the evaluations of the operational altitude h are plotted as function of the tether length r, showing the expected correlation between the two. The operational altitude is, most of the times, set by the optimiser to the lower bound (varying in the global sensitivity analysis between 150 and 250 m). This is because a short tether is contributing less to the system drag than a long one: a reduction of the drag is bringing more benefits to the system, compared to an increase in altitude. However, the Lagrange multiplier on this lower bound, is on average small (Table 5.6). This means that this constraint is weak. It is interesting to notice that λ_{hmin} is almost not influenced by the minimum operational altitude variance. Figure 5.15b shows the trend with the wing area A_{kite} and $C_{L\,max}$. For big kites with high maximum lift coefficient, this constraint is weak. It should be remarked that a model of the trajectory, not available in this work, would discard solutions with extremely short tether.

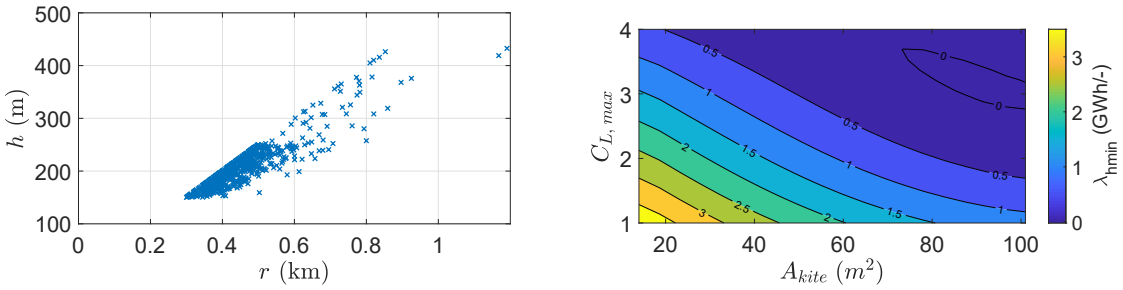

(a) (b)

Figure 5.15: Evaluations of operational altitude h as function as tether length r (a) and contour plot of the metamodel of the Lagrange multiplier of the constraint on minimum operational altitude as function of the wing area A_{kite} and the maximum lift coefficient $C_{L\,max}$ (b).

Other trends can give an understanding of the results. Figure 5.16 shows the evaluations of the mass density as function of the aspect ratio. The red crosses represent commercial gliders [53], while the blue represent the output of the optimisation problems. The mass densities for crosswind AWES are higher than for commercial gliders because the aerodynamic loads are much larger.

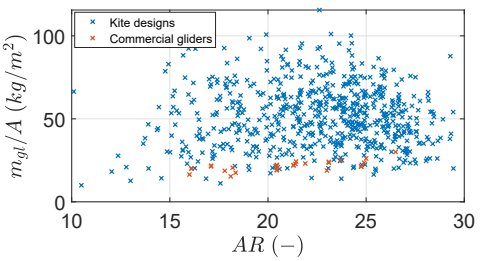

Figure 5.16: Mass density as function of aspect ratio.

5.9 Global sensitivity analysis results for a fixed wing area

It can be useful to look at a global sensitivity analysis with a fixed wing area. In this case, the wing area is fixed to 30 m^2. The Sobol' indices for this case are shown in Appendix A.1.

The most important parameter, if the wing area is fixed, is the maximum lift coefficient $C_{L\,max}$. It is the main responsible for the increase in AEP: Figure 5.17a shows how it increases. The annual energy production does not have any relevant benefit, if the $C_{L\,max}$ is increased higher than about 3. This can be noticed by looking at the AEP trend (Figure 5.17a), as well as at the Lagrange multiplier of the $C_{L\,max}$ trend (Figure 5.17b). As soon as the AEP reaches a plateau, λ_{CL} goes close to zero, highlighting that a small increase in the $C_{L\,max}$ would not influence the objective function (AEP).

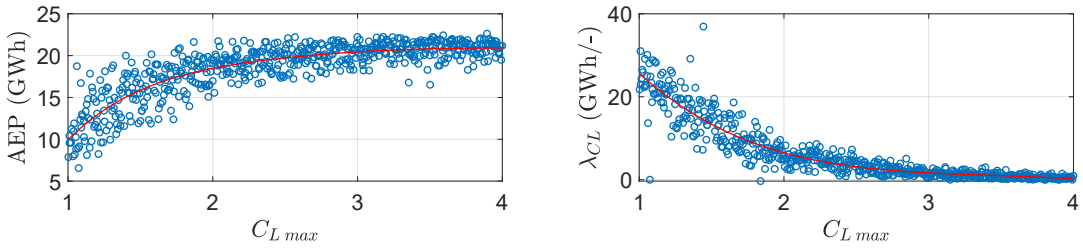

(a) (b)

Figure 5.17: Evaluations of AEP (a) and λ_{CL} (b) as function of maximum lift coefficient $C_{L\,max}$.

According to the Sobol' indices, after $C_{L\,max}$, Cd_0 is the main responsible for the CF variance. In Figure 5.18a, the metamodel of CF is shown as function of these two aerodynamic coefficients. The highest capacity factors can be obtained with low Cd_0 and relative low $C_{L\,max}$. To have a high capacity factor, the aerodynamics of the kite should be designed to have a low Cd_0 and, at the same time, a high enough maximum lift coefficient according to Figure 5.18a. It should be remarked that Figure 5.18a is created for a rated power of 3 MW and a wing area of 30 m^2. With other parameters, the contour lines would be shifted.

Figure 5.18b shows how the aspect ratio varies with the maximum structure deflection δ. If the maximum tip and central deflection is set to 1 % of the span, AR is of about 15 to make the structure stiff. If this limit is increased, the aspect ratio rises as well. For small δ, the aspect ratio evaluations are close the the mean, showing that the maximum deflection is the main model parameter driving AR. For higher δ, the evaluations are sparser: the maximum deflection is not any more the only parameter driving the aspect ratio. When designing a kite to maximise AEP, one could consider an aspect ratio according to Figure 5.18b, if the maximum structure deflection is low. For high δ, one should consider also $C_{L\,max}$, Cd_0 and the structural material density ρ_{carb}, according to the Sobol' indices.

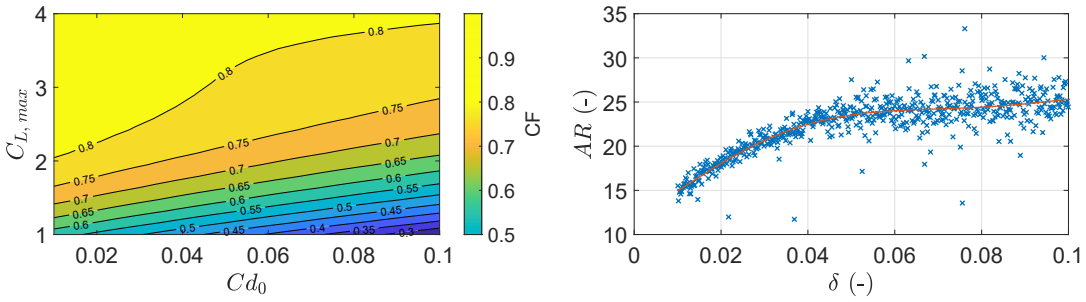

(a) (b)

Figure 5.18: Contour plot of the metamodel of the capacity factor as function of the $C_{L\,max}$ and Cd_0 (a). Evaluations and polynomial fit of the aspect ratio as function of the maximum structure deflection (b).

5.10 Global sensitivity analysis results considering wind resources uncertainties

It is interesting to see how the design is influenced by the wind conditions. Thus, a global sensitivity analysis is run, considering the wind-related uncertainties. In Table 5.7 a range is given to the wind shear coefficient α and to the Weibull parameters. All the uncertainties presented in Table 5.4 are also considered.

par	Min	Max	Units	Description
α	0.1	0.3	-	Wind shear coefficient
A	6	15	m/s	Weibull scale parameter (eq. (3.92))
k	1	3	-	Weibull form parameter (eq. (3.92))

Table 5.7: Wind resources parameters ranges.

5.10.1 Statistics of design outputs

The mean and the standard deviations of design performance, design outputs and Lagrange multipliers are given in Table 5.8.

Similar conclusions to the ones presented for Table 5.6 can be drawn. The outputs have similar magnitude, showing that the optimum designs are generally not changing if the wind resources change. The only output parameter that changes significantly is the cut-out wind speed (V_{out}). In this case, the average value increases, and the standard deviation changes from 0.6 to 5.9 m/s. This outlines the fact that the optimiser look for high capacity factor by moving the V_{out} according to the Weibull distribution.

	AEP	AEP_{GG}	AEP_{FG}	CF	m_{tot}	m_{gl}	m_{el}	m_{te}	m_{TO}	Δ
units	GWh	GWh	GWh	-	kg	kg	kg	kg	kg	°
mean	20.39	15.55	4.83	0.78	3445	2638	161	625	20	8.3
SD	4.33	3.89	2.16	0.16	1681	1482	113	326	68	2.6
	r	d	h	β	V_{in}	V_{out}	s	AR	B	δ_{out}
units	m	mm	m	°	m/s	m/s	m	-	m	m
mean	467	38	217	27.88	2.34	22.66	34.36	22.01	8.38	1.15
SD	123	8	53	2.55	0.88	5.88	8.65	4.52	2.09	1.91
	δ_{in}	A_{turb}	Q_{turb}	α_{TO}	Q	E_{TO}	A_{prop}	t_{AA}	t_{BB}	t_{CC}
units	m	m^2	-	°	kN	Wh	m^2	mm	mm	mm
mean	1.92	78.11	0.88	24.04	14.77	6380	0.2	3	15	27
SD	2.36	61.48	0.27	21.49	12.27	4654	0.66	9	12	11
	λ_{te}	λ_{Prated}	λ_M	$\lambda_{\delta out}$	$\lambda_{\delta in}$	λ_{CL}	λ_{Akite}	λ_{hmin}		
units	GWh/-	GWh/-	GWh/-	GWh/-	GWh/-	GWh/-	GWh/-	GWh/-		
mean	2.08	37.8	0.49	0.11	0.27	3.85	4.28	0.95		
SD	1.79	17.07	0.57	0.17	0.32	5.76	3.21	1.3		

Table 5.8: Mean and standard deviation of the outputs considering wind resources uncertainties.

5.10.2 Sobol analysis and design trends

The Sobol' indices can now be investigated. Figure 5.19 shows the first part of the outputs, Figure A.3 the second.

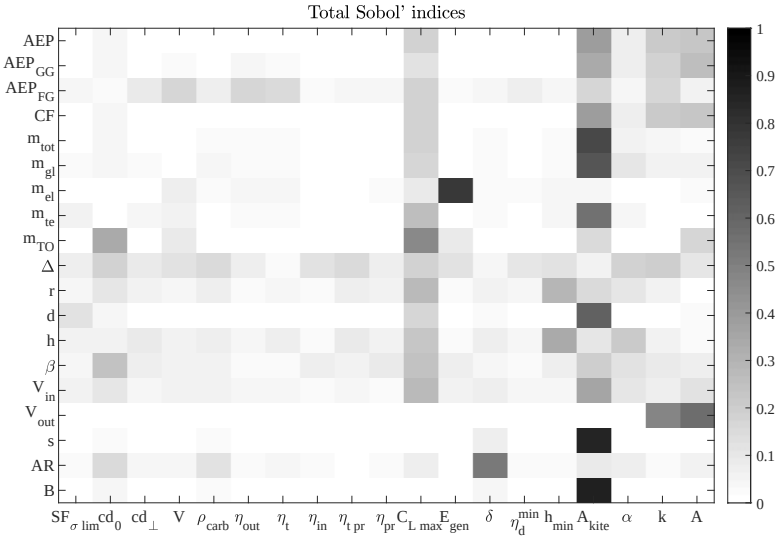

Figure 5.19: Graphical visualization of the total Sobol' indices considering the wind resources uncertainties (first part).

The annual energy production is influenced by the the wind resources uncertainties. However, the wing area A_{kite} and the maximum lift coefficient $C_{L\,max}$ are still driving the performance. Figure 5.20a shows the surface plot of the metamodel relating the *Weibull scale parameter* A and the wing area A_{kite} to the capacity factor. For low wind resources regions, a high capacity factor can be obtained by increasing the wing area.

Figure 5.20b shows how the Lagrange multiplier on the rated power varies with the scale parameter. Increasing A, the constraint is stronger: it would be more and more convenient to have a bigger rated power.

By analysing the mean and standard deviation of the outputs (Table 5.8) and the Sobol'

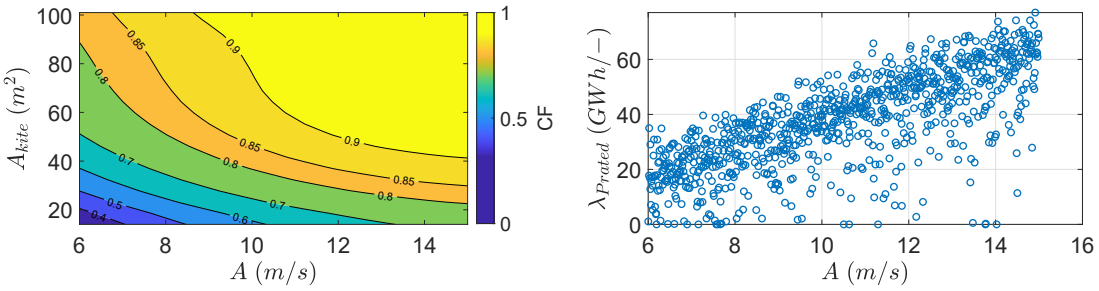

(a) (b)

Figure 5.20: Contour plot of the metamodel of the capacity factor as function of the scale parameter A and the wing area A_{kite} (a) and Lagrange multiplier of the rated power as function of the scale parameter (b).

indices, it tuns out that the design of the kite and of the tether is not influenced by the wind resources. Thus a kite can be designed keeping the wind resources fixed, and it can be used in all the scenarios.

This section is showing that, to achieve high capacity factors in low wind regions, a large wing area is necessary. Given a wing area, the design of the kite is not influenced by the wind resources uncertainties. Thus, a big kite can be used with a large rated power in high wind regions, and with lower rated power in low wind regions. In this way, high capacity factors are obtained in both regions.

5.11 Discussion

In this chapter, the methods presented in Chapter 4 are used to evaluate the model proposed in Chapter 3. A detailed analysis on the optima designs, with respect to AEP, is presented.

First, the optimisation problem formulation is described. The optimiser performs a design of the kite to maximise the annual energy production. Some tests to validate the model are carried out. One optimisation result is shown, to introduce typical trends.

The uncertainties of model parameters, influencing the kite design, are given. Most of the parameters uncertainties are epistemic uncertainties: in the future they will be fixed, but at this stage it is interesting to understand how the design varies with them.

How these uncertainties influence the configuration design is investigated. The design, performed by the optimisation algorithm, is evaluated in many points, according to the model parameter uncertainties. As a first analysis, the mean value of the outputs defines the expected configuration. The standard deviation of the outputs indicates if they are more or less sensitive to the model parameter uncertainties.

After, a global sensitivity analysis shows how the outputs variances are influenced by the model parameters variances. This analysis brings to the following discussion.

A crosswind AWES designer, at a first stage, should focus on the design of wing area and of kite aerodynamics. These characteristics can be designed, by assuming the other parameters with conservative values. In other words, to design a system for a given capacity factor, one could assume the model parameters with low Sobol' indices (e.g. the tether strength safety factor, efficiencies due to the trajectory and so on) and perform a preliminary design based on the high Sobol' indices parameters. Once the preliminary design is performed, an accurate estimation of the model parameter with low Sobol' indices for the given design can be carried out. In this way, strong configurations can be obtained.

In this chapter, some information useful to determine interesting research areas can be found. To maximise AEP, it would be interesting to study kites with really low Cd_0 and high enough lift coefficients. As shown in this chapter, extremely high lift coefficients are, on average, not attractive. It is also shown that a reduction of the structural material density, representing kite design with lower mass such as multi-planes, does not require high lift coefficients. However, the structural model is not accurate for these designs. Thus, a research topic could be on the investigation of optimal aerodynamic designs, considering the structural properties. An accurate aerodynamic and structure study could give also information related to the wing cost. The design of the wing area of the kite is indeed driven by cost considerations. Thus, it could be interesting to develop some accurate cost models for the kite structure. Studies on how to decrease of the tether drag coefficient can also bring benefits, according to the Sobol' indices.

It is shown that the kite design does not depend on wind resources, the wing area is. The same capacity factor can be obtained in different regions, by designing the wing area accordingly.

If in the future some regulations will impose high safety factors on the tether, the kite could be designed to produced high capacity factors anyway. Same conclusions can be drawn for a regulation on the minimum operational altitude. These two considerations show the strength of crosswind AWES, with respect to these two possible regulations.

The analyses presented in this chapter, show the big potential of crosswind AWES, in term of power production. They point out the strength that this technology will have in the future.

Chapter 6

Cost modelling of a generic crosswind AWES

In this chapter, the cost models for a generic crosswind AWES are presented. The presented cost models refer to GG-AWES and FG-AWES. Some cost functions are common between the two generation strategies, some others are typical of one solution.

In literature, a cost model related to GG-AWES is introduced by the master thesis of Heilmann [54] and used to economically assess a kite wind farm by Heilmann himself [55], Grete [56] and De Lellis [57]. All these works deal exclusively with soft kites. Thus a generalization is necessary.

Concerning FG-AWES, Bauer [50] proposes a model that is distinguishing between drivetrain cost, including generators and power electronics, and a unique cost, including airframe, tether, ground station, development costs and the profit margin of the power plant manufacturer. No other models, to the best knowledge of the author, are available for FG-AWES. Thus, in this work a simple cost model is proposed, using the available models as much as possible.

In this chapter, the cost functions of each subsystem are given with the relative numerical values of the parameters. The considered uncertainties on the cost model parameters are also shown. If the standard deviation of one parameter is null, no uncertainty is given to it. The cost of the components is estimated in 2019 euros.

6.1 Kite structure

To describe the cost of an aircraft in an accurate way, an accurate structural design should be developed, to assess the cost of each sub-component. In this work a simple cost function is assumed, relating the cost to the kite mass.

To give an appropriate range to the material cost, an investigation on the costs of some existing gliders is performed [53]. It should be noted that commercial glider prices also include non-structural components. The trend relating the empty mass and the price are showed in Figure 6.1. The cost function is thus:

$$C_{glider} = p_{gl} \cdot m_{wing} \ (€) \tag{6.1}$$

Where the mass of the glider is estimated with the structural model. The coefficient p_{wing} is varying between 20 and 200 €/ kg.

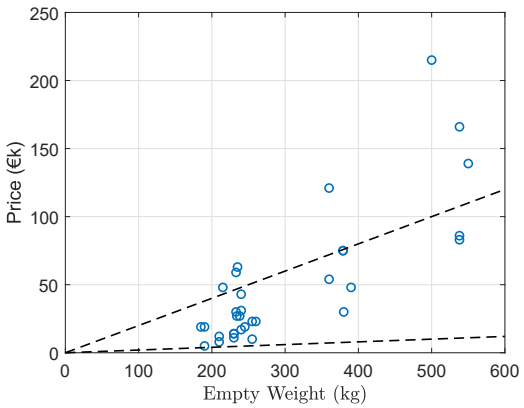

Figure 6.1: Price of commercial gliders as function as the manufacturer's empty weight [53].

6.2 Tether

The cost of the tether is proportional to its mass [54]. Once the mass is estimated, the cost can be found. In Table 6.1 the estimated mean and the standard deviation of price per kg are reported [54].

The electric cable is considered to be made of aluminium, because it is lighter than copper [3]. The presence of both the structural and electrical components needs a customised design and manufacturing, that increase the cost. A manufacturing factor f_{te} is applied to the cable costs, if it needs the specific design.

	Mean	SD	Units
Structural tether: p_{te}	200	50	€/kg
Electrical cables: $p_{el\ cable}$	2	-	€/kg
	Minimum	Maximum	
Manufacturing cost f_{te}	1.2	2	-

Table 6.1: Structural tether cost [54] [58], electrical cable cost [59] and manufacturing factor.

Depending on the fibres types and on the operational stress, a working life due to creep can be determined for the structural component of the tether.

Bosman [52] proposed a tether design considering one single stress level, showing that the load cycles during the generation phase are small. Therefore, the stress can be considered constant. The author considers that the tether is not operating at the nominal tension all the time, due to the reel-in phase. Moreover, during night and during winter the average temperature is reduced and therefore it increases the life. In Figure 6.2a the curves relating the tether stress to the life for three different ropes are shown [52].

In this analyses, the tether stress is not constant, but varies with the wind speed. Thus, it would be too approximative to estimate the tether life just by considering the maximum tether stress. Moreover, this approach would lead the optimisation algorithm to unreasonable designs. Bosman [52] suggests the usage of a Miner' Rule approach, thus a reformulation of this rule for creep damage is proposed.

The Miner's Rule [60] is an empirical rule used to compute the life of a structural component when load cycles, with different stress levels, are applied to it. Considering a generic material, a plot similar to the one presented in Figure 6.2b can be experimentally found. To explain this rule, it is considered a case in which two load levels S_1 and S_2 are applied for a number

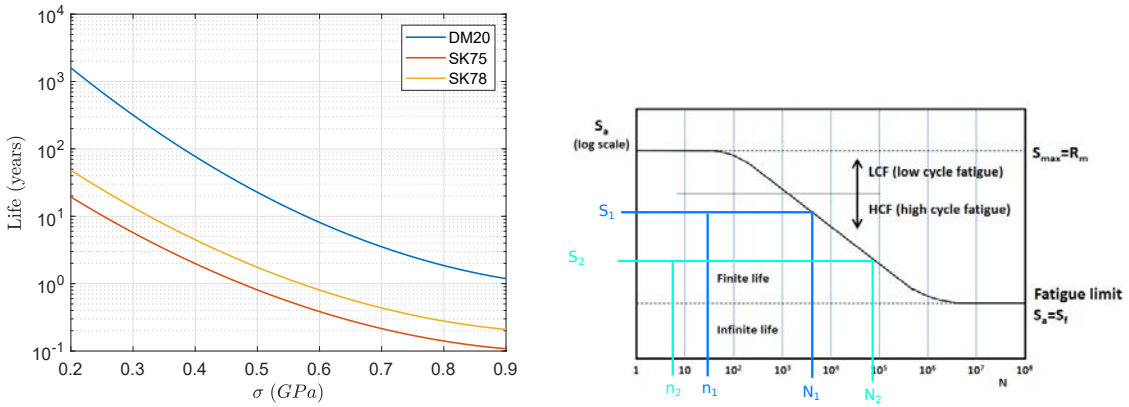

(a) (b)

Figure 6.2: Working life as function of tension stress for different types of Dyneema tether at T=20° C [52](a) and Wöhler curve for a generic material with in the x-axis the number of cycle and in the y-axis the stress level (b).

of cycles n_1 and n_2. If the stress S_1 was applied a number N_1 of cycles, the material would have failed. The same for S_2 and N_2. The Miner's Rule states that the material fails when:

$$\sum_{i=1}^{n_{loads}} \frac{n_i}{N_i} = 1 \tag{6.2}$$

In the example when $\frac{n_1}{N_1} + \frac{n_2}{N_2} = 1$. A similar approach is used to compute the life of the tether, with respect to Figure 6.2a. According to the wind speed, a different stress level is applied to the tether $\sigma(V_w)$. If only this stress was applied to the tether, the life would have been $L(\sigma(V_w))$ (the functions plotted in Figure 6.2a). Considering the function describing the wind speed frequency $f(V_w)$ (Weilbull distribution, Equation (3.92)), it is possible to find for how long a stress level is applied to the tether in one generic period of time T_{te}:

$$l(V_w) = f(V_w) \cdot T_{te} \tag{6.3}$$

Considering the Miner's Rule, and the safety factor $SF_{\sigma\, lim}$ the tether fails when:

$$\sum_{i=1}^{n_{Vw}} \frac{l(V_{w\,i})}{L(SF_{\sigma\, lim} \cdot \sigma(V_{w\,i}))} = T_{te} \sum_{i=1}^{n_{Vw}} \frac{f(V_{w\,i})}{L(SF_{\sigma\, lim} \cdot \sigma(V_{w\,i}))} = 1 \tag{6.4}$$

Considering continuous functions, the summation becomes:

$$T_{te} \int_{V_{in}}^{V_{out}} \frac{f(V_w)}{L(SF_{\sigma\, lim} \cdot \sigma(V_w))} dV_w = 1 \tag{6.5}$$

Using the latter equation, the frequency of tether replacement $f_{te} = \frac{1}{T_{te}}$ (1/year) can be found. In this work the creep curve for the $DM20$ material in Figure 6.2a is used.

6.3 Winch

6.3.1 GG-AWES: Winch drum, Line Handling and Winch Bearings

The winch drum is found to be a relevant cost for GG-AWES systems. A good design can avoid the damaging of the tether and elongate its life. The winch should not be too big to

lower the manufacturing cost and to avoid a low generator speed.

The winch cost is proportional to its material mass [54]:

$$C_{Winch} = m_{drum}\, c_{al} \tag{6.6}$$

Assuming that the thickness of the drum is 5% of the diameter and that all the tether is lying on the first layer [54], the mass is:

$$m_{drum} = \frac{\pi \left(D_{drum}^2 - (0.9 \cdot D_{drum})^2\right)}{4} \frac{r\ d}{D_{drum}\pi} \rho_{al} \tag{6.7}$$

Parameter	Mean	SD	Units
D_{drum}/d	50	-	-
c_{al}	1.6	-	€/kg

Table 6.2: Parameters ranges related to the winch drum cost [54].

6.3.2 FG-AWES: Winch drum, Line Handling and Winch Bearings

For a FG-AWES, the cost related to the winch is lower: it does not need to be designed for power production. The winch should be big enough to avoid damaging the tether, but the tether could be stored in many layers, limiting the axial dimension.

The drum mass can be then computed as:

$$m_{drum} = \frac{\pi \left(D_{drum}^2 - (0.9 \cdot D_{drum})^2\right)}{4\ n_{layers}} \frac{r\ d}{D_{drum}\pi} \rho_{al} \tag{6.8}$$

considering $D_{drum}/d = 100$ and $n_{layers} = 4$.

6.4 Electrical system

6.4.1 GG-AWES

The cost function for the generator is estimated from Heilmann [54]. It is proportional to the rated power and it is function of the generator speed:

$$C_{gen} = a_{gen} \cdot P_{rated} \cdot w_{nom}^{b_{gen}} \tag{6.9}$$

with w_{nom} in rpm, P in W.

The power electronics cost can be considered proportional to the rated power [54]:

$$C_{el} = P_{rated} \cdot a_{el} \tag{6.10}$$

With the power expressed in W.

Concerning the take-off sub-system, a power density is considered for the motors (c_{mot}) [17] and the batteries (c_{batt}) [61].

The parameters describing the cost of the electrical system for a GG-AWES are given in Table 6.3.

Parameter	Mean	SD	Units
a_{gen}	1.2	0.2	€/W
b_{gen}	-0.6	-	-
a_{el}	0.09	-	€/W
c_{mot}	90	-	W/€
c_{batt}	0.19	-	€/Wh

Table 6.3: Cost parameters related to the GG-AWES electrical system.

6.4.2 FG-AWES

For FG-AWES, the on-board generators and electronics cost is modelled with the same equations proposed for GG-AWES. However, to take into account an additional cost if the electronic generation is on-board, a factor f_{FG}, ranging from 1.2 to 1.8, is applied to the equivalent GG-AWES cost.

6.5 Launching and landing structure

The launching and landing structure should be designed according to the take-off strategy. In this work two strategies are considered: linear and vertical take-off.

6.5.1 Linear take-off

A linear take-off requires the design of the take-off and landing system. *Ampyx Power* [13] has designed a catapult to launch the kite into the wind. The catapult can rotate on the platform to face the wind. For the landing, the tether pulls the aircraft down on the platform with a patented system. The rail is 20 m long for a 12 m span kite.

Unfortunately, a design driver is not clear for the linear take-off and landing. A meaningful strategy for the cost estimation could be to evaluate the cost of a simple take-off method, assuming that a customized lunching and landing system would reduce the costs. Once a simple method is implemented, a large uncertainty on the model parameters is used to model the many design strategies.

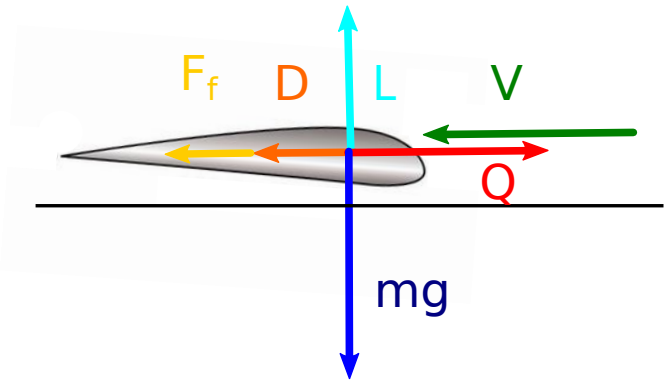

Figure 6.3: Force balance during the acceleration on the strip.

Referring to Figure 6.3, the kite is modelled as a classical aircraft taking off. The thrust Q, needed to accelerate, is given by the on-board propellers used during the climbing. The drag D and the friction force $F_f = \mu(mg - L)$ are acting along the opposite direction. The

equation of motion, assuming a constant thrust Q, is therefore:

$$\begin{aligned} m\dot{v} &= Q - \mu(mg - L) - \frac{1}{2}C_d\rho A v^2 \\ \dot{v} &- Av^2 - B = 0 \end{aligned} \tag{6.11}$$

By setting $v(t = 0) = 0$, the solution of the first order differential equation is:

$$v = \sqrt{\frac{B}{A}}\tan(\sqrt{AB}t) \tag{6.12}$$

The strip length L_s can be found by looking at the distance swept by the kite till the achievement of the stall velocity (velocity for which $L = mg$). The thrust Q is considered 70% of the thrust provided during the climbing phase, μ is set equal to 0.1 [17].

The area on the ground is approximately [18]:

$$A_{g,lin} \simeq \frac{\pi L_s^2}{4} + \frac{\pi s^2}{4} \tag{6.13}$$

6.5.2 Vertical take-off

For vertical take-off, the kite is supported by a static structure holding the kite [14] or it can take off directly from the ground [21]. The initial acceleration is performed by the turbines and/or propellers. The area on the ground is then approximately equivalent to a circle with the diameter equal to the kite span: $A_{g,vert} \simeq \frac{\pi s^2}{4}$.

The cost range of the launching and landing structure is given in Table 6.4. [1]

	Minimum	Maximum	Units
Ground structure p_{Ag}	20	200	€/m^2

Table 6.4: Launching and landing cost per unit area.

6.6 Tower

A tower could be beneficial for AWES [62]. The technical advantages for a tower are:

- Reduction of the tether inclination. Therefore, reduction of the angle between the kite and the wind. The power equation is proportional to the cosine of this angle raised to the power of three, as shown in Eq. (3.88). If the inclination is reduced, more power can be harvest.
- The autonomous take-off and landing manoeuvres could be simplified [62].
- The energy needed to reach the operational altitude is lower [62].
- Wind sensors can be mounted on the tower, to have a better estimation of the shear and of the operational conditions. Moreover, the tower can be used to support other functions, such as antennas [62].

[1] These values are estimated to have an average take-off structure cost equal to approximately 10 % of the total initial capital cost.

- The kite can be used over a forest [62].
- The kite can reach higher operational altitude.

A model for the structural design of the tower can give information also about the costs. Looking at Figure 6.4, some suspensions lines reduce the bending moments on the tower.

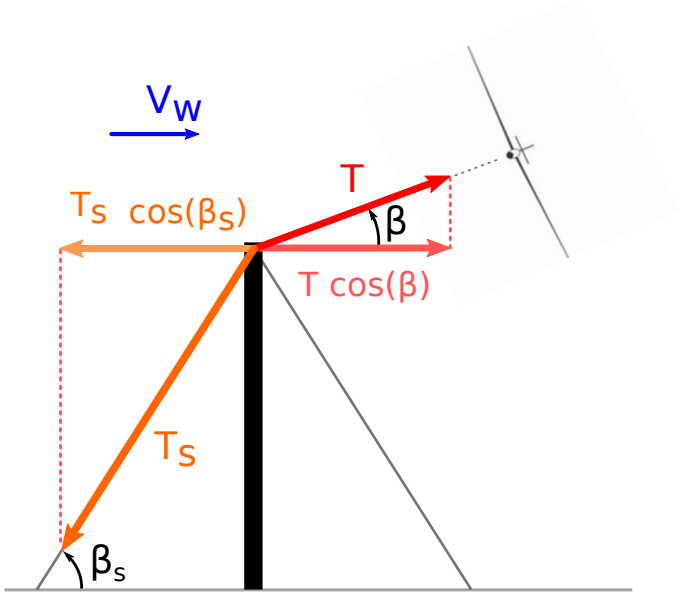

Figure 6.4: Forces acting on the tower and on the suspension lines for a FG-AWES or a GG-AWES with the generator set at the tower top.

As an approximate first design, the tower is considered to absorb only compression forces and not bending moments. A buckling constraint is neglected at this stage. Therefore, the tension force on the suspension lines is [62]:

$$T_s = \frac{T_s \cos(\beta_s)}{\cos(\beta_s)} = \frac{T \cos\beta}{\cos(\beta_s)} \tag{6.14}$$

The compression force acting on the tower is [62]:

$$T_{comp} = T_s \sin\beta_s - T \sin\beta = T(\tan\beta_s \cos\beta - \sin\beta) \tag{6.15}$$

With these two expressions, the tower and the suspension lines can be designed. Assuming a suspension lines inclination of 60°, the lines and the tower cross section should be thick enough to not exceed the material strength. The material of the cables is considered to be steel. The tower could be a truss structure manufactured in aluminium. A truss structure would allow a cost-effective transportation, mounting and disposal.

For a GG-AWES, the design is more complex and could be done in two ways. The first is similar to the FG-AWES design: the winch and the generator are set on the top of the tower. For this design, the tower should withstand an additional torque due to the power generation. It could be a bending moment or a twist, depending on the generator orientation.

If the generator is set at the tower base, a pulley has to change the direction of the tether (Figure 6.5). This is leading to a new force resultant that need to be supported by the tower and the suspension lines.

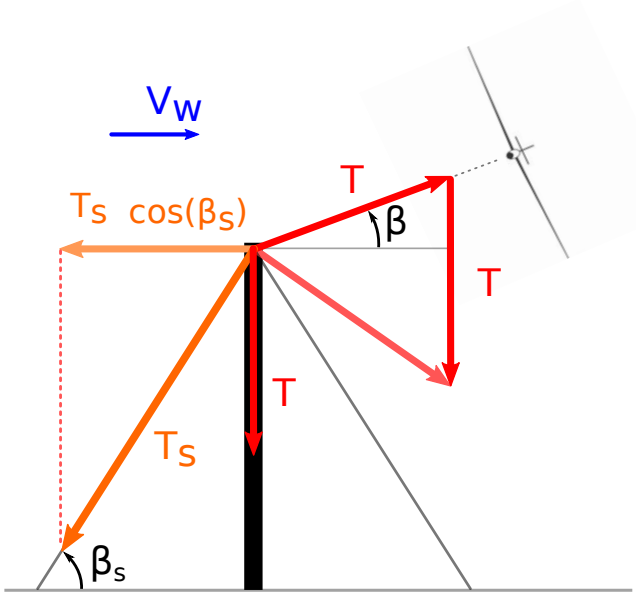

Figure 6.5: Forces acting on the tower and on the suspension lines for a GG-AWES with the generator set at the tower bottom.

In this case, the forces on the suspension lines are the same as in the previous case. The normal force that the tower needs to withstand is:

$$T_{comp} = T_s \sin\beta_s + T(1 - \sin\beta) = T(1 + \tan\beta_s \cos\beta - \sin\beta) \tag{6.16}$$

In this work the generator is suppose to be placed on the tower top.

The price per kg of the suspension lines c_{SL} and of the tower frame c_{tw} are given in Table 6.5. A factor c_t, which multiplies the tower material cost, is used for manufacturing, transportation and installation.

	Mean	SD	Units
c_{SL}	1.5	-	€/kg
c_{tw}	1.6	-	€/kg
	Minimum	Maximum	Units
c_t	1	3	-

Table 6.5: Steel [63] and aluminium prices per kg and manufacturing factor.

6.7 Fixed costs

The fixed costs include all the costs of components not related to the specific system design, such as transformer, cover frame, electrical grid connection, assembly, transport, installation, operation and maintenance and decommissioning. Faggiani [64] proposes cost models for each of these components for a GG-AWES with soft kites. Since these costs are considered the same for all the designs, they are used in this work. The main costs are listed in Table 6.6.

		Units
Transformer [65]	$12'000\left(P_{rated}/10^6\right)^{0.4}$	€
Cover frame [54]	$0.03P_{rated}^{0.8}+3000$	€
Electrical connection [66]	25'000	€
Cable installation	120'000	€
Transport and installation	$0.005P_{rated}$	€
Civil works	5000	€
Units and cable removal	$100'000$	€

Table 6.6: Fixed costs for all the designs [64].

6.8 Operation and maintenance

Typically, operation and maintenance costs constitute a relevant share of the total annual costs of a wind turbine. It is expected to be similar for AWES.

Operation and maintenance costs are related to insurance, regular maintenance, reparation, spare parts and administration. A typical value for wind turbines is about 12 to 15 €/MWh [67].

In this work the operation costs OC (insurance, regular maintenance and administration) are considered to have a mean of 9 €/MWh and a standard deviation of 3 €/MWh.

The maintenance costs (reparation and spare parts) are related to components with a working life. The tether life is estimated with the procedure shown in Section 6.2. A frequency of replacement of the kite $f_{r.\,gl}$ is considered as well. This is to take into account possible crashes.

6.9 Levelized cost of energy (LCOE)

Once all the costs are computed, the initial capital costs ICC and the operational and maintenance costs OMC can be found. The Levelized cost of energy ($LCOE$) is then the ratio between the *annual costs* and the produced energy [66]:

$$LCOE = \frac{ICC \times CRF + OMC}{AEP} \tag{6.17}$$

Where AEP is in MWh/y and OMC in €/y. The capital recovery factor CRF can be expressed as function as the discount rate i:

$$CRF = \frac{i(1+i)^{n_y}}{(1+i)^{n_y}-1} \tag{6.18}$$

where n_y is the number of years of operation.

Chapter 7

Profit maximisation

In this chapter, the cost model is included in the optimisation. Thus, some interesting economics outputs can be analysed. The aim of this investigation is to spot trends that relate the system designs to LCOE.

Initially, the new problem formulation is proposed. Some tests to understand how many optimisation problems are to be run to find a global minimum are carried out. Later, two typical optimisation outputs are shown. The uncertainty quantification include the cost-related uncertainties. Finally, the global sensitivity analysis is performed. Initially, GG-AWES, FG-AWES and systems with both the generation types are analysed. Later, two global sensitivity analyses on GG-AWES and FG-AWES outline the characteristics of the two generation types.

7.1 Problem formulation

The problem formulation is slightly different from the one proposed in Section 5.1. In this case, the cost of the design is considered.

7.1.1 Design variables

To the design variables presented for the AEP maximisation, given in Table 5.1, the tower height q_{ht} in m is added.

7.1.2 Constraint

The constraints are related to the tether strength, the rated power, the minimum operational altitude and to the structural design, as in the previous case. However, no constraint on the wing area is here considered. In this way, the optimiser designs the kite dimensions.

7.1.3 Objective function

The objective function is represented by the annual profit:

$$\Pi = p_{el} \cdot AEP - (ICC \times CRF + OMC) \tag{7.1}$$

Where p_{el} is the price of electricity and the term in the brackets is the annual costs (Eq. (6.17)). This objective function is robust from an optimisation algorithm point of view. The

optimiser tries to maximise AEP and minimise the costs. p_{el}, for the optimiser, represents a weight between revenues ($p_{el} \cdot AEP$) and the costs ($ICC \times CRF + OMC$).

This objective function is preferable compared to LCOE. A minimisation of LCOE is highly dependent on the fix costs, here known with high uncertainty. In this case, the minimum LCOE could be found with small AEP and small costs, leading to not interesting designs.

7.1.4 Optimisation algorithm

A gradient-based optimisation algorithm can still be suitable for this problem, with some considerations. This family of algorithms cannot handle discontinuity in the design space: the cost functions are not always continuous. For instance, some costs are present only if the system has on-board or ground generation. To still use these algorithms, the generation type is chosen before starting the optimisation. Therefore, the generation types can ground generation (GG-AWES), on-board generation (FG-AWES) or both at the same time. After this initial decision, the optimisation problem can be solved. To compare the results, the three generation types should be evaluated.

7.2 Model implementation

The physical model is similar to the one presented in Section 5.2. The only difference is that the tower height is included in the altitude computation.

Once the annual energy production AEP is computed, the cost associated to the design can be evaluated.

7.3 Algorithm validation

Some tests to understand if the problem is well posed can be performed. Moreover, these tests point out how many optimisation problems are to be run to find the global minimum.

7.3.1 Algorithm reliability

To understand how many optimisation problems are to be run to find a global minimum, the test presented in Section 5.3.1 is carried out. The rated power P_{rated} and the electricity price p_{el} are considered two parameters that highly influence the objective function. Thus, they are varied. The objective function should be checked to be a continuous and smooth function of these parameters. Figure 7.1a shows how the objective function varies with P_{rated} and Figure 7.1b with the electricity price p_{el}. To make these plots, 21 optimisation problems are run. Within these 21, 7 are ground generation, 7 fly-generation and 7 have both the generation types. The objective function is considered to be a smooth and continuous function of the selected parameters, according with the scale of the plot.

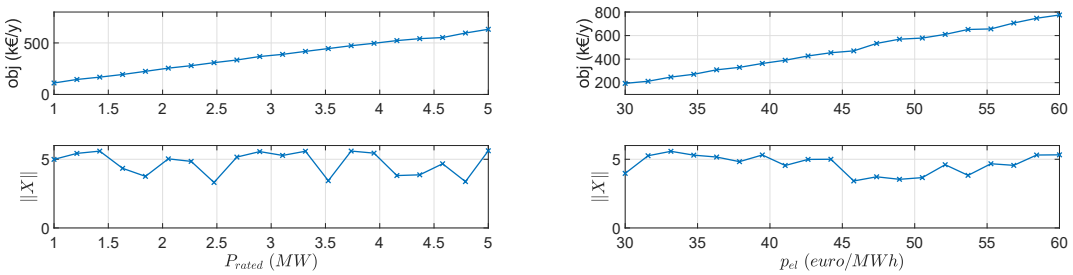

(a) (b)

Figure 7.1: Objective function and norm of the design variables as function of the rated power (a) and of the electricity price (b).

7.3.2 Reference LCOE

To validate the cost model, the finals LCOE is compared with reference values. Drexler in [68] shows the LCOE of the main existing AWES technologies. The LCOE ranges between about 20 to 120 €/MWh. However, this thesis is analysing costs and performances in the future, when the technology will be mature. So, the LCOE is expected to be lower. Ahrens in [9] shows that AWES can have a LCOE ranging between 10 and 20 €/MWh with a mature technology.

7.4 Optimisation results

In this section, two typical results of the optimisation problem are shown. The rated power is set to 2 MW, the maximum lift coefficient to 2. The kite is supposed to have a failure every 10 years and to be replaced. All the other parameters are set to nominal values.

These solutions are not investigated in details because a more informative analysis is presented with a global sensitivity analysis in the next sections.

7.4.1 GG-AWES

Figure 7.2 shows the main outputs for the optimisation of a GG-AWES. The pie chart outlines that most of the initial capital costs are related to electronics. The kite structure and the tether have a low share of the total cost. A span of 32 m and an aspect ratio of 8 combine for a wing area of 128 m^2. However, the total kite mass is low. The low aspect ratio makes the airfoil thickness to be large. Thus, the spar caps are far from each other, increasing the inertia. By looking at the power curve, the rated power is achieved at around 9 m/s. This is leading to a capacity factor of 46 %. On the first plot on the right, the trend of the lift coefficient and of the tether stress can be seen. The tether stress gets close to the limit of 1.5 when the rated power is reached. The operational tether life is 2.4 years. The second plot on the right shows the reel-out coefficient γ_{out} and the additional inclination due to mass Δ. Finally, this system has a LCOE of 16 €/MWh.

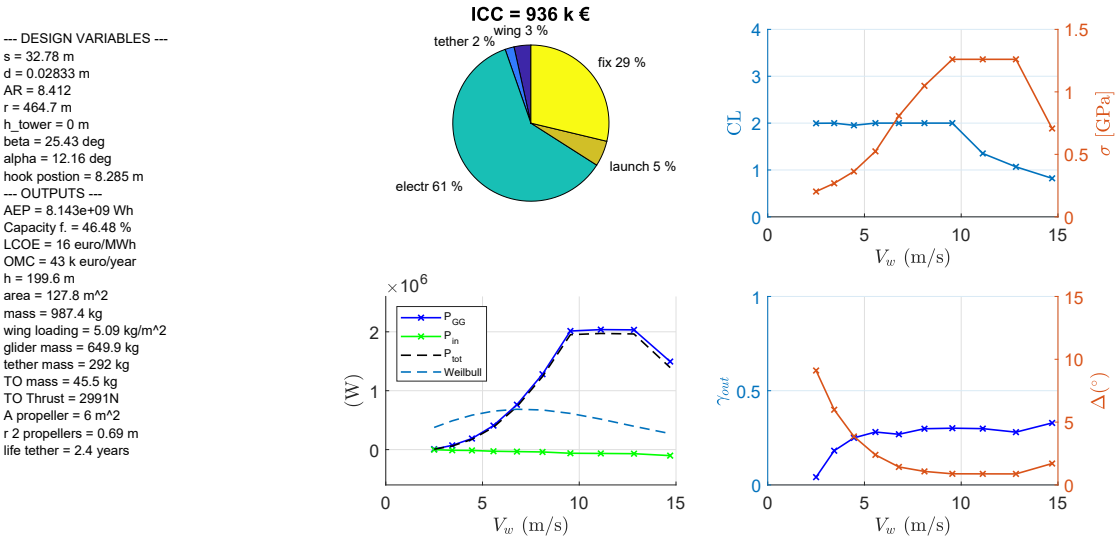

Figure 7.2: Typical trends for a GG-AWES optimised to maximise the profit.

7.4.2 FG-AWES

Figure 7.3 shows typical trends for a FG-AWES. In this case the electronics have a lower cost share, if compared to the GG-AWES case. The Initial Capital Cost (ICC) is lower. A span of 42 m and an aspect ratio of 13 combine for a wing area of 140 m^2. The structure mass (*glider mass* in figure) is higher than for the GG-AWES case. Looking at the power curve, the rated power is reached at around 9 m/s, leading to a capacity factor of 54 %. The first plot on the right shows the lift coefficient and the stress, as function of the wind speed. The stress reaches the maximum when the rated power is attained. This is in accord with the power curve description proposed by Vander Lind [41], explained in Section 5.3.2. The tether has an operational life of 6.3 years. Finally, a LCOE of 17 €/MWh can be obtained with this system.

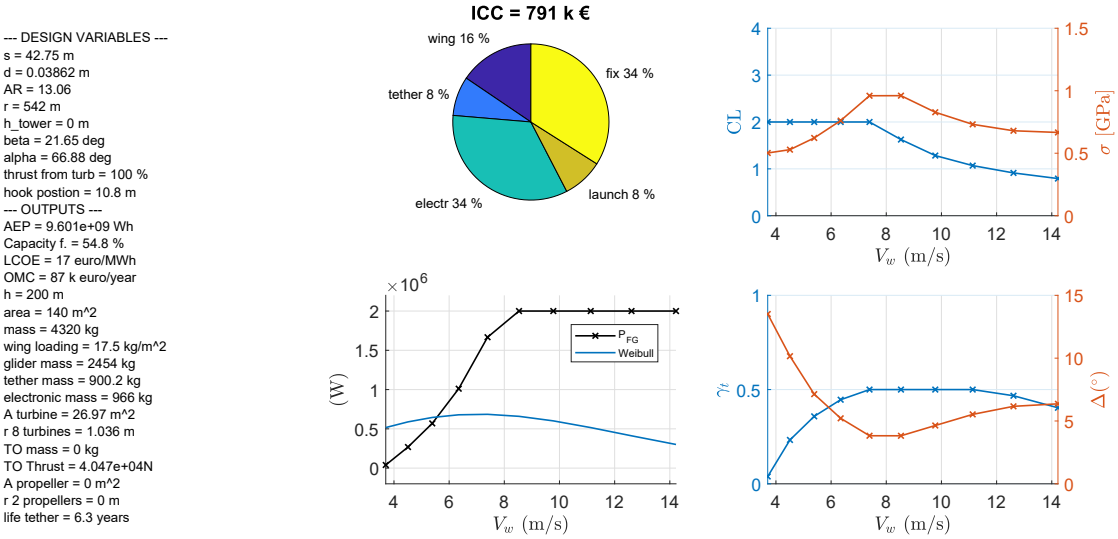

Figure 7.3: Typical trend for a FG-AWES optimised to maximise the profit.

7.5 Uncertainty quantification

In this section, the uncertainty quantification is presented. All the model parameter uncertainties related to the physical model, given in Table 5.4, are considered. To these, the economic related uncertainties are added. These uncertainties are mainly related to the uncertain cost parameters given in the previous chapter. To these cost parameters, the epistemic uncertainties on the rated power, on the number of operational years and on the maximum tower height are added. A frequency of kite replacement is also considered. This is to investigate how the control system failures, and the relate crashes of the kite, impact on the design.

In Table 7.1, the uncertainties, added to ones presented in Table 5.4, are given.

par	Min	Max	Units	Description
p_{wing}	20	200	€/kg	Price per unit mass of the structural material of the aircraft (eq (6.1))
f_{te}	1.2	2	-	Cable manufacturing additional price in case of both structural and electrical components (Table 6.1)
p_{Ag}	20	200	€/m^2	Coefficient for the launch and landing system cost (Table 6.4)
c_t	1	3	-	Coefficient for the manufacturing of the tower (Table 6.5).
$f_{r.\ gl}$	0	0.5	-	Number of aircraft replacement in one year.
f_{FG}	1.2	1.8	-	Factor for the on-board electronic cost (Section 6.4.2).
h_t^{max}	150	250	m	Maximum tower height
n_y	15	25	-	Number of operational years.
P_{rated}	1.5	4.5	MW	Rated power
par	Mean	SD	Units	Description
p_{te}	200	50	€/kg	Price per unit mass of the structural material of the cable (Table 6.1)
a_{el}	1.2	0.2	€/MW	Coefficient for the generator cost (Table 6.3)
C_{fix}	150	80	k€	Fix cost (Table 6.6)
OC	9	3	€/MWh	Operation costs
i	0.09	0.015	-	Discount rate [69]
p_{el}	40	10	€/MWh	Price of electricity [70]

Table 7.1: Model parameters ranges and descriptions for the economic analysis. The first parameters group has a uniform distribution, the second a Gaussian.

7.6 Global sensitivity analysis

The global sensitivity analysis is now considered, using the procedure explained in Section 4.3.4.

7.6.1 Evaluation procedure

A number of evaluations of the optimisation problem (*computational model* in Figure 4.4) has to be performed. These evaluations are taken in points filling the model parameter space.

In Figure 7.4, the process for the evaluation is presented. In Section 7.5, the model parameters that could be design drivers are selected and an uncertainty is given. Using the *Latin hypercube sampling* technique, a number *Nsample* of inputs are generated. Each input is a set of model parameters and, if a parallel computing approach is used, is sent to a worker. Each worker has then to find the global maximum, given the problem with the selected model parameters. To find the global maximum, a number *N_max* of optimisation

problems, with different random initial conditions, has to converge for each generation type. Finally, the global maximum for each input is considered to be the best of the $3 \times N\_max$ converged optimisation problems.

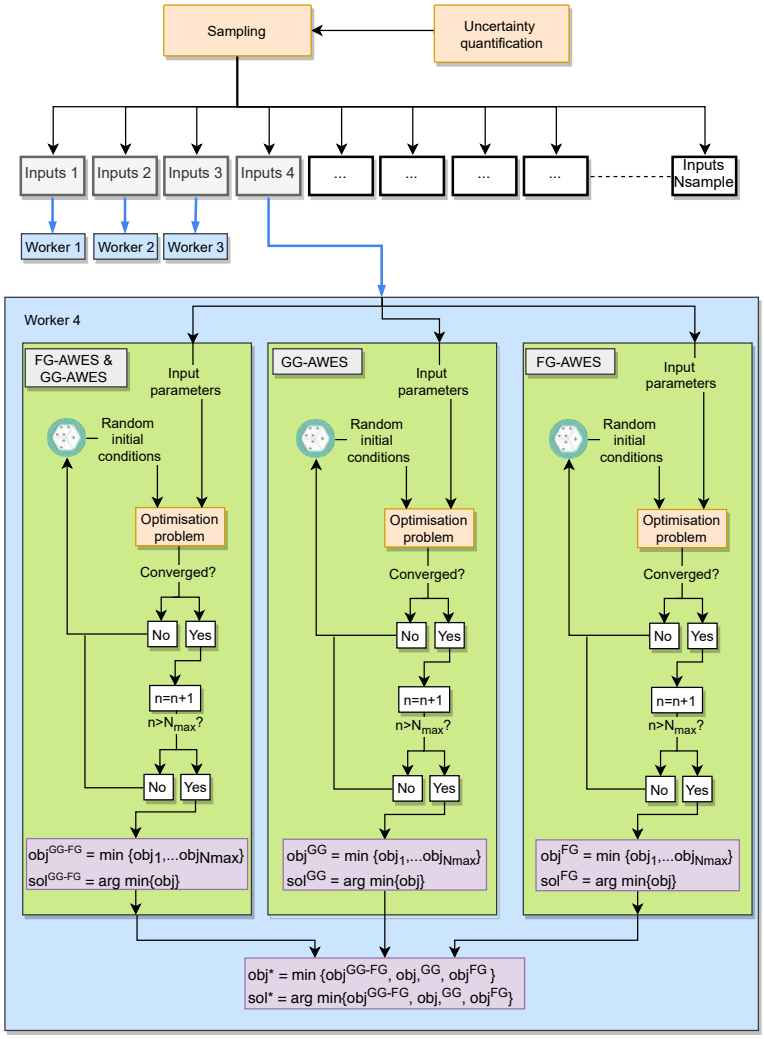

Figure 7.4: Flowchart of global sensitivity for profits maximisation.

7.6.2 Output parameters

To describe the solution from a physical and economical point of view, additional outputs to the one presented in Section 5.7.2 are considered. These are:

Π : Annual profit

$LCOE$: Levelized cost of energy

$f_{r.\,te}$: Frequency of tether replacement

A_{kite} : Wing area. In the AEP maximisation case it was a model parameter, here it is an output.

h_t : Tower height

A_g : Ground area needed to take-off.

λ_{ht} : Lagrange multiplier of the maximum tower height.

ICC : Initial Capital Cost

OMC : Operation and Maintenance Cost

$cost_{kite}$: Kite structure cost

$cost_{te}$: Tether cost

$cost_{el}$: Electronics cost

$cost_{TOs}$: Take-off structure cost

$cost_t$: Tower cost

7.7 Global sensitivity analysis results

Once the uncertainties and the outputs are defined, the global sensitivity analysis can be performed, following the methods explained in Section 4.3. The wind resources are fixed to the nominal values for this case.

2400 points (i.e. $Nsample = 2400$ in Figure 7.4) are considered a sufficient number to have a good representation of the model parameter space and to build a metamodel. Each of these points is the best (in term of objective function) of 21 converged optimisation problems run with random initial conditions (i.e. $N\_max = 7$ in Figure 7.4), in accord with the results of Section 7.3.1.

7.7.1 Statistics of design outputs

Initially, a statistical approach to analyse the outputs is performed. Thus, the mean and standard deviation of the outputs are given in Table 7.2.

	Π	$LCOE$	CF	AEP	m_{tot}	m_{gl}	m_{el}	m_{te}	m_{TO}
units	k€	€/MWh	-	GWh	kg	kg	kg	kg	kg
mean	439	19.75	0.8	20.9	1649	672	50	878	50
SD	270	3.39	0.1	6.46	925	468	145	442	62
	r	d	$f_{r.te}$	h	h_t	β	V_{in}	V_{out}	A_{kite}
units	m	mm	1/year	m	m	°	m/s	m/s	m^2
mean	426	50	0.09	209.24	0.52	29.42	1.86	18.96	149.4
SD	84	10	0.07	37.34	5.56	1.44	0.82	0.98	99.53
	AR	s	B	δ_{out}	δ_{in}	A_{turb}	Q_{turb}	α_{TO}	Q
units	-	m	m	m	m	m^2	-	°	kN
mean	8.73	33.13	7.99	0.26	0.82	45.2	0.21	35.09	10
SD	2.87	8.79	2.17	0.41	0.39	115.41	0.4	30.52	9
	A_g	E_{TO}	A_{prop}	λ_{te}	λ_{Prated}	λ_M	$\lambda_{\delta out}$	$\lambda_{\delta in}$	λ_{CL}
units	m^2	kWh	m^2	k€/-	k€/-	k€/-	k€/-	k€/-	k€/-
mean	941.1	5	6.68	0	834	23.7	0.6	1.5	15.3
SD	516.24	3	6.58	0.3	563	21.2	3.4	6.6	32.4
	λ_{hmin}	λ_{ht}	ICC	OMC	$cost_{kite}$	$cost_{te}$	$cost_{el}$	$cost_{TOs}$	$cost_t$
units	k€/-	k€/-	k€	k€	k€	k€	k€	k€	k€
mean	19.7	0	1711	221	68	194	1159	121	0
SD	54.2	0	576	93	52	122	466	73	5

Table 7.2: Mean and standard deviation of the outputs for the profit maximisation case with fixed wind resources.

Design performance

The performance is the objective function of the optimisation problem: the profit Π. The mean value is 439 k€ per year. The standard deviation highlights that Π is generally positive: AWES are interesting from a investors point of view, without any incentives.

Design outputs

The design outputs describe the average solution. The LCOE is found to be really low, with a small standard deviation. This outlines that it is generally possible to have small cost of energy, in accord with the reference values given in Section 7.3.2. Interestingly, the capacity factor is really high, with a relative small standard deviation. This means that a power curve with a small rated wind speed is economically attractive.

The masses have high variances. They are expected to vary with the rated power. The operational altitude is low. The tether is replaced on average every 10 year, but the variance is high. The elevation angle β has a value similar to the average of the AEP maximisation case. Moreover, the variance is small, outlining that this value can be fixed in future designs and studies. The average cut-in wind speed is low: this is to increase the operational wind speed range and the capacity factor. The aspect ratio is smaller than the one for the AEP maximisation. A smaller AR makes the chord larger and the wing thicker. In this way, the weight reduces. The variables related to the take-off have high uncertainties, showing that no take-off strategy is, on average, preferable. All the variables related to the tower are small, highlighting that building a tower is not convenient from an economic point of view.

Finally, the costs can be analysed. By looking at the component costs, the most expensive sub-system is the electronic sub-system with more than 1 million euro on average. The tether and the take-off structure follow. Interestingly, the cheapest sub-system is the kite structure.

Constraints

The Lagrange multipliers of the constraints give an overview of the constraints strength. They are normalized with the constraint limit themselves to make a comparison possible. Clearly, the constraint limiting the most the objective function Π is the rated power. However, it has a big standard deviation.

The constraints on the structural material strength λ_M, on the minimum operational altitude λ_{hmin} and on the maximum lift coefficient λ_{CL} have similar magnitude between each other. They also have high standard deviation. Therefore, a detailed investigation is necessary.

The Lagrange multiplier on the tether strength is small, showing that this constraint is weak. The material strength is not driving the design of the tether, the creep life is. Finally, the Lagrange multipliers on the structure displacement are small. The structural design is indeed driven by the structural material strength.

7.7.2 Sobol analysis and design trends

The Sobol' indices are now analysed. In Appendix B.1 the visual representation of the Sobol' indices is given. The variance of the profit Π is mainly influenced by the rated power and by the electricity price. The variance of LCOE is highly sensitive to the operation costs OC variance. In order to visualize a high number of evaluations, a density plot can help to understand where most of the points are. In Figure 7.5a, the evaluations density highlights the dependence between LCOE and OC.

The capacity factor variance is highly influenced by the price of electricity variance. In Figure 7.5b this dependence is shown. Interestingly, when the electricity price is low, some evaluations show a low capacity factor. In this case, the profit cannot be positive and the optimiser looks for minimising the costs.

It is now interesting to understand which generation type the optimiser chooses to maximise the profit. Figure 7.6a shows the evaluations for the LCOE as function of the frequency of replacement of the kite, highlighting the generation type chosen by the optimiser. If the kite is not replaced at all or less than once in 10 year, FG-AWES seems to be convenient from a cost prospective. If the kite needs to be replaced more often, GG-AWES is preferable. This is related to the cost of the flying mass that needs to be replaced after a crash. Figure

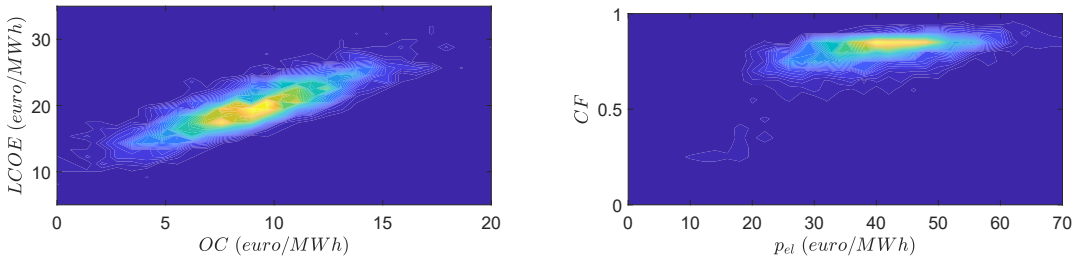

(a) (b)

Figure 7.5: Density plot of the LCOE as function of the operation costs (a) and CF as function of the electricity price (b).

7.6b shows the evaluations of the flying mass cost. The costs, which are needed to be paid after a crash, are much higher for a FG-AWES compared to a GG-AWES.

In accord with this analysis, GG-AWES and FG-AWES are expected to have different designs. Therefore, a global sensitivity analysis, considering one single generation type, is carried out in Section 7.9 and 7.10. First, a investigation on how the wind resources influence the design is performed.

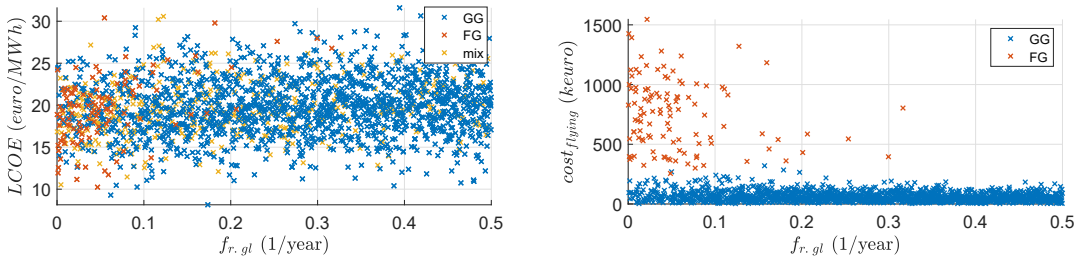

(a) (b)

Figure 7.6: Evaluations of LCOE (a) and of cost of the flying mass (b) as function of the frequency of kite replacement.

7.8 Global sensitivity analysis results considering wind resources uncertainties

To understand in which way the wind resources influence the design, a sensitivity analysis including them is carried out. The ranges for the wind shear α and the Weibull parameters is given in Table 5.7.

The statistics of the outputs are given in Table 7.3. Interestingly, the average and the standard deviation of the outputs look similar to the ones presented in Table 7.2. The standard deviation of the cut-out wind speed has a larger magnitude: to have high capacity factor the power curve terminates when the Weibull distribution goes to zero.

In Appendix B.2, the Sobol' indices for this case are given. The wind resource uncertainties have an influence on the design and on the LCOE. In Figure 7.7a the metamodel, used for the Sobol' indices evaluation, is used to show how LCOE varies with the scale parameter A and the operation costs OC. Clearly, with higher wind speed and lower operation costs, LCOE is lower. However, a low LCOE can be obtained also in low wind speed regions. Figure 7.7b shows how the wing area varies with the maximum lift coefficient and the

	Π	$LCOE$	CF	AEP	m_{tot}	m_{gl}	m_{el}	m_{te}	m_{TO}
units	k€	€/MWh	-	GWh	kg	kg	kg	kg	kg
mean	425	20	0.77	20.2	1550	631	41	830	48
SD	270	4.19	0.14	6.83	907	472	139	427	54
	r	d	$f_{r.te}$	h	h_t	β	V_{in}	V_{out}	A_{kite}
units	m	mm	1/year	m	m	°	m/s	m/s	m^2
mean	432.21	47.9	0.1	213.13	0.35	29.56	2	22.41	144.56
SD	86.29	10.6	0.07	40.96	5.02	1.16	0.86	5.98	116.25
	AR	s	B	δ_{out}	δ_{in}	A_{turb}	Q_{turb}	α_{TO}	Q
units	-	m	m	m	m	m^2	-	°	kN
mean	8.78	32.37	7.79	0.25	0.82	36.3	0.16	32.79	9
SD	2.77	9.86	2.38	0.36	0.39	110.35	0.36	29.68	8
	A_g	E_{TO}	A_{prop}	λ_{te}	λ_{Prated}	λ_M	$\lambda_{\delta out}$	$\lambda_{\delta in}$	λ_{CL}
units	m^2	kWh	m^2	k€/-	k€/-	k€/-	k€/-	k€/-	k€/-
mean	917.85	5	6.56	0.8	945.8	22.2	0.4	1.2	19.4
SD	595.69	3	7.58	21.2	696.5	21	1.8	3.8	124.8
	λ_{hmin}	λ_{ht}	ICC	OMC	$cost_{kite}$	$cost_{te}$	$cost_{el}$	$cost_{TOs}$	$cost_t$
units	k€/-	k€/-	k€	k€	k€	k€	k€	k€	k€
mean	20.3	0.3	1663	213	64	180	1134	117	0
SD	67.7	9.6	585	93	52	114	460	74	4

Table 7.3: Mean and standard deviation of the outputs for the profit maximisation case including wind resources.

Weibull scale parameter. For low A a big area is optimal. In this region, a high lift coefficient is beneficial to reduce the kite area. With an increase of the scale parameter, smaller wing areas are optimum, from a cost point of view. Thus, depending on the wind resources, the kite size can vary. However, the aspect ratio is not influenced by the wind resources. This information is elaborated in the next two sections.

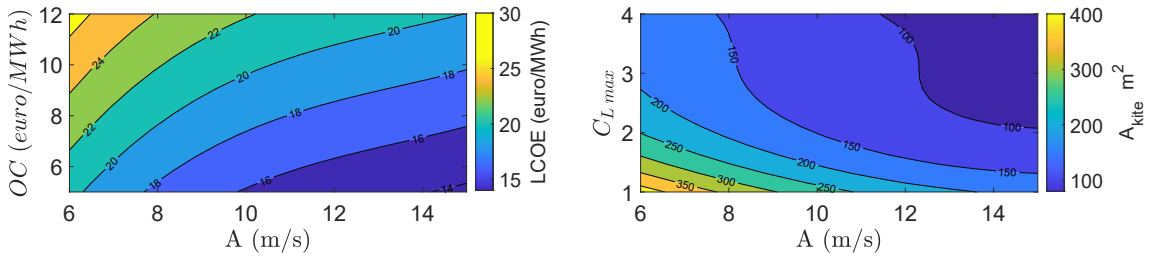

(a) (b)

Figure 7.7: Contour plot of the metamodel of LCOE as function of the Weibull scale parameter and the operation costs (a) and of the wing area as function of the Weibull scale parameter and the maximum lift coefficient (b).

7.9 Global sensitivity analysis results for GG-AWES

In this section, the results of a global sensitivity analysis, carried out on a GG-AWES, are presented. The rated power is fixed to 3 MW, the frequency of kite replacement ranges from $f_{r.gl} = 0$ to $f_{r.gl} = 0.1$ 1/year. The wind resources uncertainties are considered in this analysis.

7.9.1 Statistics of design outputs

In Table 7.4 the statistics of the evaluations are given.

	Π	$LCOE$	CF	AEP	m_{tot}	m_{gl}	m_{el}	m_{te}	m_{TO}
units	k€	€/MWh	-	GWh	kg	kg	kg	kg	kg
mean	438	19.58	0.78	20.4	1614	724	0	813	77
SD	243	4.01	0.13	3.52	660	412	0	302	68
	r	d	$f_{r.te}$	h	h_t	β	V_{in}	V_{out}	A_{kite}
units	m	mm	1/year	m	m	°	m/s	m/s	m^2
mean	430	48.6	0.11	212	0.3	29.6	2	22.28	142
SD	91	7.8	0.08	42	4.0	1.23	0.83	6.02	101
	AR	s	B	δ_{out}	δ_{in}	A_{turb}	Q_{turb}	α_{TO}	Q
units	-	m	m	m	m	m^2	-	°	kN
mean	9.39	33.5	8.09	0.36	0.89	0	0	33.44	9
SD	2.81	9.75	2.35	0.42	0.43	0	0	28.04	5
	A_g	E_{TO}	A_{prop}	λ_{te}	λ_{Prated}	λ_M	$\lambda_{\delta out}$	$\lambda_{\delta in}$	λ_{CL}
units	m^2	kWh	m^2	k€/-	k€/-	k€/-	k€/-	k€/-	k€/-
mean	982	6	7.08	0.3	958.2	15.4	0.5	1.1	18.9
SD	585	4	6.43	5.3	615.3	12.5	2.2	3.6	45.5
	λ_{hmin}	λ_{ht}	ICC	OMC	$cost_{kite}$	$cost_{te}$	$cost_{el}$	$cost_{TOs}$	$cost_t$
units	k€/-	k€/-	k€	k€	k€	k€	k€	k€	k€
mean	18.5	0	1737	202	75	163	1207	124	0
SD	29.1	0	374	68	52	74	255	75	3

Table 7.4: Mean and standard deviation of the outputs for GG-AWES.

Design performance

The system has a positive profit, meaning that a GG-AWES can be convenient from an investor point of view, without any incentives.

Design outputs

The LCOE is small, with a relative small variance. The optimal capacity factors are high. The power curve has then a small rated wind speed. The masses have still high uncertainties: a detailed study on what is driving the structural design is needed. The average frequency of tether replacement $f_{r.te}$ is of 0.11, meaning that the tether is replaced every about 10 years. However, the standard deviation is large. The operational altitude is still low. To build a tower is not convenient, from an economic point of view. The elevation angle is with small standard deviation. The kite area is high, with high uncertainty. The aspect ratio is low compared to typical glider values, but of the same magnitude of civil aircraft [71]. The statistics of the take-off climbing angle show that no strategy is generally preferable, from an economic point of view. Figure 7.8 shows the cost breakdown of the initial capital cost. The highest cost is due to the electronics, followed by the tether and the take-off structure costs. The kite structure is generally low.

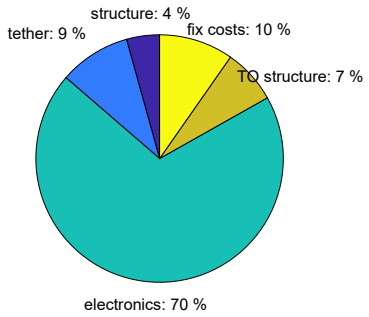

Figure 7.8: Cost breakdown of GG-AWES.

Constraints

The highest Lagrange multiplier is on the rated power. The others are almost two orders of magnitude smaller. The mean of the Lagrange multiplier on the structural material strength λ_M is higher compared to the deflection multipliers. Therefore, the structural design is driven by the material strength. The Lagrange multiplier on the maximum lift coefficient and on the minimum operational altitude present a high standard deviation: a detailed study is then necessary. The Lagrange multipliers on the tether strength and on the maximum tower height are small, showing that these constraints are weak.

7.9.2 Sobol analysis and design trends

The visual representation of the total Sobol' indices is given in Appendix B.3.

The profit Π is highly influenced by the electricity price. The operational costs and the wind resources follow. This is an important finding for policy makers. To finance the significant research and development of AWES, investors want high expectation of profit, with low risk. Thus, policy makers could make sure that a minimum price of electricity will be paid for green energy produced by AWES. In this way, investors are sure to have high profits, with a mature technology. Investors should also notice that high capacity factors imply power generation with low wind conditions. In countries where wind energy have a big share of the energy market, the hours with low wind speeds have a high electricity price. Thus, power fed into the grid in these hours is really profitable.

LCOE is, as in the previous section, influenced by the the operation costs OC and the wind resources. The capacity factor CF variance is mainly influenced by the electricity price and by the Weibull form parameter k. In Figure 7.9a, this dependence is shown. Extremely high capacity factors are optimum in regions with high Weibull form parameter and high electricity price.

The frequency of tether replacement variance is highly influenced by the tether material cost variance. Figure 7.9b shows the evaluation density of this dependence. Two clusters can be identified. Some optima designs have a tether frequency of replacement close to zero, meaning that the tether has a higher life than the operation system lifetime. Others have a higher frequency of replacement. In this cluster, the tether life ranges from about 5 to 20 years.

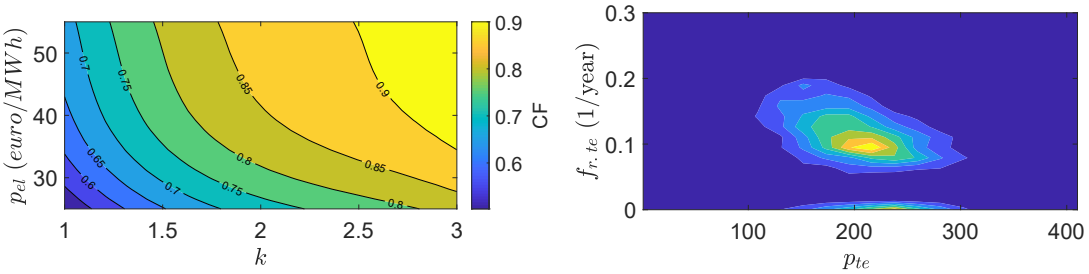

(a) (b)

Figure 7.9: Contour plot of the metamodel of CF as function of the Weibull form parameter and the electricity price (a). Density plot of the tether replacement frequency as function of the tether material cost (b).

The kite dimensions are highly influenced by the Weibull form parameter and the maximum lift coefficient. Figure 7.10a shows the metamodel of the wing area, as function of the scale

parameter and the maximum lift coefficient. Similar considerations to the one given for Figure 7.7b can be drawn. For low A, a high lift coefficient is beneficial to reduce the wing area.

The aspect ratio variance is influenced by $C_{L\,max}$, Cd_0 and by the structural material density ρ_{carb}. Figure 7.10b shows the metamodel of AR as function of Cd_0 and $C_{L\,max}$. Higher aspect ratios are optimal, if high maximum lift coefficients are used. For low value of $C_{L\,max}$, Cd_0 is almost not influencing AR, while for higher $C_{L\,max}$ it is. For the AEP maximisation, the aspect ratio design is driven by the structural deflection constraint. For the profit maximisation, it is driven by the material strength (see average Lagrange multiplier). Thus, for different optimisation problem, different constraints are strong.

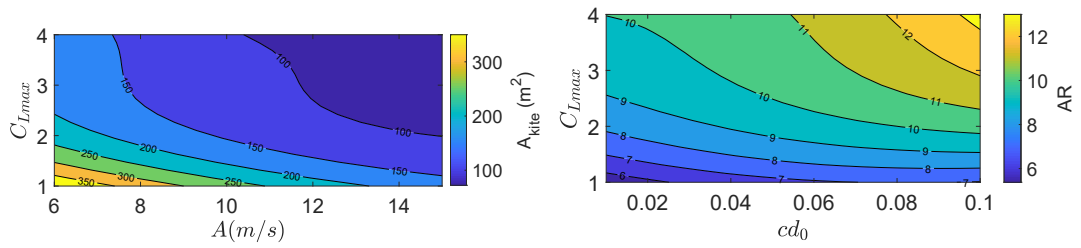

(a) (b)

Figure 7.10: Contour plot of the metamodel of the wing area as function of the Weibull scale parameter and the maximum lift coefficient (a) and of AR as function of the drag coefficient at zero lift and the maximum lift coefficient (b).

The variables related to the take-off do not show any clear dependence. No take-off strategy is then optimum from an economic perspective, according to these analysis.

The constraint on the rated power is the strongest. The Lagrange multiplier of this limit mainly depends on the Weibull scale parameter and on the electricity price variance. Figure 7.11a shows this dependence. For high Weibull scale parameters and high electricity prices, an increase in the rated power is more and more beneficial for the profit. The variance of the Lagrange multiplier on the structural material strength λ_M depends on many parameter, while the Lagrange multipliers on the structure deflections λ_δ depend on the maximum allowed deflection. The Lagrange multiplier on the maximum lift coefficient λ_{CL} depends on many parameters, but mainly on $C_{L\,max}$ and Cd_0. Figure 7.11b shows this dependence. The constraint on the maximum lift coefficient is strong when Cd_0 is high and $C_{L\,max}$ is low. For high $C_{L\,max}$ it is generally weak. In general, high lift coefficient are not highly beneficial for the profit. This is in accord with the finding for the AEP maximisation case.

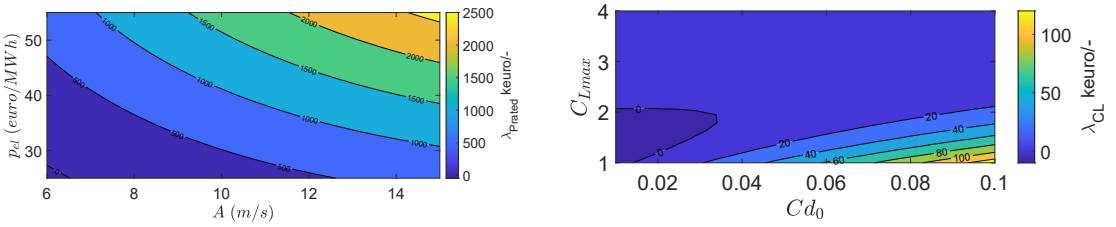

(a) (b)

Figure 7.11: Contour plot of the metamodel of the Lagrange multiplier on the rated power as function of the Weibull scale parameter and the electricity price (a) and of the Lagrange multiplier on the maximum lift coefficient as function of the drag coefficient at zero lift and the maximum lift coefficient (b).

7.10 Global sensitivity analysis results for FG-AWES

In this section, the optimisation of a FG-AWES with respect of the profit is shown. The rated power is fixed to 3 MW, the frequency of kite replacement ranges from $f_{r.gl} = 0$ to $f_{r.gl} = 0.1$ (1/year). This is to study the range where a FG-AWES can be convenient. The wind resources uncertainties are considered in this analysis.

7.10.1 Statistics of design outputs

In Table 7.5 the statistics of the evaluations are listed.

	Π	$LCOE$	CF	AEP	m_{tot}	m_{gl}	m_{el}	m_{te}	m_{TO}
units	k€	€/MWh	-	GWh	kg	kg	kg	kg	kg
mean	411	19.9	0.72	19	3375	1216	483	1627	49
SD	248	4.52	0.16	4.19	1249	790	289	590	106
	r	d	$f_{r.te}$	h	h_t	β	V_{in}	V_{out}	A_{kite}
units	m	mm	1/year	m	m	°	m/s	m/s	m^2
mean	433	64.4	0.01	208	2.46	28.6	2.68	21.51	153
SD	92	10.5	0.04	37	11.22	2.38	1.02	5.92	145
	AR	s	B	δ_{out}	δ_{in}	A_{turb}	Q_{turb}	α_{TO}	Q
units	-	m	m	m	m	m^2	-	°	kN
mean	9.7	33.82	8.26	0.42	0.86	251	0.8	56.49	27
SD	3.5	11	2.77	0.57	0.52	194	0.33	26.48	13
	A_g	E_{TO}	A_{prop}	λ_{te}	λ_{Prated}	λ_M	$\lambda_{\delta out}$	$\lambda_{\delta in}$	λ_{CL}
units	m^2	kWh	m^2	k€/-	k€/-	k€/-	k€/-	k€/-	k€/-
mean	1031	7	1.91	1.5	862.4	21.6	1.2	2.3	24
SD	708.56	4	5.64	12.1	604.2	20.3	4.3	7	44.2
	λ_{hmin}	λ_{ht}	ICC	OMC	$cost_{kite}$	$cost_{te}$	$cost_{el}$	$cost_{TOs}$	$cost_t$
units	k€/-	k€/-	k€	k€	k€	k€	k€	k€	k€
mean	50.8	0	1441	209	119	426	594	130	2
SD	126.9	0	324	73	78	180	102	94	11

Table 7.5: Mean and standard deviation of the outputs for FG-AWES.

Design performance

FG-AWES have generally positive profit, meaning that these systems can be economically attractive and be cost competitive without any incentives.

Design outputs

LCOE is small, similar to the one found for GG-AWES. However the average capacity factor is slightly lower. The total mass is, on average, about the double of the total mass of a GG-AWES. The tether is designed to infinite life. The operational altitude is low. No tower is needed from an economic perspective. The average elevation is slightly smaller than for GG-AWES. The wing area is high, with high standard deviation. The aspect ratio is similar to civil aircraft values [71]. The take-off variables shows that often all the thrust needed to take-off is provided by onboard turbines ($Q_{turb} = 0.8$), but in some cases additional propellers are required. Also the climbing angle α_{TO} shows that not always a vertical take-off is convenient. However, when analysing results related to the take-off, one should consider the simplistic cost model. Finally, the cost breakdown is shown in Figure 7.12. The electronics and the tether have the biggest share on the *initial capital cost*.

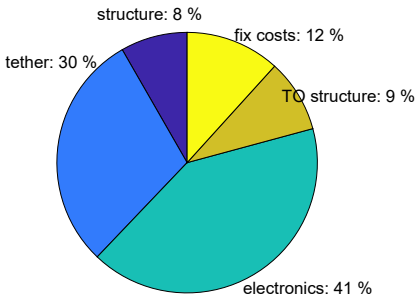

Figure 7.12: Cost breakdown of FG-AWES.

Constraints

The rated power is the strongest constraint. The constraints on the minimum operational altitude, on the maximum lift coefficient and on the material strength follow.

7.10.2 Sobol analysis and design trends

The visual representation of the Sobol' indices is given in Appendix B.4. The profit is mainly influenced by the electricity price, the operation costs and the wind resources. LCOE is mainly influenced by the operation costs OC and the wind resources. The capacity factor CF is mainly influenced by the electricity price and by the Weibull scale parameter k.

Similar considerations to the ones presented for the GG-AWES can be drawn. Policy makers and investors could be interested in the high profits given by a mature technology.

Figure 7.13a shows how the structural mass varies with the price per kg of the structural material and the electricity price. For cheap materials and high electricity prices the optimal designs are with higher mass. This figure is pointing out that, if cheap materials are used in the manufacturing of a kite, the optimal mass increases. However, in this thesis the material properties are not related to the material costs. Thus, an accurate structural design and material cost model could show different trends.

The geometry is influenced by the aerodynamic coefficients, the price of the structural material and the electricity price. Figure 7.13b shows how the wing area is influenced by the drag coefficient and by the maximum lift coefficient. For small Cd_0 and low $C_{L\,max}$, the optimal wing area is way smaller than for high Cd_0. This figures is showing that, when designing a kite for a given rated power, the wing area and the aerodynamics should be designed at the same time.

Figure 7.14a shows how the aspect ratio is influenced by the price of the structural material p_{wing} and by $C_{L\,max}$. AR increases with a cheaper material and for high $C_{L\,max}$. For the AEP maximisation, the average of the optimal AR over the model parameter space is 22 (Table 5.6). Figure 7.14a outlines that, if the structural material cost is low, the optimal designs are going towards the optimal designs for the AEP maximisation. This analysis shows that a high aspect ratio is, on average, not convenient from a cost point of view. Considering that for GG-AWES similar results are found, researches could focus on optimisation of high aspect ratio kites, to make them also economically attractive.

Figure 7.14b shows how the radius of one onboard turbine varies with the Weibull scale

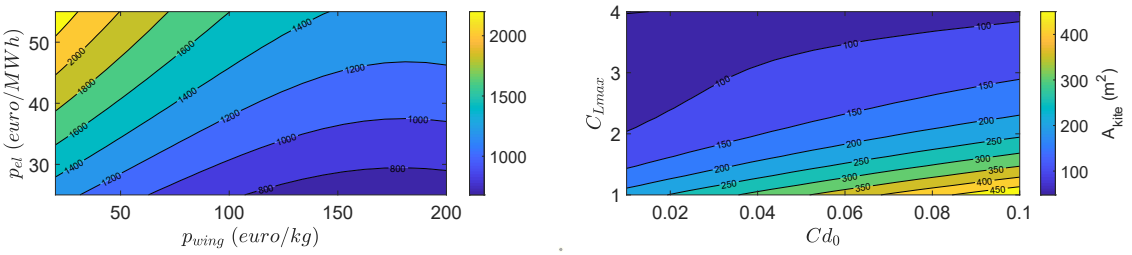

(a) (b)

Figure 7.13: Contour plot of the metamodel of structural mass m_{gl} as function of the structural material price and the electricity price (a). Contour plot of the metamodel of wing area as function of the drag coefficient at zero lift and the maximum lift coefficient (b).

parameter and the minimum efficiency due to disc theory. The radius of the wind turbines is computed with the assumption of 8 onboard turbines. η_d^{min} gives an indication on the losses due to disc theory. If $\eta_d^{min} = 0.8$, a maximum power loss of 20 % due to disc theory is considered for the turbines design. For high η_d^{min}, the wind turbines size increases. For low η_d^{min} and high A, the size decreases. However, low η_d^{min} implies high losses due to disc theory. Referring to the Sobol' indices, the variance of η_d^{min} is not influencing the variance of Π, $LCOE$ and CF. This means that low η_d^{min} can be chosen and the main economics outputs are not influenced. Hence, if the designer wants small onboard turbines, he can perform a kite design with low η_d^{min}, still having the same cost of energy.

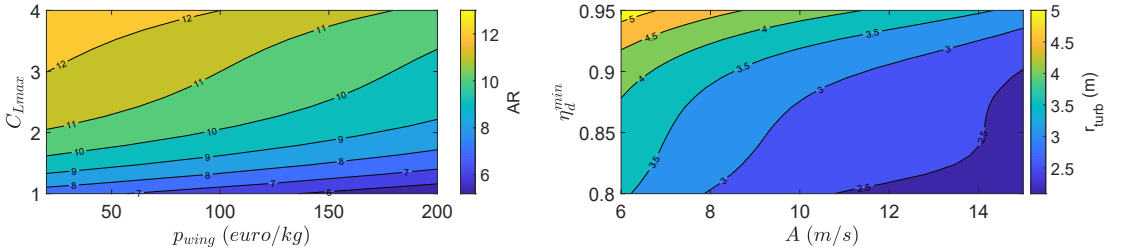

(a) (b)

Figure 7.14: Contour plot of the metamodel of the aspect ratio as function of the structural material price and the maximum lift coefficient (a) and of the turbines radius as function of the Weibull scale parameter and the minimum disc theory efficiency (b).

Finally, the Lagrange multipliers are analysed. The Lagrange multiplier on the minimum operational altitude λ_{hmin} is influenced by h_{min} and the wind shear. Figure 7.15a shows this relationship. The constraint is stronger when the limit itself is high and for low wind shear. If a regulation will impose a minimum operational altitude, kites placed in regions with low wind shears will be penalised more than kite in high shear regions.

λ_{CL} has a high dependence with $C_{L\,max}$. It can be interesting to see how λ_{CL} varies with the structural material density ρ_{carb}. A low structural material density models aircraft with low mass, such as multi-planes. Figure 7.15b shows how λ_{CL} varies with $C_{L\,max}$ and ρ_{carb}. As highlighted by the Sobol' indices, the variance of ρ_{carb} does not influence strongly λ_{CL}. Interestingly, for high material density, representing standard aircraft design, λ_{CL} is higher than for low densities. This means that a standard aircraft needs higher $C_{L\,max}$ than a multi-plane aircraft.

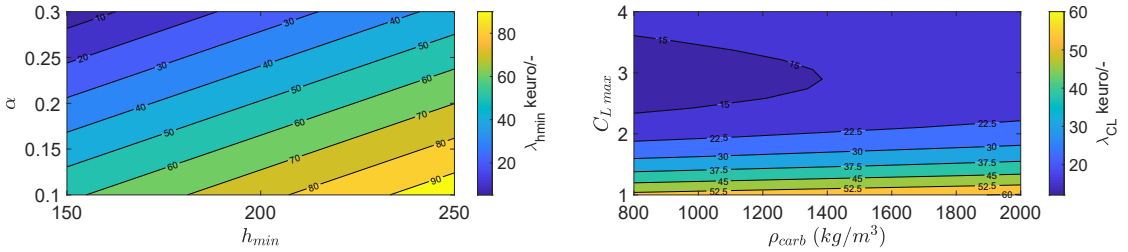

(a) (b)

Figure 7.15: Contour plot of the metamodel of the Lagrange multiplier on the minimum operational altitude as function of the minimum operational altitude and the wind shear (a) and of the Lagrange multiplier on maximum lift coefficient as function of the structural material density and the maximum lift coefficient (b).

7.11 Discussion

In this chapter, a detailed analysis of the optimal designs, with respect to the profit, is presented.

First, the optimisation problem formulation is described. The optimiser performs a kite design to maximise the profit. Two typical optimisation results are shown. How the physical and economic uncertainties influence the design is investigated with a global sensitivity analysis.

Three generation types (GG-AWES, FG-AWES and both at the same time) are considered at a first stage. If the kite control system is reliable, a FG-AWES is convenient. However, these results are based on an approximate cost model. The electronics cost for FG-AWES is indeed found to be lower than for GG-AWES. This is because the on-board electrical generators spin faster than the generator on the ground. More studies could be needed for the cost modelling of the on-board electronics. If the kite needs to be replaced often, a GG-AWES is preferable. In this case, kites should be designed to be really cheap. Investors are attracted from low rick projects. With the assumption that the first commercial AWESs will not have a control system fully reliable, investors could be more interested in GG-AWES, to lower the consequences of frequent failures.

For high kite replacement frequency, the kite optimal designs have low structural mass, to reduce the costs after a replacement. For GG-AWES, high aerodynamic performances are not required, from an economic point of view. Thus, these two information suggest that soft kites could be optimal design for GG-AWES. Further investigations are necessary.

The LCOE of GG-AWES and FG-AWES are similar and low, outlining that both the generation types, with a mature technology, could be disruptive in the energy market. The strength of these technologies is the high capacity factor. For a given rated power, the kite structure is, on average, a small portion of the initial capital cost. Thus, large kites can be designed, without a big impact on the total costs. This is the key to reach high capacity factors. High capacity factors imply power generation with low wind conditions. The hours with low wind speeds have typically a high electricity price. Therefore, power fed into the grid in these hours is really profitable.

For GG-AWES, the tether should be designed to have a working life, according to the tether cost. For FG-AWES, it is convenient to have tether designed to infinite life. The tether is found to have a big share in the total cost. A study on how to reduce this cost can have a big impact on LCOE. Cheaper tethers will be likely replaced more often. Thus, it could be interesting to study in details the creep phenomenon in the tether.

Aspect ratios similar to the ones of commercial aircraft are found to be optimal. However, for the AEP maximisation, higher AR are found. Researches could focus on the optimisation of high aspect ratio kites, in order to make them attractive also from an economic perspective. For both the generation types, extremely high maximum lift coefficients are found to be not attractive.

From these analyses, building a tower is never convenient. No take-off strategy is found to be cost effective. The cost model related to the take-off and landing structure is considered too simplistic to give any interesting information.

Chapter 8

Future works

Within this work, many open questions and future works are outlined. In the following list, the main are given:

- To improve the structural model a buckling constraint could be considered. This constraint would likely prevent the optimiser from finding really light optimal solutions.
- It could be interesting to estimate the tether life in the physic model. A constraint on the minimum number of operational years can be considered. In this way, the tether life can be included in the AEP maximisation case. The Lagrange multiplier on this constraint would give information on the constraint strength.
- A more accurate cost model for all the sub-systems is needed.
- It could be interesting to evaluate the accuracy of the reel-in model used in this thesis. The high uncertainty, given to this model, is showing that it is not impacting the results. However, the physics is modelled in a really approximate way.
- It could be interesting to create a FE model of the wings, idealising it with booms and skin panels [72]. This simple FE could be used in an optimisation algorithm to perform a more accurate structural design.
- It could be interesting to couple the FE model, just proposed, with a geometric parametrisation of the airfoil in an optimisation algorithm. In this way, the optimiser should be able to design the wing, considering the aerodynamics and structure at the same time.
- The model could be improved by including soft kites. An optimisation algorithm that can handle discontinuities could be used to find the optimal designs for multiple scenarios.
- The environmental impact of a AWES could be evaluated by considering the emissions needed to produce it. Thus, an environmental comparison with traditional wind turbines and other technologies could be performed. A multi-objective optimisation could show how the design would look like if the cost of energy and the environmental impact are minimised.
- It could be interesting to use a multi-objective approach to minimise the cost and, at the same time, the power per unit area of an AWES wind farm.

Chapter 9

Conclusions

In this thesis, the design of the main sub-systems of crosswind AWES are studied.

In Chapter 3, the derivation of the power equation for a generic crosswind AWES is shown. This power equation takes into account the flying mass and the relative power losses. It can be used by system designers to give a quantitative estimation of the power losses due to mass for both FG-AWES and GG-AWES. Moreover, the proposed formulation does not include the assumption of high glide ratio: it can model all kite types. In this chapter, a structural and a take-off model are presented. They are used to estimate the flying mass.

In Chapter 5, the methods, presented in Chapter 4, are used for the evaluation of the physical model. These methods allow a detailed understanding of the design trends. The key parameters for the maximisation of AEP are the wing area, the maximum lift coefficient and the drag coefficient at zero lift. They determine the capacity factor, thus they should be carefully designed. A method to design strong configurations is proposed. A really high maximum lift coefficient is found to be not so interesting for the AEP maximisation: the Lagrange multiplier on the maximum lift coefficient is low in this case. Finally, it is shown that large area kites could be placed in low wind regions, to obtain high capacity factors.

In Chapter 7, the same methods are applied to study the configuration designs that maximise the profit. A cost model is proposed in Chapter 6. From the design analyses, it turns out that GG-AWES and FG-AWES, with a mature technology, will be extremely competitive in the energy market, without any incentives. Since the kite structure does not represent a big share in the total costs, large area kites can ensure high capacity factors. This is the key to reach low cost of energy. From this analysis, FG-AWES can give higher profit if the kite is rarely replaced. Interestingly, building a tower is found to be not convenient: the optimiser chooses really small tower height.

Bibliography

[1] Wikipedia. George pocock (inventor). https://en.wikipedia.org/wiki/George_Pocock_(inventor), 2019 (accessed February 05, 2019).

[2] Miles L. Loyd. Crosswind Kite Power. *J. Energy*, 4(3):106–111, 1980.

[3] Antonello Cherubini. *Advances in Airborne Wind Energy and Wind Drones*. PhD thesis, Scuola Superiore Sant'Anna, 2017.

[4] Roland Schmehl. *Airborne Wind Energy*. Green Energy and Technology. Springer Singapore, 2018.

[5] Cristina Archer and Ken Caldeira. Global Assessment of High-Altitude Wind Power. *Energies*, 2(2):307–319, may 2009.

[6] Cristina L. Archer. An Introduction to Meteorology for Airborne Wind Energy. In Moritz Diehl Uwe Ahrens and Roland Schmehl, editors, *Airborne Wind Energy*, pages 81–94. 2013.

[7] Philip Bechtle, Mark Schelbergen, Roland Schmehl, Udo Zillmann, and Simon Watson. Airborne wind energy resource analysis. *Renew. Energy*, 141:1103–1116, 2019.

[8] Antonello Cherubini, Andrea Papini, Rocco Vertechy, and Marco Fontana. Airborne Wind Energy Systems: A review of the technologies. *Renew. Sustain. Energy Rev.*, 51:1461–1476, 2015.

[9] Uwe Ahrens. A breakthrough that could power the world. https://www.slideshare.net/UweAhrens/xwind-presentation, 2019 (accessed May 11, 2019).

[10] D. M. Legaignoux B. T. Legaignoux. Propulsive wing with inflatable armature PCT Patent Application WO8602902, 1987.

[11] Xaver Paulig, Merlin Bungart, and Bernd Specht. Conceptual Design of Textile Kites Considering Overall System Performance. In Moritz Diehl Uwe Ahrens and Roland Schmehl, editors, *Airborne Wind Energy*, pages 547–562. 2013.

[12] Storm Dunker. Ram-air Wing Design Considerations for Airborne Wind Energy. In Moritz Diehl Uwe Ahrens and Roland Schmehl, editors, *Airborne Wind Energy*, pages 517–546. 2013.

[13] Ampyx Power. https://www.ampyxpower.com/, 2019 (accessed April 19, 2019).

[14] Makani Power. https://makanipower.com/, 2019 (accessed April 19, 2019).

[15] Kitekraft. http://kitekraft.de/, 2019 (accessed April 19, 2019).

[16] Kitex. https://kitex.tech/, 2019 (accessed April 19, 2019).

[17] Eelke Bontekoe. Up! How to Launch and Retrieve a Tethered Aircraft, MSc thesis, Delft University of Technology. 2010.

[18] Lorenzo Fagiano and Stephan Schnez. On the take-off of airborne wind energy systems based on rigid wings. *Renew. Energy*, 107:473–488, 2017.

[19] Enerkite. `https://www.enerkite.de/en/`, 2019 (accessed April 19, 2019).

[20] Twintec. `http://twingtec.ch/`, 2019 (accessed April 19, 2019).

[21] Kitemill. `http://www.kitemill.com/`, 2019 (accessed April 19, 2019).

[22] I. Argatov, P. Rautakorpi, and R. Silvennoinen. Estimation of the mechanical energy output of the kite wind generator. *Renew. Energy*, 34(6):1525–1532, 2009.

[23] Rolf van der Vlugt, Anna Bley, Michael Noom, and Roland Schmehl. Quasi-steady model of a pumping kite power system. *Renew. Energy*, 131:83–99, 2019.

[24] Moritz Diehl. Airborne Wind Energy: Basic Concepts and Physical Foundations. In Moritz Diehl Uwe Ahrens and Roland Schmehl, editors, *Airborne Wind Energy*, pages 3–22. 2013.

[25] Cantwell. Finite Wing Theory, Stanford University. pages 1–62.

[26] M. Nita and D. Scholz. Estimating the Oswald Factor from Basic Aircraft Geometrical Parameters. *Dtsch. Luft- und Raumfahrtkongress*, 281424:1–19, 2012.

[27] Peter Taylo Sena Kumarasena, Nicholas P. Jones, Peter Irwin. Wind-Induced Vibration of Stay Cables. Technical report, HNTB Corporation 75 State St., Boston.

[28] Adrian Gambier. Retraction Phase Analysis of a Pumping Kite Wind Generator. In Roland Schmehl, editor, *Airborne Wind Energy*, pages 117–135. 2018.

[29] Rolf H. Luchsinger. Pumping Cycle Kite Power. In Moritz Diehl Uwe Ahrens and Roland Schmehl, editors, *Airborne Wind Energy*, pages 47–64. 2013.

[30] Mark Schelbergen and Roland Schmehl. Optimal Operation and Power Curve Estimation of a Pumping Airborne Wind Energy System. In *14th EAWE PhD Semin. Wind Energy*, Vrije Universiteit Brussel, Belgium, 2018.

[31] Odeh Dababneh and Altan Kayran. Design, analysis and optimization of thin walled semi-monocoque wing structures using different structural idealization in the preliminary design phase. *Int. J. Struct. Integr.*, 5(3):214–226, 2014.

[32] Quentin R. Wald. The aerodynamics of propellers. *Prog. Aerosp. Sci.*, 42(2):85–128, 2006.

[33] Martin Hansen. *Aerodynamics of Wind Turbines*. Routledge, 2015.

[34] Martin O.L.Hansen. Lecture notes in: *Wind Turbine Technology and Aerodynamics*, December 2017.

[35] Jorge Nocedal and Stephan Wright. *Numerical optimization, series in operations research and financial engineering*. 2006.

[36] fmincon. `https://se.mathworks.com/help/optim/ug/fmincon.html`, 2019 (accessed July 7, 2019).

[37] Bruno Sudret, Stefano Marelli, and Joe Wiart. Surrogate models for uncertainty quantification: An overview. *2017 11th Eur. Conf. Antennas Propagation, EUCAP 2017*, pages 793–797, 2017.

[38] B. Marelli, S. and Lamas, C. and Konakli, K. and Mylonas, C. and Wiederkehr, P. and Sudret. UqLab User Manual – Sensitivity Analysis. Technical report, Chair of Risk, Safety \& Uncertainty Quantification, ETH Zurich, 2019.

[39] Samik Raychaudhuri. Introduction to Monte Carlo Simulation. In *2008 Winter Simul. Conf.*, pages 91–100, 2008.

[40] Ilya M. Sobol. Sensitivity analysis for nonlinear mathematical models. *Math. Model. Comput. Exp.*, 1(4):407–414, 1993.

[41] Damon Vander Lind. Analysis and Flight Test Validation of High Performance AirborneWind Turbines. In Moritz Diehl Uwe Ahrens and Roland Schmehl, editors, *Airborne Wind Energy*, pages 473–490. 2013.

[42] Uwe Ahrens, Moritz Diehl, and Roland Schmehl, editors. *Airborne Wind Energy, Springer Verlag, Berlin Heidelberg*. 2013.

[43] Makani Power. Response to the Federal Aviation Authority. *Docket No. FAA-2011-1279; Not. No. 11-07 Notif. Airborne Wind Energy Syst.*, (11):1–10, 2012.

[44] Antonello Cherubini. Fundamentals of Airborne Wind Energy Systems, Universidad Carlos III de Madrid, 2017.

[45] Giovanni Licitra, J. Koenemann, A. Bürger, P. Williams, R. Ruiterkamp, and M. Diehl. Performance assessment of a rigid wing Airborne Wind Energy pumping system. *Energy*, 173(February):569–585, 2019.

[46] Giovanni Licitra, S. Sieberling, S. Engelen, P. Williams, R. Ruiterkamp, and M. Diehl. Optimal control for minimizing power consumption during holding patterns for airborne wind energy pumping system. *2016 Eur. Control Conf. ECC 2016*, pages 1574–1579, 2016.

[47] Richard Ruiterkamp and Sören Sieberling. Description and Preliminary Test Results of a Six Degrees of Freedom Rigid Wing Pumping System. In Moritz Diehl Uwe Ahrens and Roland Schmehl, editors, *Airborne Wind Energy*, pages 443–458. 2013.

[48] Uwe Fechner and Roland Schmehl. Model-Based Efficiency Analysis of Wind Power Conversion by a Pumping Kite Power System. In Moritz Diehl Uwe Ahrens and Roland Schmehl, editors, *Airborne Wind Energy*, pages 249–269. 2013.

[49] I. Argatov and R. Silvennoinen. Energy conversion efficiency of the pumping kite wind generator. *Renew. Energy*, 35(5):1052–1060, may 2010.

[50] Florian Bauer, Ralph M. Kennel, Christoph M. Hackl, Filippo Campagnolo, Michael Patt, and Roland Schmehl. Drag power kite with very high lift coefficient. *Renew. Energy*, 118:290–305, 2018.

[51] Magnax. `https://www.magnax.com/technology`, 2019 (accessed April 19, 2019).

[52] Rigo Bosman, Valerie Reid, Martin Vlasblom, and Paul Smeets. Airborne Wind Energy Tethers with High-Modulus Polyethylene Fibers. In Moritz Diehl Uwe Ahrens and Roland Schmehl, editors, *Airborne Wind Energy*, pages 563–585. 2013.

[53] Glider review. http://www.gliderreview.com/, 2019 (accessed May 11, 2019).

[54] Jannis Heilmann. The technical and economic potential of airborne wind energy, MSc Thesis, Utrecht University, 2012.

[55] Jannis Heilmann and Corey Houle. Economics of Pumping Kite Generators. In Moritz Diehl Uwe Ahrens and Roland Schmehl, editors, *Green Energy Technol.*, pages 271–284. 2013.

[56] Christoph Grete. Optimization, Scaling and Economics of Pumping Kite Power Systems, MSc thesis, Delft University of Technology. 2014.

[57] M. De Lellis, A. K. Mendonça, R. Saraiva, A. Trofino, and Lezana. Electric power generation in wind farms with pumping kites: An economical analysis. *Renew. Energy*, 86:163–172, 2016.

[58] Ivan Argatov and Valentin Shafranov. Economic assessment of small-scale kite wind generators. *Renew. Energy*, 89:125–134, apr 2016.

[59] Alibaba.com. https://www.alibaba.com/, 2019 (accessed May 14, 2019).

[60] E. Santecchia, A. M. S. Hamouda, F. Musharavati, E. Zalnezhad, M. Cabibbo, M. El Mehtedi and S. Spigarelli. A Review on Fatigue Life Prediction Methods for Metals. *Adv. Mater. Sci. Eng.*, 2016, 2016.

[61] Electric vehicle battery: Materials, cost, lifespan. https://www.ucsusa.org/clean-vehicles/electric-vehicles/electric-cars-battery-life-materials-cost, 2019 (accessed May 14, 2019).

[62] Florian Bauer, Christoph M. Hackl, Keyue Smedley, and Ralph M. Kennel. Crosswind kite power with tower. In Roland Schmehl, editor, *Airborne Wind Energy*, pages 441–462. 2018.

[63] Steel prices. https://worldsteelprices.com/, 2019 (accessed May 10, 2019).

[64] Pietro Faggiani. Pumping Kites Wind Farm, MSc thesis, Delft University of Technology, 2014.

[65] Price of a transformer, year = 2019 (accessed May 14, 2019), howpublished = "https://electrical-engineering-portal.com/price-of-a-transformer".

[66] Pietro Faggiani and Roland Schmehl. Design and Economics of a Pumping Kite Wind Park. In Roland Schmehl, editor, *Airborne Wind Energy*, pages 391–411. 2018.

[67] Operation and maintenance costs of wind generated power. https://www.wind-energy-the-facts.org/operation-and-maintenance-costs-of-wind-generated-power.html, 2019 (accessed July 7, 2019).

[68] Christoph Drexler, Alexander Hofmann, and Balint Kiss. Airborne Wind Energy Technology Review and Feasibility in Germany. (July), 2017.

[69] Grant Thornton. Renewable energy discount rate survey results – 2017. 2018.

[70] Kristian Rune Poulsen Karsten Capion, Morten Stryg. Electricity Price Outlook 2018, 2018.

[71] Civil jet aircraft design. https://booksite.elsevier.com/9780340741528/appendices/data-a/table-3/table.htm, 2019 (accessed July 7, 2019).

[72] T. H G Megson. *Aircraft Structures for Engineering Students*. Elsevier, 2013.

Appendices

Appendix A

Sobol' indices for the maximisation of AEP

A.1 Analysis with $A_{kite} = 30$ m^2

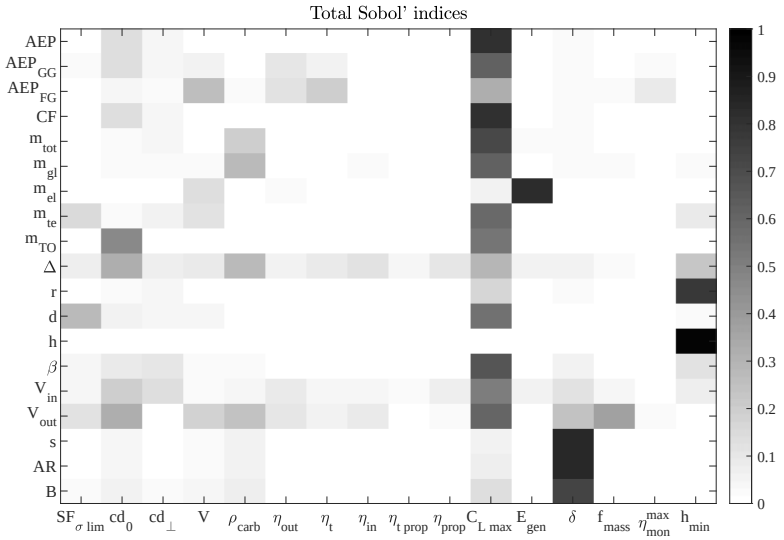

Figure A.1: Graphical visualization of the total Sobol' indices for a fixed wing area (first part).

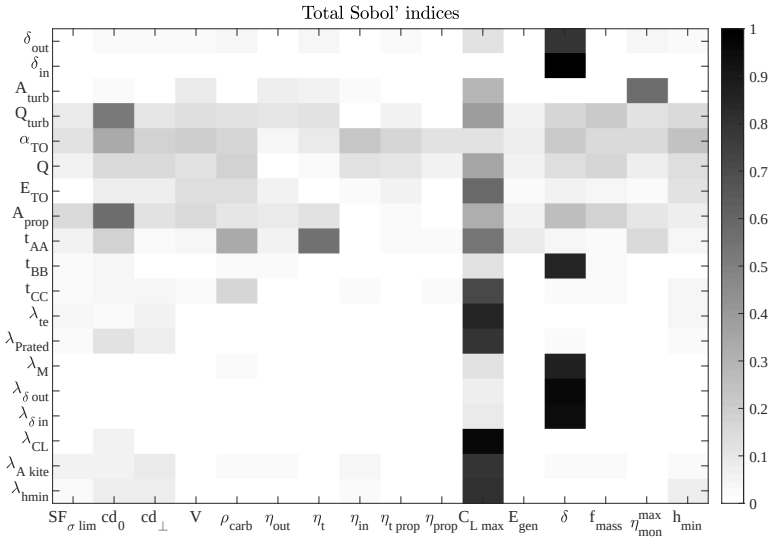

Figure A.2: Graphical visualization of the total Sobol' indices for a fixed wing area (second part).

A.2 Analysis considering wind resources uncertainties

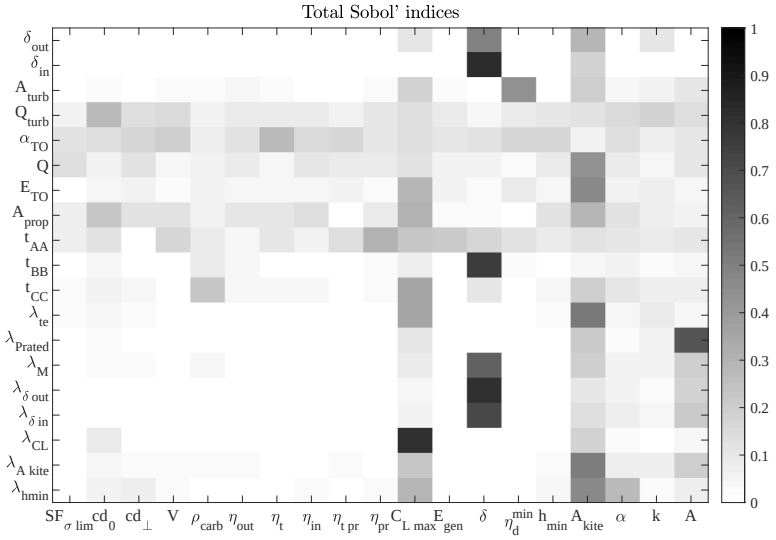

Figure A.3: Graphical visualization of the total Sobol' indices considering the wind resource uncertainties (second part).

Appendix B

Sobol' indices for the profit maximisation

B.1 Analysis with fixed wind resources

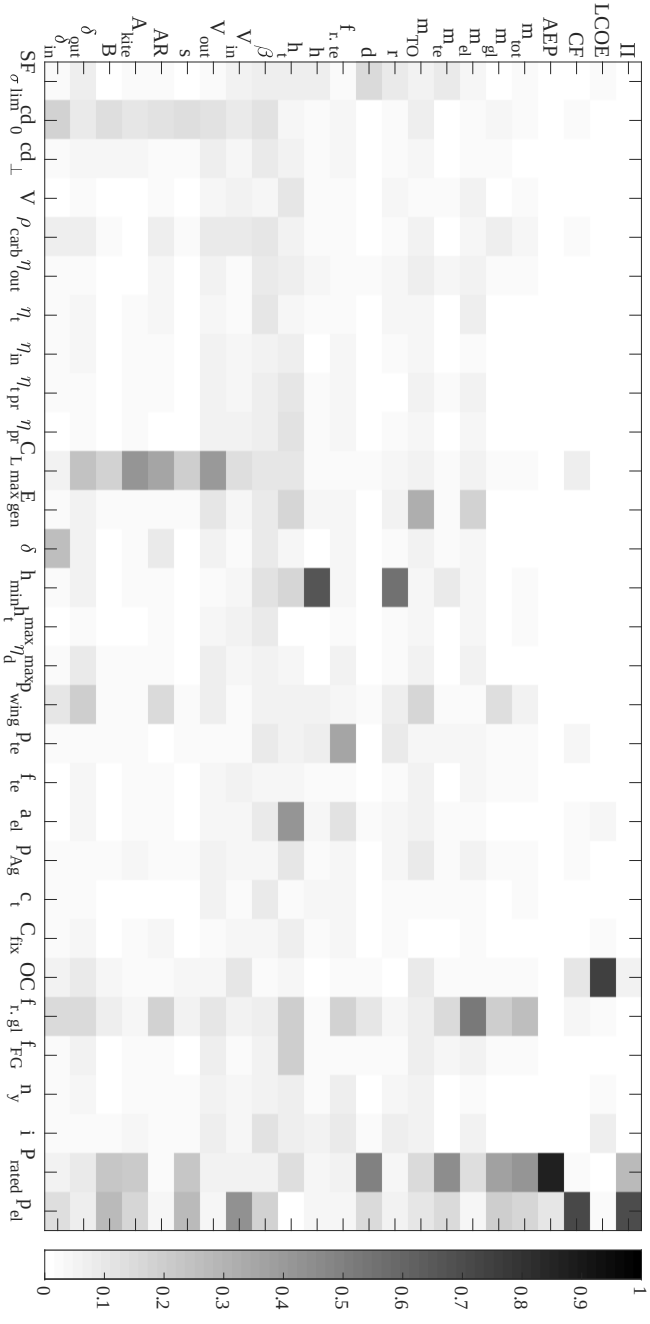

Figure B.1: Graphical visualization of the total Sobol' indices for the profit maximisation case (first part).

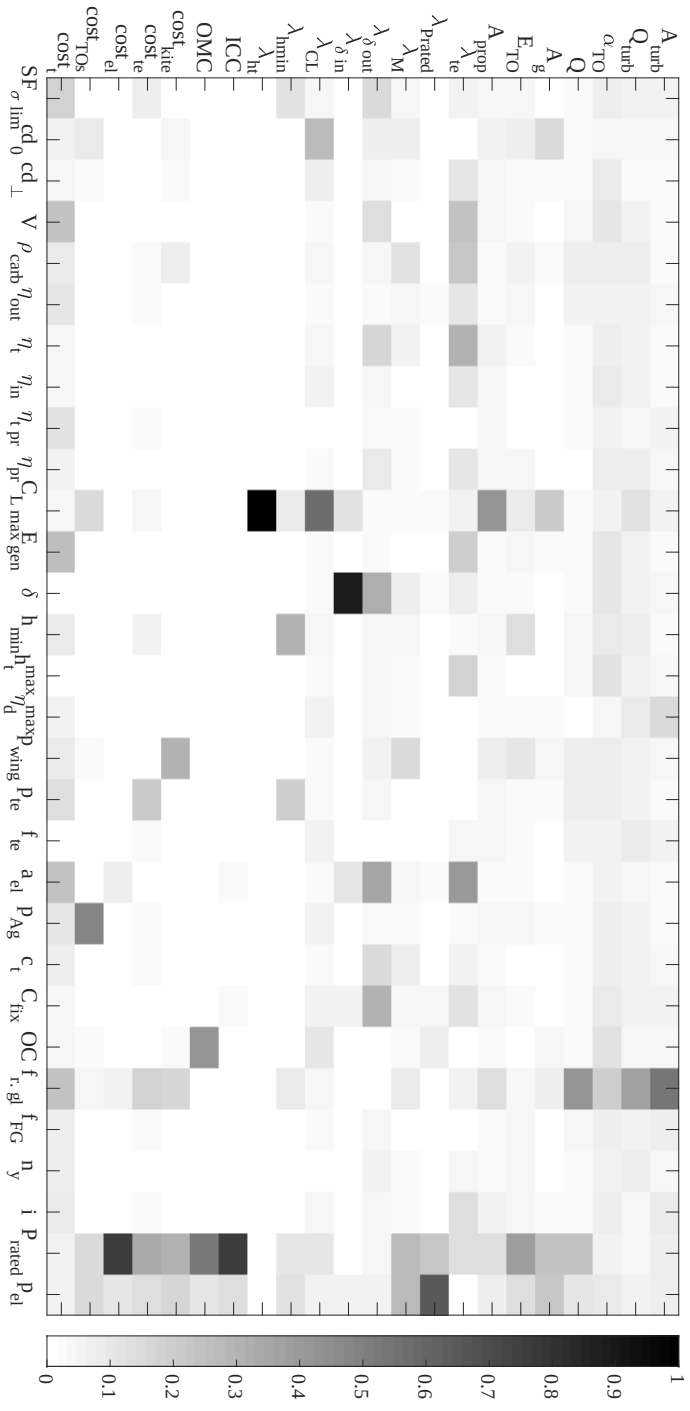

Figure B.2: Graphical visualization of the total Sobol' indices for the profit maximisation case (second part).

B.2 Analysis considering wind resources uncertainties

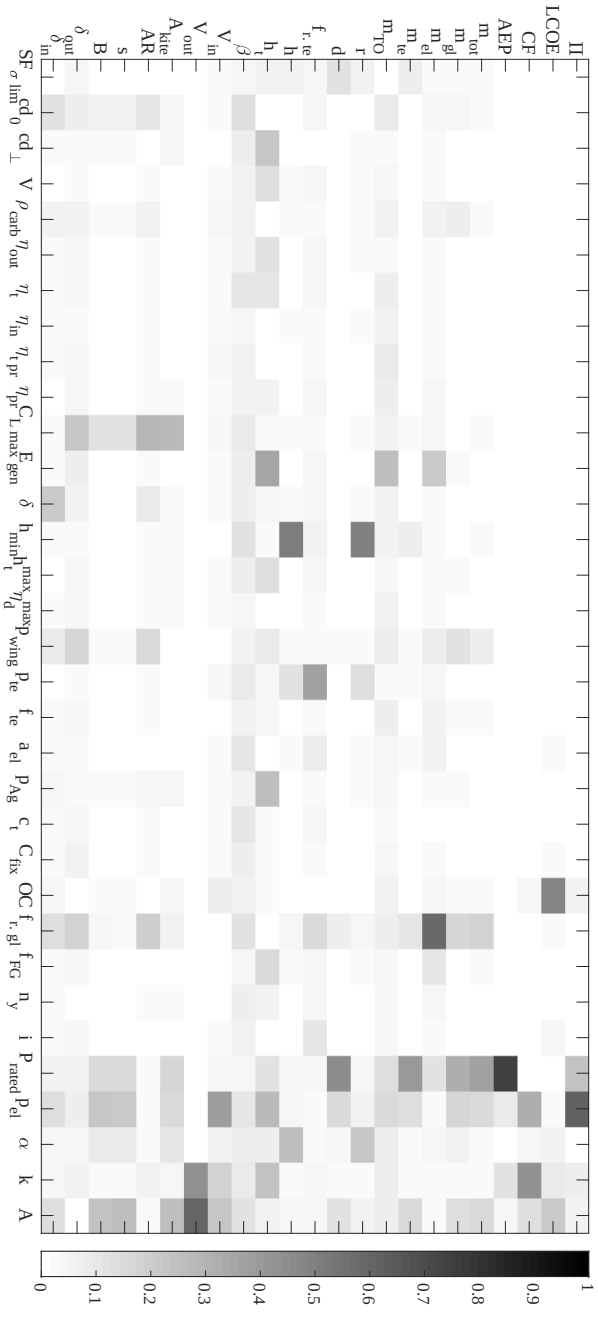

Figure B.3: Graphical visualization of the total Sobol' indices considering wind resources uncertainties (first part).

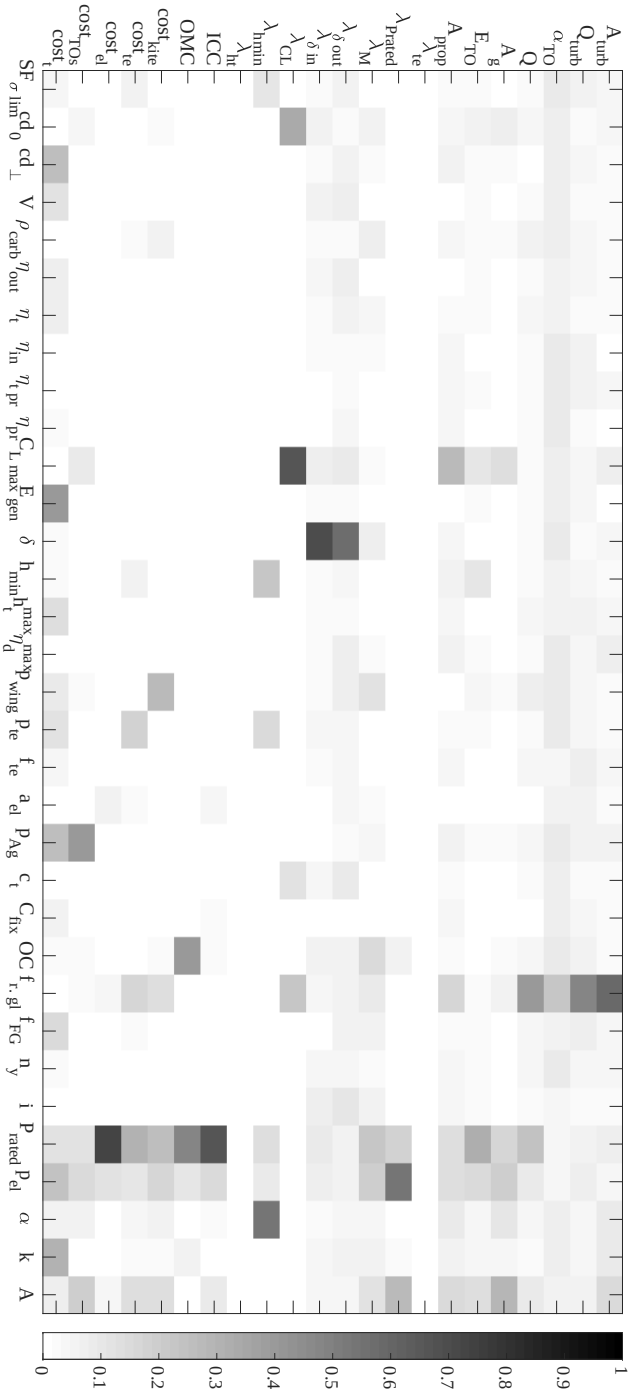

Figure B.4: Graphical visualization of the total Sobol' indices considering wind resources uncertainties (second part).

B.3 Analysis for a GG-AWES

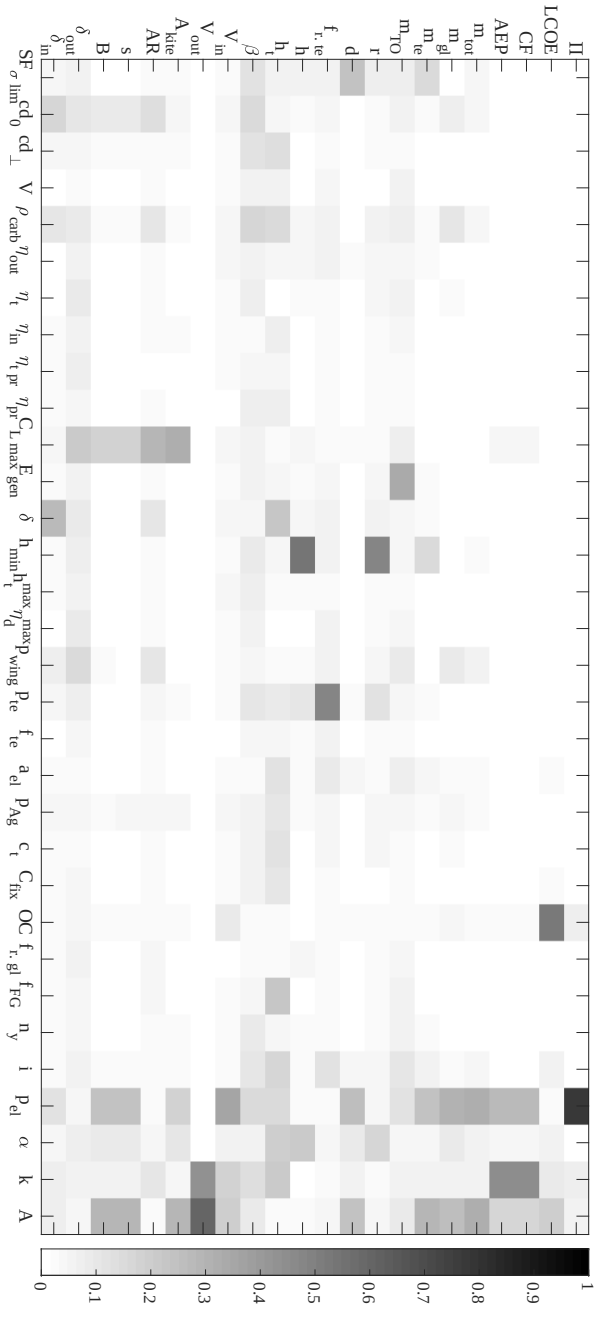

Figure B.5: Graphical visualization of the total Sobol' indices for the GG-AWES case (first part).

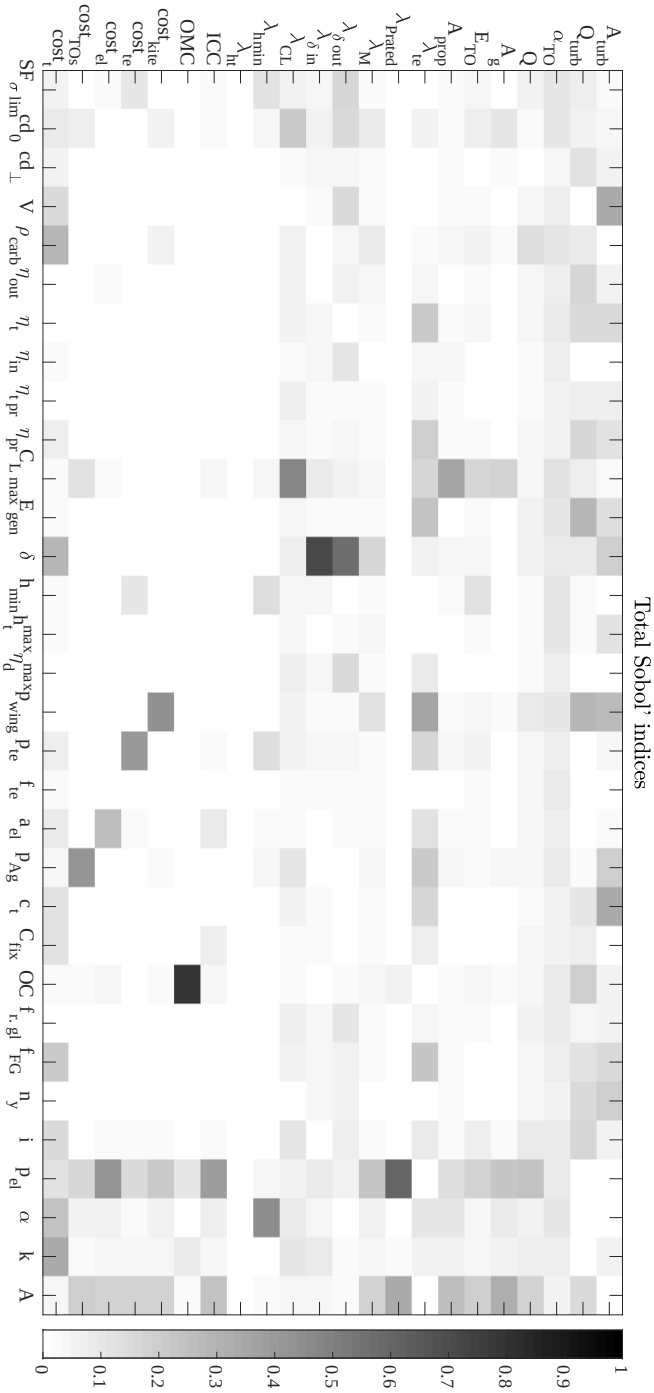

Figure B.6: Graphical visualization of the total Sobol' indices for the GG-AWES case (second part).

B.4 Analysis for a FG-AWES

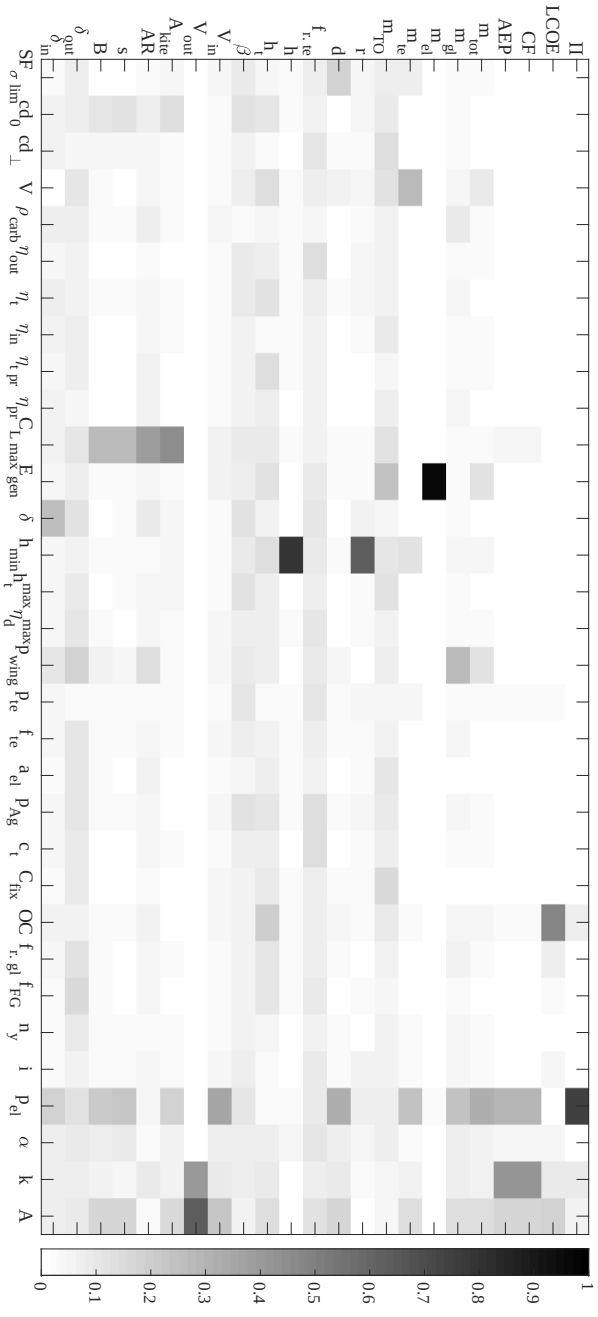

Figure B.7: Graphical visualization of the total Sobol' indices for the FG-AWES case (first part).

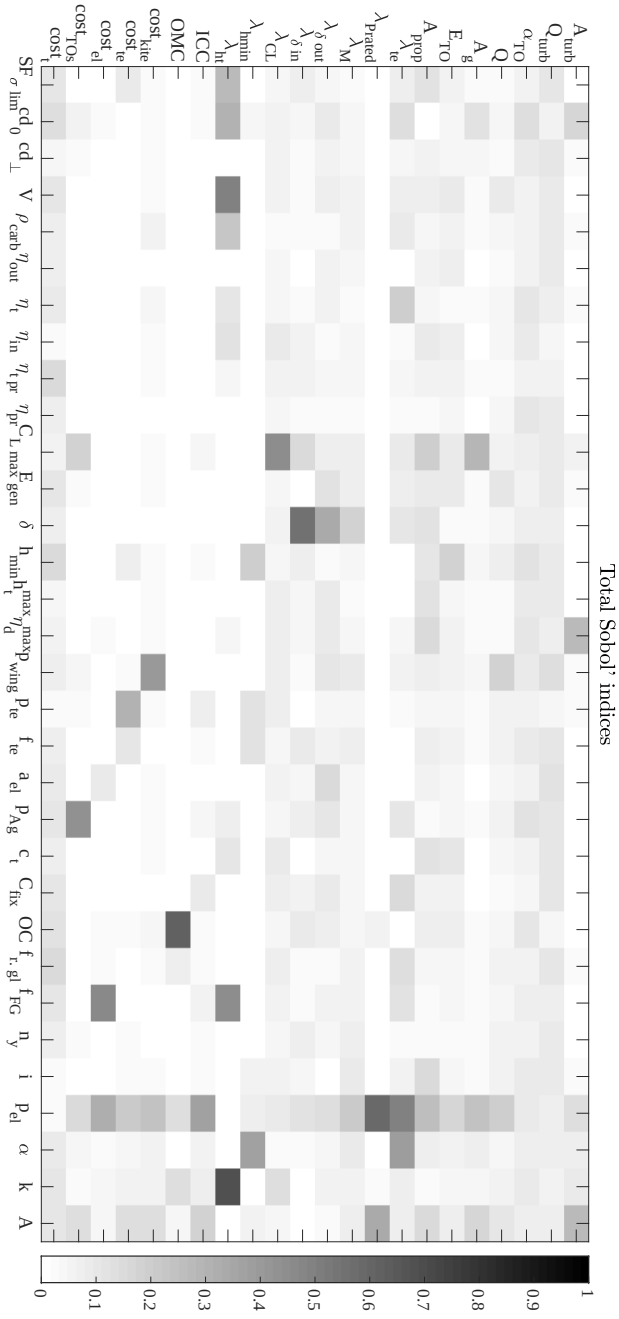

Figure B.8: Graphical visualization of the total Sobol' indices for the FG-AWES case (second part).